

NEAR-FIELD MIMO CHANNEL MODELING WITH APPLICATIONS TO SMALL
ANECHOIC CHAMBERS

By

JONATHAN TEFFT

Bachelor of Science in Electrical Engineering, The University of New Hampshire, 2009

Master of Science in Electrical Engineering, The University of New Hampshire, 2011

DISSERTATION

Submitted to The University of New Hampshire
in Partial Fulfilment of
the Requirements for the Degree of

Doctor of Philosophy

in

Electrical Engineering

December 2018

This dissertation has been examined and approved in partial fulfillment of the requirements for the degree of Doctor of Philosophy in Electrical Engineering by:

Dissertation Director, Dr. Nicholas J. Kirsch, Associate Professor of
Electrical and Computer Engineering

Dr. Kent A. Chamberlin, Professor of
Electrical and Computer Engineering

Dr. Michael J. Carter, Associate Professor of
Electrical and Computer Engineering

Dr. Qiaoyan Yu, Associate Professor of
Electrical and Computer Engineering

Dr. Joachim Raeder, Professor of
Physics

On November 14, 2018

Approval signatures are on file with the University of New Hampshire Graduate School

Acknowledgements

I would like to acknowledge Dr. Nicholas Kirsch for advising me on this dissertation work, and for funding me with a Graduate Research Assistantship for multiple years. This allowed me to continue and complete my work despite numerous changes in direction in my research.

I would like to acknowledge Octoscope, Inc. and Fanny Mlinarsky for funding much of this research, and providing a small anechoic chamber for measurements associated with much of the work in this dissertation. Without this, the work of this dissertation could not have been produced.

I would also like to acknowledge my committee members Dr. Kent Chamberlin, Dr. Michael Carter, Dr. Qiaoyan Yu, and Dr. Joachim Raeder, for agreeing to be on my committee and for taking the time to review my dissertation. I especially would like to thank Dr. Chamberlin and Dr. Carter for providing advice on several electromagnetic and mathematical topics included in this dissertation.

I would also like to thank my fellow graduate students in the UNH Wireless Systems Lab for their moral support over the past several years. Finally, I would like to acknowledge my parents John and Susan Tefft, my partner Avery Parkes, and my friends for their infinite patience and support. I could not have made it through this arduous process without you.

Jonathan Tefft

Contents

List of Tables	vii
List of Figures	viii
Abstract	xiii
1. Introduction	1
1.1 Motivation	1
1.1.1 Importance of Small Chamber MIMO Test Solutions	3
1.1.2 Importance of Near-Field MIMO Channel Models	5
1.2 Contributions, and Outline	6
2. Background	10
2.1 Fundamental Concepts	10
2.1.1 SISO channels	10
2.1.2 MIMO	12
2.1.3 Near-Field Topics and Mutual Coupling	21
2.2 Literature Review	22
2.2.1 MIMO-OTA Testing	23
2.2.2 Near-Field MIMO Channels and Capacity	28

2.3	Preliminary Investigations	34
2.3.1	Hertzian Dipole Field-Based Channel Matrix Formulation	34
2.3.2	AWGN Channel	40
2.3.3	Normalization	40
2.3.4	Capacity Equations	41
2.3.5	Channel and Capacity Simulation	43
2.3.6	Background for Selection of Free-Space Green's Function as Basis	45
3.	Small Anechoic Chamber Feasibility for MIMO-OTA Testing	57
3.1	Electromagnetic Field Synthesis	58
3.1.1	Number of probe antennas	58
3.1.2	3GPP SCME Channel Model	59
3.2	Small chamber system	61
3.2.1	Numerical Model	62
3.2.2	Computational Electromagnetic Model	65
3.3	Analytical Results	66
3.4	Electromagnetic Simulation Results	69
3.5	Conclusions	72
4.	Near-Field Channel Model Framework	74
4.1	Formulation of Channel using Dipole Arrays	76
4.1.1	Mathematical Channel Model with Arbitrary Dipole Orientations	78
4.1.2	Numerical Computation of Dipole Array Channel	86
4.1.3	Numerical Computation Setup and Results	88
4.2	Dipole Array Channel with Spatial Attribute Function Decomposition	92

4.2.1	Plane Waves as Spatial Attribute Functions	94
4.2.2	Point Sources as Spatial Attribute Functions	98
4.2.3	Point Source Location	99
4.2.4	Inner Product of Point Sources	101
4.2.5	Use of Point Source and Plane Waves as Joint Spatial Attribute Functions	104
4.3	Fitting of Spatial Attribute Functions to Numerical Channel	104
4.3.1	Point Source Fitting	105
4.3.2	Refinement Using Plane Waves	106
4.4	Validation of Spatial Attribute Function Selection with Numerical Channel .	107
4.5	Conclusions	111
5.	Statistical and Frequency Extensions of Near-Field Channel Model . . .	112
5.1	Accurate Method of Fitting Spatial Attribute Functions to Measured Data .	114
5.1.1	Generalized Least Squares	115
5.1.2	Covariograms and Spatial Dependence	116
5.1.3	Complex Geostatistical Covariance Model	118
5.1.4	Geostatistical Regression	122
5.1.5	Geostatistical Kriging	125
5.2	Adapting Spatial Attribute Function Set for a Wideband Model	128
5.2.1	Algorithm for Fitting Spatial Attribute Function Set	130
5.2.2	Modeling Coefficients as Polynomial Functions of Frequency	131
5.2.3	Final Wideband Model Description	132
5.3	System Description	133
5.3.1	Chamber Configuration and Properties	133

5.3.2	Antenna Properties	135
5.3.3	Measurement Equipment	137
5.4	Measurement Campaign Description	138
5.4.1	Antenna Orientations and Positions	140
5.4.2	Chosen Measurement Campaign Positions	142
5.4.3	Resulting Dataset	144
5.5	Modeling of Measurement Data	147
5.5.1	Analysis of Complex Geostatistical Covariance Of Measurements . . .	150
5.5.2	Selected Wideband Frequency Bands for Modeling	161
5.5.3	Performance Analysis of Frequency-Scaled Spatial Attribute Functions	162
5.5.4	Spatial Attribute Function Set Extension to Wideband Model	164
5.5.5	Wideband Model Accuracy	168
5.6	Conclusions	171
6.	Application of Small Chamber Model to MIMO Analysis	173
6.1	Small Anechoic Chamber Channel and Impulse Response	173
6.2	Small Anechoic Chamber Spatial Correlation Analysis	178
6.3	Wideband MIMO Capacity Using Small Chamber Channel Model	185
6.3.1	MIMO Capacity Analysis System Description	185
6.3.2	MIMO Capacity and Eigenvalue Results	186
6.4	Conclusions	194
7.	Conclusion and Future Work	196
	References	198

List of Tables

3.1	Simulation Parameters	64
3.2	Simulation Results	70

List of Figures

1.1	3GPP Release Timeline for 5G [1]	2
1.2	Contribution Flowchart for Chapters 4 and 5	7
2.1	2 Element Dipole and Loop Antenna Array [2]	31
2.2	Near-Field 2×2 MIMO Example [2]	31
2.3	Equivalent Circuit for Near-Field MIMO System [2]	32
2.4	Near-Field MIMO Array Reflector [3]	33
2.5	FDTD Near-Field MIMO Array Simulation [3]	33
2.6	2×2 MIMO System Model	38
2.7	Capacity with Uniform Allocation vs. SNR and Spacing	45
2.8	Dipole Electric Field Formulation	48
2.9	Dipole Mutual Impedance Formulation	53
2.10	Dipole Self Impedance Formulation	55
3.1	Small Anechoic Chamber Dimensions	63
3.2	HFSS Chamber Model of a Small Chamber	66
3.3	CDF of Reflectivity for Select Configurations, 700 MHz and 35 degree spread	68
4.1	Chapter 4 Contribution Flowchart	75

4.2	Dipole Mutual Impedance Formulation	78
4.3	Dipole Self Impedance Formulation	81
4.4	Antenna Array and Dipole Port Definitions	82
4.5	Transmission Line Network Definition	83
4.6	Definition of Parallel Admittance Networks	84
4.7	Modeled System for Numerical Computation	89
4.8	Magnitude of Channel Vs. Dipole Position	91
4.9	Phase of Channel Vs. Dipole Position	91
4.10	Visualization of Point Source Wave Fronts	100
4.11	Normalized Histogram of Cross-Correlation Vs. Separation	103
4.12	LogNormal Mean EVM For Combinations of Spatial Attribute Functions . .	108
4.13	Standard Deviation of EVM For Combinations of Spatial Attribute Functions	110
4.14	LogNormal Mean + 1 SD EVM For Combinations of Spatial Attribute Functions	110
5.1	Chapter 5 Contribution Flowchart	113
5.2	Octoscope octoBox BOX-38 Interior	134
5.3	Octoscope OBS-14 Log Periodic Antenna [4]	135
5.4	Octoscope OBS-14 Array [4]	136
5.5	Octoscope OBS-14 Radiation Patterns [4]	136
5.6	Pasternack PE51083 Rubber Duck Antenna [5]	137
5.7	Keysight E5063A VNA [6]	138
5.8	Chamber and Measurement System Diagram	141
5.9	Measured Channel Magnitude (dB), Probe One (Located in Lower Right), 5.15 GHz	145

5.10 Measured Channel Phase (rad.), Probe One (Located in Lower Right), 5.15 GHz	146
5.11 LN Mean + σ EVM, Probe One, 5.725 GHz	148
5.12 LN Mean + σ EVM, Probe Two, 5.725 GHz	148
5.13 LN Mean + σ EVM, Probe Three, 5.725 GHz	149
5.14 LN Mean + σ EVM, Probe Four, 5.725 GHz	149
5.15 Measured Channel Spatial X-Cov., Mag., Probe One, 5.15 GHz	152
5.16 Measured Channel Spatial X-Cov., Real, Probe One, 5.15 GHz	152
5.17 Measured Channel Spatial X-Cov., Imag., Probe One, 5.15 GHz	153
5.18 Measured Channel Spatial Power Spectrum, Probe One, 5.15 GHz	153
5.19 Residual Emp. Spatial X-Cov., Mag., Probe One, 5.15 GHz	154
5.20 Residual Emp. Spatial X-Cov., Real, Probe One, 5.15 GHz	155
5.21 Residual Emp. Spatial X-Cov., Imag., Probe One, 5.15 GHz	156
5.22 Residual Emp. Spatial Power Spectrum, Probe One, 5.15 GHz	157
5.23 Residual Model Spatial X-Cov., Mag., Probe One, 5.15 GHz	158
5.24 Residual Model Spatial X-Cov., Real, Probe One, 5.15 GHz	159
5.25 Residual Model Spatial X-Cov., Imag., Probe One, 5.15 GHz	160
5.26 Empirical LN Mean EVM vs. Freq., Probe One Band Four	163
5.27 Empirical LN Mean EVM vs. Freq., Probe Four Band Three	163
5.28 Emp. and Poly. Model of β_1 Mag. vs. Freq., Probe One Band Two	165
5.29 Emp. and Poly. Model of β_1 Phase vs. Freq., Probe One Band Two	166
5.30 Emp. and Poly. Model of β_4 Mag. vs. Freq., Probe Two Band One	166
5.31 Emp. and Poly. Model of β_4 PHase vs. Freq., Probe Two Band One	167
5.32 Emp. and Poly. Model of σ^2 vs. Freq., Probe Two Band Four	167

5.33	Emp. and Poly. Model of c_1 vs. Freq., Probe Three Band Two	168
5.34	Modeled LN Mean EVM vs. Freq., Probe One Band Four	169
5.35	Modeled LN Mean EVM vs. Freq., Probe Four Band Three	169
5.36	Increase of LN Mean EVM From Emp. to Model vs. Freq., Probe 1 Band 4 .	170
5.37	Increase of LN Mean EVM From Emp. to Model vs. Freq., Probe 4 Band 3 .	171
6.1	Probe One (Lower Right) Channel Model Mag. Over Test Zone	174
6.2	Probe One (Lower Right) Channel Model Phase Over Test Zone	175
6.3	Probe One Channel Impulse Response at Chamber Center	176
6.4	Probe Two Channel Impulse Response at Chamber Center	177
6.5	Probe Three Channel Impulse Response at Chamber Center	177
6.6	Probe Four Channel Impulse Response at Chamber Center	178
6.7	Probe One, Empirical and Polynomial Fit Spatial Correlation vs. Separation	180
6.8	Probe Two, Empirical and Polynomial Fit Spatial Correlation vs. Separation	180
6.9	Probe Three, Empirical and Polynomial Fit Spatial Correlation vs. Separation	181
6.10	Probe Four, Empirical and Polynomial Fit Spatial Correlation vs. Separation	181
6.11	Probe One, Empirical Spatial Correlation CCDFs vs. Separation	182
6.12	Probe Two, Empirical Spatial Correlation CCDFs vs. Separation	183
6.13	Probe Three, Empirical Spatial Correlation CCDFs vs. Separation	183
6.14	Probe Four, Empirical Spatial Correlation CCDFs vs. Separation	184
6.15	$0.25 \lambda \times 0.25 \lambda$ DUT WB Cap. Vs. DUT Center Pos.	186
6.16	$0.5 \lambda \times 0.5 \lambda$ DUT WB Cap. Vs. DUT Center Pos.	187
6.17	$\lambda \times \lambda$ DUT WB Cap. Vs. DUT Center Pos.	187
6.18	$1.5 \lambda \times 1.5 \lambda$ DUT WB Cap. Vs. DUT Center Pos.	188

6.19	$0.25 \lambda \times 0.25 \lambda$ DUT WB Cap. CCDF	189
6.20	$0.5 \lambda \times 0.5 \lambda$ DUT WB Cap. CCDF	189
6.21	$\lambda \times \lambda$ DUT WB Cap. CCDF	190
6.22	$1.5 \lambda \times 1.5 \lambda$ DUT WB Cap. CCDF	190
6.23	$\frac{\lambda}{4} \times \frac{\lambda}{4}$ DUT Channel Eigenvalue CCDF	192
6.24	$\frac{\lambda}{2} \times \frac{\lambda}{2}$ DUT Channel Eigenvalue CCDF	192
6.25	$\lambda \times \lambda$ DUT Channel Eigenvalue CCDF	193
6.26	$\frac{3\lambda}{2} \times \frac{3\lambda}{2}$ DUT Channel Eigenvalue CCDF	193

Abstract

NEAR-FIELD MIMO CHANNEL MODELING WITH APPLICATIONS TO SMALL
ANECHOIC CHAMBERS

By

Jonathan Tefft

University of New Hampshire

Demand for wireless communications is rapidly expanding, especially in areas of high-speed communications including 4K video over wireless HDMI replacements and millimeter wave communications. Multiple-input multiple-output (MIMO) systems leverage spatial diversity to achieve higher capacity, helping to meet this demand for high-speed communications. The cost of consumer wireless devices can be lowered by testing in small, affordable multi-antenna environments. However, there is a lack of knowledge of MIMO in the near field. Near-field (specifically Fresnel region and near the Fraunhofer distance) MIMO channels define the performance of these systems, therefore a robust method of near-field MIMO channel modeling is needed to aid in system design and testing. The contributions of this dissertation include a method of iteratively decomposing a sampled broadband Fresnel region and near-Fraunhofer distance SISO channel into a set of spatial functions. The channel residual of the spatial functions was statistically analyzed to refine the channel estimate model and include effects not modeled in selected spatial functions. A robust simulation and measurement campaign for model verification was performed in a small anechoic chamber, and in turn the SISO models were combined into a MIMO channel description used to evaluate the MIMO performance of a small anechoic chamber environment. In addition

to developing and evaluating a wideband MIMO channel model, a feasibility analysis was performed on the ability of small MIMO-OTA anechoic test chambers to reproduce specific MIMO test environments in a test zone.

CHAPTER 1

Introduction

1.1 Motivation

Recently, there has been an explosion in the demand for internet access through wireless communications networks, including smart phones, tablets, and laptops. Applications such as streaming video have exponentially increased the amount of data consumed by users as well as the data rate requirements of such use. Wireless communication is a critical broadband access strategy in this country and around the world, particularly in rural areas. The US national broadband plan [7] has stated long-term goals including that “at least 100 million US homes should have affordable access to actual download speeds of 100 Mbps and actual upload speeds of 50 Mbps...The United States should have the fastest and most extensive wireless networks of any nation...Every American should have affordable access to robust broadband service” [7]. By 2020, some estimate that the amount of spectrum necessary to support mobile broadband is 1,720 MHz.

In addition, improvements in spectral efficiency and increase in the density of network architectures will be necessary to help meet this demand. According to the 3rd Generation Partnership Project (3GPP), from 2010 to 2025, there is a desired 1,000-fold increase in capacity desired to meet demand, requiring, for example “three times more spectrum, six times more spectrum efficiency, and 56 times increased network density” [8]. The 3GPP is on track for that level of usage growth, and is addressing this need in its Release 15 and 16 standards, which define 5G [1]. Figure 1.1 illustrates this release schedule.

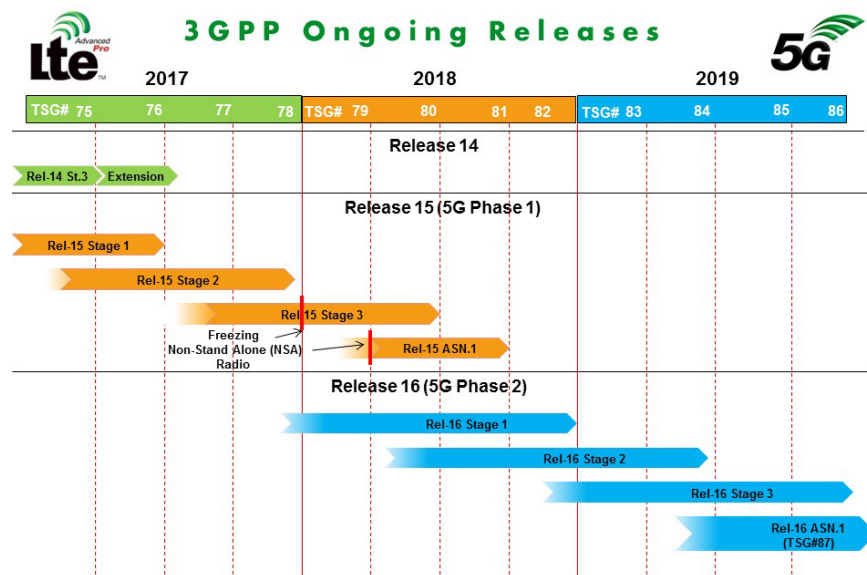


Figure 1.1: 3GPP Release Timeline for 5G [1]

Evolving standards and technologies will help to meet these objectives. These standards will utilize an increase in available spectrum whether as a primary user or opportunistic secondary user through software-defined radio. They will utilize state of the art techniques to optimize spectral efficiency through use of schemes such as multiple input multiple output (MIMO), massive MIMO, and multi-user (MU)-MIMO. Network densities will increase, with cells shrinking to reduce inter-cell interference, increase signal to interference plus noise ratio (SINR) for the communications link, and therefore increase capacity for each user.

Evolving standards that will take advantage of these techniques include 5G. According to a white paper by The Wireless Association (CTIA) [9], 5G will be able to utilize spectrum above 24 GHz, or millimeter wave spectrum. This will allow spectrum blocks in excess of 200 MHz, but will require extremely small cells due to the short range of propagation of millimeter wave signals, and in addition to their inability to penetrate objects including walls. CTIA states that the United States Federal Communications Commission (FCC) is

working to provide access to 10,000 MHz of new high-band spectrum for mobile broadband in its Spectrum Frontiers proceeding. 5G will be 10 times faster and support 100 times more devices.

5G will need to yield enhanced mobile broadband through capacity enhancement (giga-bytes per second for applications such as 4K 3D video), support a massive internet of things through massive connectivity (e.g. sensor networks), and support low latency and ultra-high reliability (self-driving cars) [8].

In addition to 5G, other high-data rate applications that utilize MIMO, potentially in the near-field, include millimeter wave WiFi 802.11ad (more specifically its extension 802.11ay), and high definition video interconnects supporting resolutions up to 4K (which could replace High-Definition Multimedia Interface (HDMI)).

With the majority of emerging high-data rate standards utilizing MIMO, the importance of MIMO test solutions to verify that a device under test (DUT) can operate near capacity is critical to the goal of maximizing spectral efficiency. Ideally, a small, affordable test solution is desirable. After determining such a system is feasible, the ability to properly model such a MIMO system, which due to its small nature will be in the near-field (specifically the Fresnel region and near-Fraunhofer distances), is critical to calculating the capacity of the system and measuring DUT performance. In addition, a general near-field MIMO channel model can assist in the development of emerging near-field MIMO standards for high-data rate communications.

1.1.1 Importance of Small Chamber MIMO Test Solutions

In an effort to meet the demand for high-speed wireless networking to provide support for applications such as multimedia streaming and document sharing, multiple-antenna com-

munications are and will continue to be deployed. Multiple-Input Multiple-Output (MIMO) systems employ antennas arrays that increase capacity, spectral efficiency, and cell coverage [10]. MIMO systems can operate with many signaling techniques, including Bell Labs layered Space-Time (BLAST), Alamouti space-time code, vertical BLAST (V-BLAST) and Turbo-BLAST; all of the techniques leverage the spatial diversity of the antenna arrays at the transmitter and receiver [11].

Many recent and emerging standards serve to increase the adoption of MIMO technology, including IEEE 802.11n, 802.11ac and 802.11ax (Wi-Fi), Long Term Evolution (LTE) and LTE-Advanced (standards developed by the 3rd Generation Partnership Project (3GPP)), and WiMAX (IEEE 802.16). These standards utilize multiple antennas in both the base station and the mobile device. Inherently, MIMO systems are dependent on the spatial orientation of the antennas at both ends of the links and the geometry of the antenna arrays themselves. This spatial correlation, in addition to the multi-path fading of the wireless channel, will impact the performance of a wireless communications link [11]. Therefore, a simple over-the-air (OTA) test which does not take into consideration this correlation or fading is not sufficient for validating the throughput performance of a multiple antenna system. The development and deployment of next generation devices greatly depends on the ability to test and analyze the devices under realistic conditions; it is for this purpose that MIMO-OTA testing platforms are being developed.

Current MIMO-OTA testing platforms such as large anechoic chambers are expensive, running in excess of one million USD. Recent research has demonstrated that, for a reduced set of standard MIMO-OTA channels, a small anechoic chamber with a reduced array of probe antennas can be utilized. Such a small chamber can cost in the range of 200 thousand USD, a significant savings over the large chamber solutions. This can result in smaller

development costs for electronics manufacturers, which could serve to lower the cost of next-generation wireless devices for consumers, which could in turn assist in wider adoption of these technologies. A small chamber is also more portable, allowing it to be easily transported into a building through doorways, rather than assembled in a single location in a dedicated room without the option of relocating.

1.1.2 Importance of Near-Field MIMO Channel Models

High-data-rate near-field MIMO applications include LTE, LTE-A, millimeter wave systems such as 5G and 802.11ad, and HDMI replacements. All of these applications either can be tested in the near-field (specifically the Fresnel region and near-Fraunhofer distances) or operate in the near-field, and in either case a full characterization of the wireless communications channel is critical for defining system performance limits when developing a new technology and creating test metrics for throughput testing of an existing technology.

An effort to characterize a near-field MIMO communications channel must include an understanding of the propagation between the transmitter and receiver, specifically, the propagation between each transmitting antenna, and each receiving antenna. This propagation between antennas is defined by electromagnetic theory, and can be modeled using fields in the environment of the transmit and receive antennas (including near-field aspects of field equations). In addition, interactions with the environment that would affect this field must be accounted for, including reflections from environmental objects. It is extremely important to model as many relevant components of the environment as possible (making the model accurate), while keeping the model general enough to apply to other similar but not identical scenarios (making a robust model). A useful model framework should also allow for refinement (thus increasing accuracy) using real-world measurements to capture modeling

errors and phenomena that may not have been included in the model. An accurate and robust model will have the largest impact on, and benefit for, the field of near-field MIMO communications, and that impact and benefit are the motivations of this work.

1.2 Contributions, and Outline

The contributions of the research presented herein are:

- demonstrating the ability of a cost-effective small anechoic chamber for MIMO-OTA testing to reproduce specified electric fields corresponding to standardized MIMO-OTA test cases [12]. This work showed the difficulty of recreating a standard MIMO test environment in a small test chamber; however for certain configurations of chamber size, antenna number and spacing, test zone size, and frequency, it was demonstrated that such an environment can be created in a small test chamber.
- channel models and the corresponding capacity between MIMO arrays located in the near-field. This framework utilizes electric field equations for antennas which include terms that are normally negligible in the far-field.

In addition, Fig. 1.2 includes a flowchart for the contributions of chapters 4 and 5. This flow chart will be used as a guide through these chapters. The additional contributions presented on the flowchart (plus an additional contribution related to MIMO channel analysis) are:

- A generalized numerical model describing the channel between a log periodic antenna and a dipole, each of arbitrary spacing and orientation, to calculate the channel vs. receiver dipole position in a test zone.

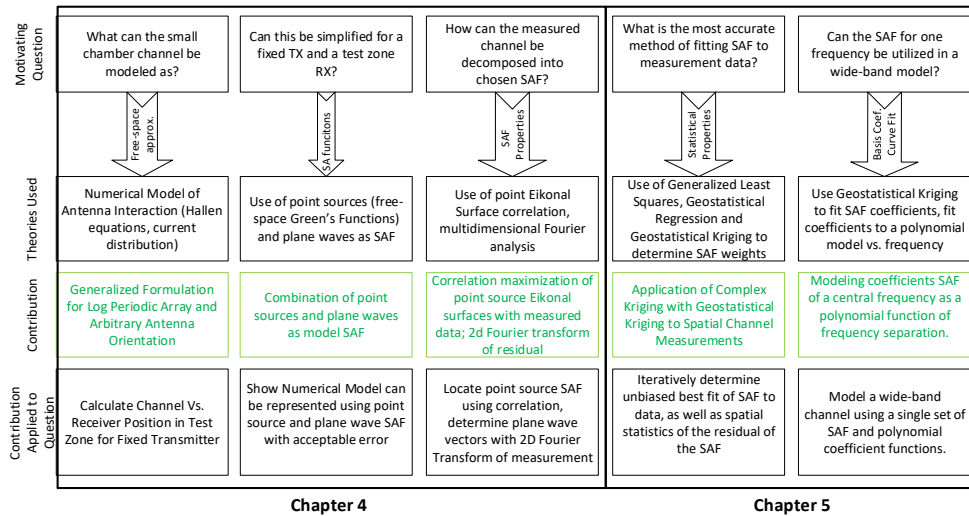


Figure 1.2: Contribution Flowchart for Chapters 4 and 5

- A method of using both point source fields and plane waves as joint spatial attribute functions (SAFs) to accurately describe the numerical channel model or a measured channel as a concise sum of functions with acceptable error.
- A method of fitting point source functions to a numerical or measured channel using a phase correlation maximization search, then use two-dimensional Fourier analysis to refine the approximation with plane waves.
- Combining methods of Complex Kriging, Geostatistical Regression and Geostatistical Kriging to statistically model the residual of the SAF function approximation to further refine the channel estimate. Applied this method to an extensive measurement campaign performed in a small anechoic chamber.
- An extension of the narrowband SAF plus residual model to a wideband channel model, utilizing frequency-scaled SAFs and polynomial coefficient and parameter models. This

yields a wideband SISO channel model of the small anechoic chamber which completely describes the channel as a mathematical function of frequency and receiver position in a test zone.

- An application of the small anechoic chamber wideband SISO channel models to wideband MIMO channel model, and an extensive analysis of the MIMO channel properties of the modeled small anechoic chamber.

This proposal is organized as follows:

- Chapter 2 presents fundamental background information on near-field electromagnetics and MIMO topics, anechoic chambers, and Kriging, as well as an overview of recent literature in this field. Also included is a preliminary investigation into simple Hertzian dipole near-field MIMO channel models, and
- Chapter 3 presents a computational electromagnetic analysis of the feasibility of small anechoic chambers for MIMO-OTA field synthesis.
- Chapter 4 presents a numerical near-field free-space channel model and a method for selecting and fitting a set of mathematical spatial attribute functions to a measurement set or sampled numerical model. This results in a narrowband functional model of the channel.
- Chapter 5 presents two extensions of the narrowband functional channel model, one refining the model by using a statistically-informed estimate of an additive residual, and the other extending the model to a wideband model. These model extensions are

applied to an extensive small chamber measurement campaign data set and verified for accuracy.

- Chapter 6 presents an extensive application of the small chamber channel model to a MIMO channel analysis of the small chamber, providing insight as to the performance of MIMO systems in a small anechoic chamber.

CHAPTER 2

Background

This chapter contains all relevant background to subsequent contributions. Fundamental concepts from the field of wireless communications relevant to the research performed for this dissertation are outlined. A literature review containing recent, relevant research in the areas of small anechoic chambers and near-field MIMO channel modeling will be performed. A section of preliminary investigations is included to show our initial work and analysis that preceded the contributions in this dissertation.

2.1 Fundamental Concepts

In this section, fundamental concepts in single-input single-output (SISO) and MIMO wireless communications, anechoic chamber theory, and antennas and electric fields in the near-field will be reviewed.

2.1.1 SISO channels

This subsection will serve as a quick review of fundamentals of SISO wireless channels, consisting of a single transmitting antenna and single receive antenna. Wireless channels are linear in nature; if we assume the channel to be time-invariant (does not change over time), causal (outputs can only happen concurrent with or after inputs), and time-dispersive (input energy is spread out over time at the output), we can describe a relationship between its input and output as an impulse response h in the time domain, or a transfer function H in the frequency domain [11]. If the wireless channel is truly time-invariant, then H is

completely deterministic.

Wireless channels in most real-world situations are time-varying and can be modeled as such with a time-dependent transfer function $T(t,f)$. This is due to motion in a real-world environment, with various reflections of the signal bouncing off and scattering from moving objects in the environment and adding constantly-varying copies of the signal constructively or destructively at the receiver. This phenomenon is known as fading, and the channel between the transmitter and receiver can change rapidly (known as fast fading) or slowly (known as slow fading). Unfortunately, this makes both analysis and communications systems much more complex. However if the channel changes slowly in time in relation to independent channel accesses (and the channel is sufficiently low-bandwidth), i.e. if the channel exhibits slow fading, it can be modeled as time-invariant (i.e. H can be used in lieu of T) for analysis. In other words, in this scenario the channel has a sufficiently long coherence time for the utilized communications scheme [11]. For each access of the channel, however, H can have different random values in this scenario. If H is independent and identically distributed (I.I.D.) for each channel access, the channel distribution can be characterized and modelled as a random variable. (Characterization and modeling of channels where the coherence time is short relative to the communications system (i.e. fast fading) is possible, but is outside the scope of this dissertation.)

If a channel is considered narrowband (ideally modeled as a single sinusoid at a frequency f_0), the impulse response $h(t)$ becomes valid at a single frequency $H(f_0)$ in the frequency domain, and it becomes a single complex constant h , or complex gain. This constant can be multiplied by the transmitted signal in either the frequency domain or time domain to produce the received signal [11]. This complex constant h will affect the amplitude and phase of the narrowband signal. Communications systems such as orthogonal frequency division

multiplexing (OFDM), where a wideband channel is divided into independent narrowband orthogonal sinusoidal channels (subcarriers) with amplitude and phase representing data in symbols of duration less than the coherence time, are designed in such a way that can utilize independent channel estimations h for each subcarrier and symbol period(s) [13].

In addition to the effect of the complex channel impulse response, noise is added to the received signal in a channel model, usually modeled as complex additive white Gaussian noise (AWGN) (i.e. both the real and imaginary components of the noise follow a Gaussian distribution, and are spectrally uniform) [11]. Thus, a narrowband SISO channel can be modeled as:

$$y(t) = h \cdot x(t) + n(t) \quad (2.1)$$

2.1.2 MIMO

If both the transmitter and receiver utilize multiple antennas, the system becomes multiple-input multiple-output (MIMO). Each pair of transmit and receive antennas is assumed to represent an independent channel that can be modeled as in Eq. 2.1. If we consider the transmitted signal as a vector \vec{x} of length N_t (the number of transmit antennas), the received signal as a vector \vec{y} of length N_r , an impulse response between TX antenna i and RX antenna j as h_{ji} , and an AWGN vector \vec{n} of length N_r , then the vectors \vec{x} and \vec{y} can be related by the following equation:

$$\vec{y}(t) = \mathbf{H}\vec{x}(t) + \vec{n}(t) \quad (2.2)$$

where \mathbf{H} , the $N_r \times N_t$ channel matrix, consists of elements h_{ji} , the complex gain between each pair of transmit and receive antennas [11]. This can be described as a vector Gaussian

channel [13].

In short, each individual received signal is the sum of a gain-adjusted and phase-shifted version of each and every transmitted signal plus some additive AWGN. The channel matrix, determined by environment, determines just how much of each transmitted signal is received at each antenna. The greater the distance between antennas in the transmit array, and the greater the distance in antennas in the receive array, the greater the variation in the combination of signals received at each antenna at the receiver. This spacing (which can be adjusted and optimized to meet the needs of communications systems), provides a spatial dimension to the system, or in other words, allows for spatial multiplexing of multiple data streams between the transmitter and receiver [13]. In certain environments (i.e. certain channel matrix formulations and distributions), utilizing MIMO can significantly increase the capacity of a communications link over a similar SISO link.

Channel Matrix Analysis and Decomposition

To evaluate the benefits of MIMO, an analysis of the channel matrix \mathbf{H} is performed. \mathbf{H} is a matrix that in the context of Eq. 2.2 can be considered a linear transformation between the transmit and receive vectors. A linear transformation can be decomposed using singular value decomposition (SVD) into a product of three matrices: a rotation matrix U (unitary matrix, i.e. the Frobenius norm of this matrix equals 1), a scaling matrix Λ (diagonal matrix consisting of the singular values of \mathbf{H}), and another rotation matrix V^H (another unitary matrix; H represents the Hermetian operator, i.e. conjugate transpose [13]). If we pre-multiply the transmit signal vector \vec{x} by V ($\vec{x}(t)$), and post-multiply the received signal vector \vec{y} (and thus also the noise vector) by U_H ($\vec{y}(t)$ and $\vec{n}(t)$), (which preserves the norm,

and thus power values, of \vec{x} , \vec{y} , and $n(\vec{t})$), then the channel can be rewritten as [13]:

$$\vec{y}(\vec{t}) = \mathbf{\Lambda}\vec{x}(\vec{t}) + \vec{n}(\vec{t}) \quad (2.3)$$

Which, due to the diagonal matrix $\mathbf{\Lambda}$ can be written as a set of parallel Gaussian channels:

$$\tilde{y}_i = \lambda_i \tilde{x}_i + \tilde{n}_i \quad (2.4)$$

where i is the eigenvalue matrix index ii , of which there are $R_{\mathbf{H}}$ values (rank of \mathbf{H}). The power of the transmitted signal \tilde{x}_i is equal to P_i , and the received signal power is thus $P_i \cdot \lambda_i^2$. (The sum of all P_i must equal the total transmitted power P_t .) The power of the noise at the receiver is N_0 . [13] The signal to noise ratio (SNR) of each parallel Gaussian channel, i.e. the signal power received divided by the noise power received, is:

$$\frac{P_i \cdot \lambda_i^2}{N_0} \quad (2.5)$$

General MIMO Capacity

From information theory, the Shannon capacity of a SISO channel with normalized bandwidth is equal to $C = \log_2(1 + SNR)$. Using the derived expression for SNR, the capacity for each parallel channel becomes:

$$C_i = \log_2 \left(1 + \frac{P_i \cdot \lambda_i^2}{N_0} \right) \quad (2.6)$$

The total MIMO channel capacity is equal to:

$$C = \sum_{i=1}^{R_H} \log_2 \left(1 + \frac{P_i \cdot \lambda_i^2}{N_0} \right) \quad (2.7)$$

This formula for instantaneous narrowband MIMO capacity was first introduced by Foschini and Gans [14]. For a wideband MIMO channel, the wideband capacity becomes an average of narrowband capacities [11]. The wideband MIMO channel is sampled at regular frequencies Δf for some bandwidth W to yield a series of narrowband channel matrices $\mathbf{H}[f]$, each of which is used in the narrowband capacity formula, and averaged over the range of frequencies sampled (2.8) [11]:

$$C_X = \frac{1}{W} \sum_{f=1}^F \log_2 \left[\det \left(\mathbf{I} + \frac{\rho}{M_{Tx}} \tilde{\mathbf{H}}[f] \tilde{\mathbf{H}}^H[f] \right) \right] \Delta f \quad (2.8)$$

where F is the number of frequencies for which \mathbf{H} is sampled, H is the Hermitian transpose operator, ρ is the linear transmit SNR, M_{Tx} is the number of transmit (probe) antennas, and \mathbf{I} is the identity matrix. $\tilde{\mathbf{H}}$ is the normalized channel matrix (2.9):

$$\tilde{\mathbf{H}}[f] = \frac{1}{\sqrt{\frac{1}{M_{Rx} M_{Tx} F} \sum_{i=1}^{M_{Rx}} \sum_{j=1}^{M_{Tx}} \sum_{k=1}^F |h_{i,j,k}|^2}} \mathbf{H}[f] \quad (2.9)$$

where M_{Rx} is the number of receiver antennas, and $h_{i,j,k}$ is the $(i, j)^{\text{th}}$ element of $\mathbf{H}[f(k)]$. Essentially, this is normalizing $\mathbf{H}[f]$ by the average element magnitude of $\mathbf{H}[f]$ across all frequencies.

Waterfilling Power Allocation and Capacity

The optimal distribution of power for each independent channel, P_i^* , can be determined using a waterfilling algorithm. Waterfilling can occur if the transmitter has knowledge of the channel matrix \mathbf{H} . The transmitter determines the eigenvalues, $\vec{\lambda}^2$, of the channel matrix. Then the transmitter initializes a variable μ , which is iteratively updated and will be used to calculate the optimal power allocation.

$$\mu = \min \left(\frac{N_0}{\vec{\lambda}^2} \right) + \frac{P_t}{R_{\mathbf{H}}} \quad (2.10)$$

Another variable p gets initialized, which is the sum of allocated power given the current value of μ :

$$p = \sum_{n=1}^{R_{\mathbf{H}}} \max \left(\mu - \frac{N_0}{\vec{\lambda}_n^2}, 0 \right) \quad (2.11)$$

the following steps are performed iteratively until the difference between P_t and p is arbitrarily small:

$$\mu = \mu + \frac{P_t - p}{R_{\mathbf{H}}} \quad (2.12)$$

$$p = \sum_{n=1}^{R_{\mathbf{H}}} \max \left(\mu - \frac{N_0}{\vec{\lambda}_n^2}, 0 \right) \quad (2.13)$$

This iteratively adds power to channels with high eigenvalues first, then progressively raises the level of μ thus adding power to subcarriers with sufficiently high eigenvalues relative to μ until all power has been allocated. Once the value of μ is determined that allocates all

power, power is optimally assigned to independent channels as [13]:

$$\vec{P}^* = \max\left(0, \mu - \frac{N_0}{\bar{\lambda}^2}\right) \quad (2.14)$$

MIMO Channel Metrics

Two metrics of the channel matrix can indicate how good a channel is for MIMO communication. First, the rank $R_{\mathbf{H}}$ of the channel matrix, or the number of non-zero eigenvalues, indicates the number of spatial degrees of freedom. If a channel matrix is full-rank, then it maximizes the dimension of the MIMO channel for the given system with N_t transmitting antennas and N_r receiving antennas [13]. Second, the condition number of the matrix $\gamma = \frac{\max(\vec{\lambda})}{\min(\vec{\lambda})}$, indicates how spread out the singular values of the channel matrix are. If the singular values are uniformly distributed, then the condition number is equal to 1 and the matrix is considered well-conditioned. The closer the condition number gets to 1, the larger the capacity in high SNR conditions [13].

Several properties play into the definition and characterization of a MIMO channel. Deterministic (static) properties that contribute to the channel include transmit and receive array orientation (often used are uniform linear arrays (ULA) for analysis) and antenna spacing, number of resolvable paths in the angular domain (and whether one of these paths is line of sight) [13]. Analytical methods to determine the rank and condition number of these deterministic channels is well-studied, particularly in the far-field. General trends reveal that small antenna separation in both transmit and receive arrays in the line-of-sight case yield no spatial degree of freedom gain, large antenna separation in the transmit array or receive array provide a spatial degree of freedom gain (even in the line-of-sight case), and multipath channels with large angular separation between multipath components provides

a spatial degree of freedom gain even with low separation in the transmit array or receive array [13].

Stochastic MIMO Channels

As discussed previously, the channel matrix may be stochastic rather than deterministic due to the presence of a fading channel. The standard assumptions in these stochastic models are that the channel exhibits sufficient coherence time such that discrete samplings of the random process (i.e. constant multiplicative complex matrix entries) can be made, and that each entry of the matrix is I.I.D. The ability of a stochastic channel matrix to represent a rich multipath environment can be analyzed through transformation of the channel matrix into an angular domain representation (i.e. pre- and post-multiplying the channel matrix by unitary matrices constructed from basis vectors for the transmit and receive signal spaces, or in other words Inverse Discrete Fourier Transform (IDFT) matrices). The elements of the angular domain representation matrix correspond to transmitter and receiver angular bins corresponding to direction of departure and direction of arrival respectively, i.e. one resolvable path. Elements of this matrix above a certain threshold indicate that the channel has at least one multipath component along this resolvable path. Assume that elements below the defined threshold are zero. The rank of the angular channel matrix can be defined as the minimum between the number of non-zero rows and non-zero columns [13].

Rayleigh Fading

One common stochastic MIMO channel model is the I.I.D. Rayleigh fading model, where each element in the channel matrix is I.I.D. circularly-symmetric complex Gaussian. The distribution of the magnitude of this complex random variable (the square root of sum of the squares of the real and imaginary components) follows a Rayleigh distribution. If we

investigate the angular domain channel matrix of such a process, we see that the Rayleigh channel has I.I.D. Gaussian distribution in the angular domain as well, indicating that the expected value in every resolvable path, i.e. the expected value of a Rayleigh random variable (which is non-zero by definition) should be above the threshold. This means that every resolvable path is utilized between the transmitter and receiver, and the simulated channel is richly scattered [13]. It should be noted that because each of the two Gaussian processes that constitute the real and imaginary parts of the channel matrix are zero mean, there is no dominant (line-of-sight) path between the transmitter and receiver.

Rician Fading

In the case where a line of sight path can be modeled as dominant, but there is also a richly-scattered channel present, a Rician fading model is appropriate. In essence, Rician fading is just Rayleigh fading, except the real and imaginary Gaussian random variable components are not zero-mean, with the real and complex component means equaling the complex gain of the line-of-sight path between transmitter and receiver. For a Rician channel model, this complex line-of-sight gain must be determined for each transmit-receive antenna pair either analytically or experimentally. Then, the ratio of energy in the line-of-sight path to the energy in the scattered paths κ must be determined [15]. The resulting channel matrix entry is the following assuming a variance of $\sigma^2 = h_{ijLOS}$:

$$h_{ij} = \sqrt{\frac{\kappa}{\kappa + 1}} h_{ijLOS} + \sqrt{\frac{1}{\kappa + 1}} \mathcal{CN}(0, |h_{ijLOS}|^2) \quad (2.15)$$

where \mathcal{CN} is the complex normal distribution. It should be noted that when κ is zero, the channel matrix becomes Rayleigh, and if κ approaches infinity, the channel matrix becomes deterministic with $h_{ij} = h_{ijLOS}$.

MIMO Channel Clusters

Realistic MIMO channel models involve one or multiple multipath clusters impinging on a receiving array. Each multipath cluster is centered around a central angle of arrival, and consists of numerous multipath elements, each of which follows a statistical distribution in time (delay τ), azimuth angle ϕ (Power Azimuthal Spread (PAS)), and elevation angle θ . Each multipath component within a cluster is selected from a fading distribution, which is correlated to the distributions in time and angle [11]. With a set of randomly generated multipath components following these distributions, a channel matrix \mathbf{H} can be generated from the sum of their components. Several standardized MIMO channel models have been developed through the modeling of multipath clusters, including Saleh-Valenzuela, Extended Saleh-Valenzuela, COST 273, Random Cluster Model (RCM), and others [11].

Mutual Coupling at the Transmitter and Receiver

Mutual coupling between elements of the transmitter can have an effect on the MIMO system capacity. The relation between the source voltage \vec{v}_s and terminal (antenna) voltage \vec{v} is [16]:

$$\mathbf{Z}_T = \mathbf{Z}^T(\mathbf{Z}^T + \mathbf{Z}_S)^{-1} \quad (2.16)$$

$$\vec{v} = \mathbf{Z}_T \vec{v}_s \quad (2.17)$$

where \mathbf{Z}_S is the diagonal matrix of N source impedances and \mathbf{Z}^T is the open-circuit, N_t port transfer impedance matrix at the transmitting end. Therefore \mathbf{Z}_T in 2.16 becomes part of the channel used in capacity analysis, i.e. $\vec{y} = \mathbf{H}\mathbf{Z}_T\vec{x}$.

Mutual coupling between elements at the receiver can also have an effect on MIMO system

capacity [17]. The matrix relation (\mathbf{Z}_R) between the voltage induced by the antennas without mutual coupling ($\mathbf{HZ}_T\vec{x}$) and with mutual coupling (\vec{y}) is:

$$\vec{y} = \begin{bmatrix} 1 & -\frac{Z_R^{1,2}}{Z_{L1}} & \cdots & -\frac{Z_R^{1,N-1}}{Z_{L1}} & -\frac{Z_R^{1,N}}{Z_{L1}} \\ -\frac{Z_R^{2,1}}{Z_{L2}} & 1 & \cdots & -\frac{Z_R^{2,N-1}}{Z_{L2}} & -\frac{Z_R^{2,N}}{Z_{L2}} \\ \vdots & \vdots & \ddots & \vdots & \vdots \\ -\frac{Z_R^{N-1,1}}{Z_{L(N-1)}} & -\frac{Z_R^{N-1,2}}{Z_{L(N-1)}} & \cdots & 1 & -\frac{Z_R^{N-1,N}}{Z_{L(N-1)}} \\ -\frac{Z_R^{N,1}}{Z_{LN}} & -\frac{Z_R^{N,2}}{Z_{LN}} & \cdots & -\frac{Z_R^{N,N-1}}{Z_{LN}} & 1 \end{bmatrix} \mathbf{HZ}_T\vec{x} = \mathbf{Z}_R\mathbf{HZ}_T\vec{x} \quad (2.18)$$

where Z_{L_n} is the load impedance of receiver port n , and $Z_R^{m,n}$ is the mutual impedance at the receiver between ports m and n . The resulting channel matrix including mutual coupling \mathbf{H}_M , which can be used in subsequent capacity analysis (as described in 2.1.2), is $\mathbf{H}_M = \mathbf{Z}_R\mathbf{HZ}_T$ [2].

2.1.3 Near-Field Topics and Mutual Coupling

In the following subsection, we discuss the distinction between near- and far-field, and properties of mutual coupling.

Near-field Vs. Far Field Ranges

An antenna radiating several modes has three regions of space defined in terms of wavenumber $k = \frac{2\pi}{\lambda}$, the radius of the minimum sphere of the antenna r_0 , and $N = [kr] + n_1$ where r is the radius from the center of the antenna, the brackets indicate the largest integer smaller than or equal to kr , and n_1 is an integer which depends on the accuracy desired for the system, which can be equal to 5 or less for small values of kr [18]. The three ranges of

space are evanescent ($r_0 \leq r \leq N/k$), Fresnel region (near field) ($N/k \leq r \leq 4N^2/\pi k$), and Fraunhofer region (far field) ($4N^2/\pi k \leq r \leq \infty$). It should be noted that the Rayleigh distance R (the boundary between near and far fields), for a source with minimum sphere of diameter $D = 2r_0$, is often defined as $R = \frac{2D^2}{\lambda}$. This distance is approximate, and making far-field assumptions near the Rayleigh distance can still produce significant phase error.

Additional Mutual Coupling Topics

Mutual coupling effects between closely-spaced linear antennas can be modeled using electric and magnetic fields produced at near-distances, which can be obtained by determining the magnetic vector potential A . In [19], sections 23.1 and 23.2 outline a rigorous mathematical analysis using sinusoidal current assumptions for determining the near field for linear antenna (e.g. general dipole antennas) separations greater than $\frac{\lambda}{10}$. This antenna separation is more than sufficient for use in our research. Mutual impedance and self-impedance are calculated in section 23.3 using equations relating induced open circuit voltage to incident electric field and current. Section 23.5 utilizes the mutual/self impedance matrix along with driving voltages for each antenna in an array to determine the input currents of each antenna, which along with the sinusoidal assumption that defines each element current $I(z)$, can be used to define the electric and magnetic fields produced by the array [19].

2.2 Literature Review

In this section, we reviewed recent literature related to our research efforts. A summary of this literature was included here to frame the context of our research, and to present the origin and evolution of some of the techniques and methods used in our research. Our literature review encompassed the areas of MIMO-OTA testing and near-field MIMO channels and

corresponding capacity.

2.2.1 MIMO-OTA Testing

This subsection reviews literature on MIMO-OTA testing topics. This literature will help place the contributions of Chapter 3 of this document in context, and help the reader understand the state of the art in MIMO-OTA testing. Topics of the literature reviewed in this subsection include MIMO-OTA chamber types, MIMO-OTA test system calibration, standard channel emulation in anechoic chambers, full-ring MIMO-OTA plane wave field synthesis, and partial-ring MIMO-OTA field synthesis.

MIMO-OTA Chamber Types

There are several different proposed MIMO-OTA systems in the literature: full ring [20, 21] and full-sphere, partial ring [22], and reverberation chamber [23]. All of these systems are designed to emulate the spatial distribution of power that would occur in a multipath environment. The spatial distribution of power is dependent on multiple incident waves of different power levels and angles of arrival. The incident power as a function of angle in a multipath environment can be modeled as multiple clusters, each exhibiting a Laplacian Power Azimuthal Spectrum (PAS). This angular dependence of the incident power is important as the achievable data rates are inherently tied to the orientation of the antennas.

The full-ring system includes evenly-spaced MIMO-OTA probes in a circle around the device-under-test (DUT) [21]. This configuration enables the creation of multiple clusters of energy impinging on the DUT. The generation of multiple clusters makes it possible to test many different wireless environments, but at the cost of a large chamber with a high number of probes and hardware. Efforts to shrink a full-ring system into a small chamber with ring radius of 0.5m have been shown to be successful in [24], however these efforts have

dealt with target zone correlation error rather than accuracy of field synthesis.

The reverberation chamber is an anechoic chamber that has reflectors that redirect the signals to distribute the power over different angles [23]. These facilities are also large and the control of the power distribution is limited. Finally, the small chamber implementation considered for our work uses a subset of antennas with respect to the full ring to synthesize a single cluster, or partial ring. The size and fewer number of probe antennas of the partial ring small chamber makes it more cost effective than its full-sized or full-ring counterpart, but the number of wireless environments that can be generated is limited [22]. While a single cluster does not provide the spatial diversity that results in the highest MIMO data rates, it does provide a standardized, realistic, and repeatable environment in which to perform MIMO-OTA testing [25].

Through simulation of a single cluster with Laplacian PAS field, it has been shown that a low number of probes can be used to generate a desired electromagnetic field in a test zone [25]. Previous work, however, only focuses on minimizing the number of probes, and does not focus on constraining these probes to a small chamber. This previous work therefore does not investigate parameters such as chamber dimensions, antenna arrangement, or frequency.

MIMO-OTA Test System Calibration

A modified test zone field compensation technique for calibrating multi-probe antenna measurement systems was presented in [26]. This method yielded performance similar to traditional calibration methods and can be used in environments with high levels of signal reflections. This technique was expanded in [27], allowing for full 3-D antenna pattern measurements without an anechoic measuring environment. Small-antenna pattern mea-

measurements can be made in non-anechoic environments where multi-reflection amplitudes are small relative to primary reflections. This technique can also be used to calibrate out the reflections caused by multiple antennas in an anechoic chamber MIMO-OTA test system. These methods were extended in [28] to multipath environment synthesis in a spherical test zone with a limited number of probes. Arbitrary electromagnetic environments can be synthesized with this method (including near-field effects), including near-field environments, due to spherical-wave theory. Spherical wave theory will be outlined in Chapter 3, in section 3.1.1.

Standard Channel Emulation in Anechoic Chambers

The literature has several papers exploring MIMO channel emulation based on various standards in full-ring anechoic chambers, specifically the effect of many chamber parameters (mostly probe antenna configurations) on numerous channel emulation metrics. The capability to recreate required radio propagation channel characteristics including power delay profile, Doppler spectrum, and spatial auto-correlation in models such as 3GPP SCM, SCME and IEEE 802.11n in a full-ring MIMO-OTA anechoic chamber test zone was investigated in [29]. A relation between number of probe antennas and test zone size for accurate spatial channel emulation was established in this work. Considerations of probe antenna spacing, radiation patterns, and mutual coupling and their effect on channel emulation accuracy were further investigated in [30]. The antenna correlation and throughput performance of three channel models were investigated for three antenna separation configurations in this work. An investigation into the ratio of probe ring radius to the test zone radius and its effect on channel emulation accuracy requirements at various frequencies was investigated in [31].

In addition to probe antenna configuration, the effects of device under test configuration

on MIMO-OTA full-ring test system requirements have been investigated in the literature. The impact of device under test antenna patterns (specifically variation in directivity) on the number of probe antennas necessary for plane wave synthesis (and equivalent induced voltage (EIV) technique, a technique with almost identical results for large MIMO-OTA setups) and prefaded signal synthesis was performed in [32]. This impact was measured using metrics of received voltage and spatial correlation accuracy. Simulation and measurement showed that higher variation in directivity requires a higher number of probes for comparable accuracy.

Beyond full-ring configurations, some papers have explored 3-dimensional channel emulation. An investigation into 3-D spatial correlation channel model emulation in a spherical probe array MIMO-OTA test setup was performed in [33]. A framework to emulate any spherical incoming power spectrum, with optimal emulation accuracy and low computational complexity, was presented in this work.

Two methods of MIMO-OTA channel emulation exist in the literature, prefaded signal synthesis (which relies on correlation within the test zone) and plane wave synthesis, both of which apply weights to the signal applied to each probe antenna. In [34], mapping of channel models onto MIMO-OTA probe antennas, specifically through generation of complex antenna coefficients through prefaded signal synthesis and plane wave synthesis, is explored. Evaluation and verification through simulation was performed, with the benefits of each of the two antenna coefficient generation methods analyzed. The cases where each would be appropriate were outlined. Plane wave synthesis methods were determined to be superior for the scenario of a limited antenna ring radius, and therefore would be the antenna coefficient method of choice for a small chamber environment, the focus of our work.

Full-ring MIMO-OTA Plane Wave Field Synthesis

Several papers in the literature investigate plane wave synthesis methods of channel emulation for MIMO-OTA systems. A review of existing investigations on MIMO-OTA test methodology is performed in [35], and rules for the required number of probes as a function of test zone size in wavelength for a desired uncertainty or accuracy in test zone field synthesis are presented. The accuracy in test zone field synthesis is defined in terms of deviation from a target electric field. Probe orientation error and location mismatch and their effect on plane wave synthesis of an electric field in a MIMO-OTA full-ring test zone are considered in [36]. A finite-difference time-domain (FDTD) simulation was used to determine the performance deterioration caused by these errors. It was shown that radial location mismatch error is found to have the greatest effect on performance.

The sufficiency and advantage of a full-ring system over a full-sphere configuration has been investigated in the literature. In [37], a 2-D circular array (full-ring) for field synthesis in MIMO-OTA testing is investigated in terms of plane wave synthesis analysis, and a case for a 2-D full-ring test system over a 3-D full-sphere test system is made. Many channels and channel models have constrained PAS to the horizontal plane. The use of 2-D systems provides a channel emulation system cost- and complexity-reduction.

Channel emulation through the synthesis of multiple simultaneous plane waves in a test zone is possible (including cluster models formed through the sum of numerous plane waves following an angular spectrum), and papers have investigated the requirements of a full-ring system to synthesize such a field. A synthesis and measurement of single- and multi-plane wave fields with multiple angle of arrival (AoA) and weightings is performed in [38], with phase and power deviations of the synthesized field investigated. It is shown that the

superposition of multiple plane waves with different AoA can cause deep fading, which can cause phase jumping and inaccuracies in measurements.

Partial-ring MIMO-OTA Field Synthesis

There has been some work in the literature regarding partial-ring anechoic chamber MIMO-OTA systems. In [25], the number of probe antennas required for generating a single Laplacian PAS cluster for varying angular spreads and test zone sizes in an anechoic chamber is established. A Laplacian cluster target field to model this channel is generated through the sampling of a Laplacian distribution to determine the amplitude of a series of plane waves from varying AoA, each with random, uniformly-distributed phase. This paper investigated partial ring systems, including probe antenna sector angle and number of antennas, and their effect on synthesized field accuracy. This paper is the basis of much of our small chamber work presented in this proposal. It, however, does not discuss how non-ideal effects such as reflection contributions in a small chamber would affect the field synthesis accuracy, which is a focus of our work.

2.2.2 Near-Field MIMO Channels and Capacity

This subsection reviewed literature near-field MIMO channels and capacity. This literature helps to place the work in Chapters 4 through 6 of this document in context, and helps the reader understand the state of the art in near-field MIMO channel modeling. Topics included in this subsection include short-range MIMO channels, near-field scatterers in MIMO systems, near-field MIMO channel modeling, and near-field MIMO capacity improvement.

Short-Range MIMO Channels

Short-range MIMO communications have been described in the literature for over a decade, with papers going back to at least 2005 found in a literature search [39]. Such systems are mostly at frequencies in excess of 6 GHz, and are often in the millimeter wave range. Due to the high frequencies involved in this type of communication, the term ‘short range’ may or may not actually be in the near field. Early work in this area in [39] describes the use of a ‘spherical-wave model’ for analysis of arrays with separation distance in the near-field. This analysis, however, turns out to be a spherical-geometry approximation using a $\frac{1}{r}$ line-of-sight path loss approximation based on inter-element separation distance rather than inter-array separation distance, and is thus a far-field approximation of a near-field channel rather than a true spherical-wave analysis in the typical sense. This work shows that using this approximation produces a more accurate estimation of capacity than assuming a plane wave (i.e. flat wave front) impinging on the entirety of the receive array.

Essentially all papers reviewed in this area utilize the same far-field line-of-sight path loss assumptions for capacity analysis [40–42]. Also, these papers note that the close spacing of corresponding antenna elements at the transmitter and receiver result in a strong line-of-sight path, and relatively low interference from neighboring transmit elements, thus producing a series of almost parallel data streams without multipath components, with this assumption being especially valid at higher frequencies. In [40] (and to a less rigorous extent in [41]), optimal element spacing was investigated and verified through measurement. In [42], a short-range 2×2 ultra-wideband MIMO system is shown to have double the capacity of a SISO system with the same characteristics, indicating that a parallel-stream assumption for the ideal case of perfect array alignment is valid.

Near-Field Scatterers in MIMO Systems

A couple papers were encountered that modeled the effect of near-field scatterers near a MIMO array on capacity. One paper, [43], discussed the effect of near-field scatterers on the mutual coupling of a MIMO antenna array and the corresponding effect on channel and capacity. This paper modifies a previously proposed model for mutual coupling for MIMO systems to include and characterize the effect of near-field scatterers. This modification is validated, then used to accurately obtain correlation properties between antenna elements, and as a result measure the effect on system capacity. Another paper, [44], investigated through modeling the effects of the equipment case and human user on a MIMO system in a handset.

Near-Field MIMO Channel Modeling

A small number of papers were found which modeled the near-field MIMO channel in a 2×2 system where each array consisted of two elements utilizing some method of orthogonality. The first set of these papers utilized a small electric dipole and a small magnetic dipole in each array. In [2], the 2×2 system with a short electric dipole and small solenoidal loop (Figure 2.1) is analyzed using the assumption that each element produces a TM_{10} and TE_{10} mode respectively (Figure 2.2), which are orthogonal. An equivalent circuit diagram is presented in Fig. 2.3. Combining spherical wave propagation of each element and coupling matrices at the transmitter and receiver, the effective channel matrix is calculated and near-field MIMO capacity is determined.

An almost identical approach involving a pair of electric and magnetic dipoles at the transmitter and receiver is outlined in [45], though this paper neglects the mutual coupling of the transmit and receive arrays, and lacks the mathematical rigor of [2], but includes an

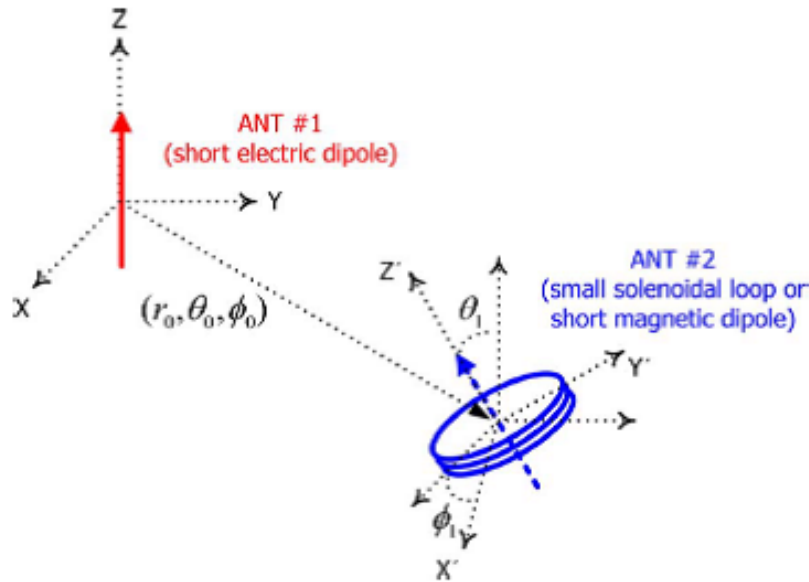


Figure 2.1: 2 Element Dipole and Loop Antenna Array [2]

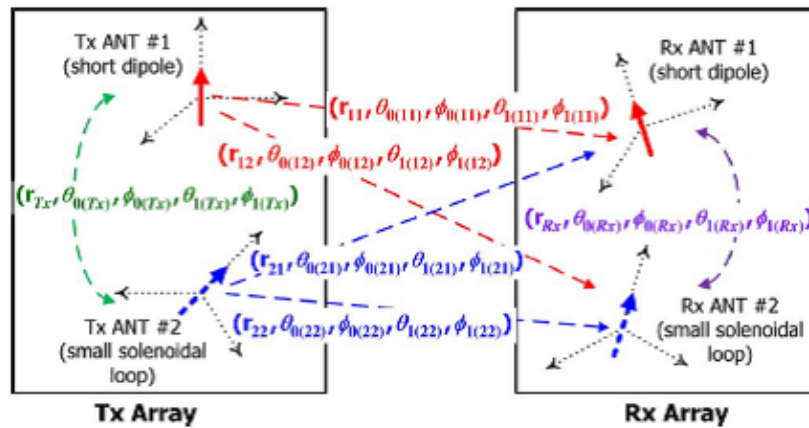


Figure 2.2: Near-Field 2×2 MIMO Example [2]

indoor measurement campaign at 1 MHz comparing the ratio of MIMO capacity to SISO capacity.

The second type of paper found analyzing near-field MIMO was one utilizing orthogonal polarizations of two electric dipoles at both the transmitter and receiver. In [46], the au-

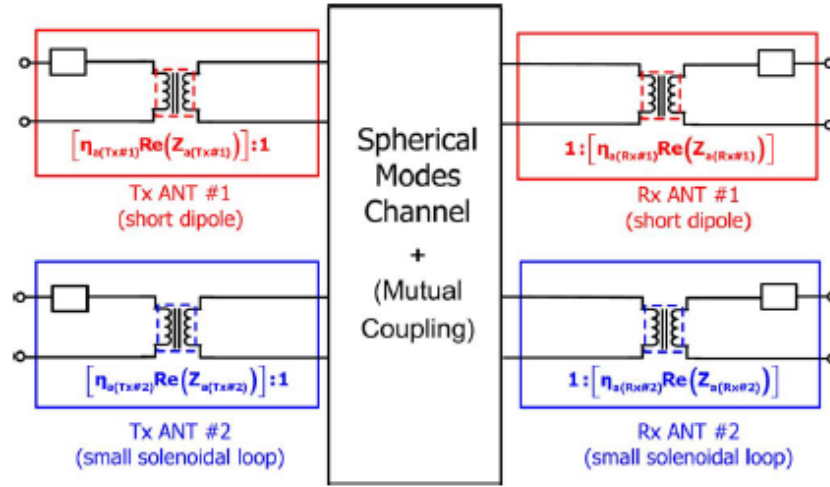


Figure 2.3: Equivalent Circuit for Near-Field MIMO System [2]

thors of which also wrote [2], uses an almost point-for-point identical analysis in this paper, with every pair of antennas using a TM_{10} mode this time. All other aspects of analysis are identical, including the mutual coupling formulations, equivalent circuit description, matrix equations, etc. While this work is similar to the work presented in the Preliminary Investigations section of this dissertation chapter, there are three distinct differences. First, the dipoles modeled in our analysis are parallel and co-planar, and thus co-polarized and not orthogonally polarized. Second, we compare near-field to far-field capacity utilizing a normalized channel, whereas [46] does not normalize and only offers capacity values for a small range of near-field distances. Third, our formulation utilizes the Hertzian dipole equation which encapsulates all propagation modes, while this paper utilizes a single mode spherical mode approximation of the electric field, and thus our model is more robust. In short, our preliminary research could be considered more comprehensive and extensible than that in [46].

Near-Field MIMO Capacity Improvement

Methods to increase the capacity of near-field MIMO have been proposed in the literature. One paper [3] proposes a structure at both the transmit and receive antenna arrays consisting of a back reflector and two side reflectors (Fig. 2.4), and analyzes capacity through FDTD simulation, as shown in Fig. 2.5. This method increases the norm and decreases the condition number of the channel matrix, thus increasing channel capacity.

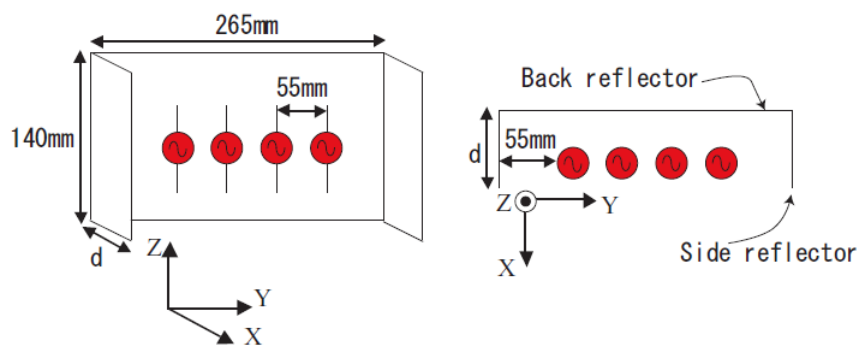


Figure 2.4: Near-Field MIMO Array Reflector [3]

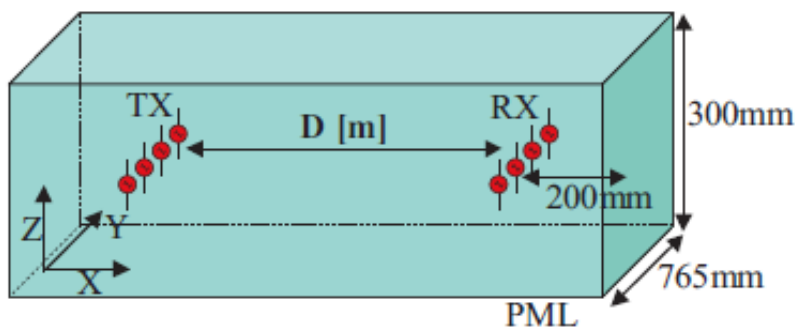


Figure 2.5: FDTD Near-Field MIMO Array Simulation [3]

Another paper (dissertation [47]) proposes the use of use of two-element dipole arrays (with separation determining the element's half power beam width(HPBW)) as a single

element in a multi-element transmit array, with this dual-dipole array forming a “beam” directed at the corresponding element of the receive array. This configuration almost creates an independent, parallel connection between each pair of antennas, similar to the concept of Short Range MIMO previously described. An optimization of element HPBW was performed to maximize capacity. No multipath was considered in analysis. Secondly, the addition of metal wires to the inter-array space to cause scattering and increase multipath richness was introduced. The effect of these wires on capacity was modeled and investigated. This dissertation suggests that element HPBW optimization in conjunction with objects placed between the transmit and receive arrays in near-field MIMO systems can increase capacity of near-field MIMO systems.

2.3 Preliminary Investigations

This section contains two preliminary investigations that served as the starting point of work in this dissertation. The first investigation serves as a simple initial assessment of MIMO capacity in the near-field using Hertzian dipoles. The second serves as an extension of textbook near-field dipole interaction equations for simple parallel orientations to arbitrary orientations. Neither investigation is novel enough to consider a contribution, but both are important enough to include as background for this document.

2.3.1 Hertzian Dipole Field-Based Channel Matrix Formulation

A MIMO channel at a single frequency can be described as a channel matrix \mathbf{H} (a complex matrix which describes the amplitude gain and phase shift from a vector of applied voltage signals at the transmit antenna array (\vec{x}) to a vector of induced voltage signals at the received

antenna array (\vec{y}) and an additive noise vector \vec{n} . This relation is as follows:

$$\vec{y} = \mathbf{H}\vec{x} + \vec{n} \quad (2.19)$$

The channel matrix can either be deterministic, a stochastic process, or a sampling of a stochastic process. Wideband models of MIMO channels involving extensions of the \mathbf{H} matrix to $\mathbf{H}(\omega)$ can be made, but are beyond the scope of this chapter.

As a first step into investigating a near-field MIMO channel model, it is useful to formulate a channel matrix \mathbf{H} which includes near-field effects. Traditional path loss models used to calculate values of the \mathbf{H} matrix, including the Friis equation and Log-distance path loss model, neglect these effects. Because the channel matrix is a relation of received voltage v_r and transmit voltage v_t , because the electric field generated by the transmit antenna (using free-space assumptions) is related to v_t , and because v_r is proportional to the electric field incident on the receive antenna, an electric field equation which includes near-field effects can be used in conjunction with antenna properties to determine the channel matrix.

For an initial investigation, a Hertzian dipole antenna was selected. The following is the electric field equation for a Hertzian dipole:

$$\vec{E}(\vec{r}) = j \frac{\eta_0 i_t dl}{4\pi} \left(\frac{k}{r} - \frac{j}{r^2} - \frac{1}{kr^3} \right) e^{-jkr} \sin \theta e^{j\omega t} \hat{\theta} + \frac{\eta_0 i_t dl}{2\pi} \left(\frac{1}{r^2} - \frac{j}{kr^3} \right) e^{-jkr} \cos \theta e^{j\omega t} \hat{r} \quad (2.20)$$

where \vec{r} is the position vector in relation to the transmit antenna, η_0 is the intrinsic impedance of free space, k is the wavenumber ($k = \frac{2\pi}{\lambda}$, where λ is wavelength in free space), r is the radial component of \vec{r} , θ is the elevation component of \vec{r} , i_t is the current applied to the transmitting antenna, and dl is the short length of the Hertzian dipole.

First, as a point of comparison, a far-field channel matrix \mathbf{H} will be determined using the Hertzian dipole equation, followed by a near-field channel matrix.

Far-Field Channel Matrix Formulation

For the far field, as r becomes large, $\frac{1}{r^2}$ and $\frac{1}{r^3}$ terms go to zero. Therefore, \vec{E} becomes:

$$\vec{E}(\vec{r}) = j \sin \theta \frac{\eta_0 i_t dlk}{4\pi r} e^{-jkr} e^{j\omega t} \hat{\theta} \quad (2.21)$$

We can assume voltage applied to the transmitting antenna is $v_t = Z_t i_t e^{j\omega t}$, where Z_t is the impedance of the antenna, i_t is the magnitude of the current through the antenna (assumed to be uniform due to the short length of a Hertzian dipole), and $e^{j\omega t}$ is the temporal component. This equation can be arranged to find current in terms of voltage and impedance:

$$i_t = \frac{v_t}{Z_t e^{j\omega t}} \quad (2.22)$$

Substituting i_t into the far-field Hertzian dipole equation:

$$\vec{E}(\vec{r}) = j \sin \theta \frac{\eta_0 v_t dlk}{4\pi r Z_t e^{j\omega t}} e^{-jkr} e^{j\omega t} \hat{\theta} \quad (2.23)$$

Simultaneously, the induced current at the output of the receive antenna i_r is proportional to $\vec{E}(\vec{r})$ with dependence on the frequency of the received signal ω and orientation of the receive antenna with respect to the incidence of $\vec{E}(\vec{r})$ (both in θ_r and ϕ_r). This constant of proportionality can be defined as $a(\theta_r, \phi_r, \omega)$, or in the case of the Hertzian dipole where orientation in azimuthal angle of incidence ϕ has no effect on the received current, $a(\theta_r, \omega)$. Therefore we can define the following relation between electric field and current at the

receiver:

$$i_r = a(\theta, \omega) \vec{E}(\vec{r}) \quad (2.24)$$

It follows that the voltage at the receiver v_r is the following:

$$v_r = Z_r i_r = Z_r a(\theta, \omega) \vec{E}(\vec{r}) \quad (2.25)$$

Combining this with the \vec{E} equation in terms of v_t :

$$v_r e^{j\omega t} = j \sin \theta \frac{Z_r a(\theta, \omega) \eta_0 v_t dlk}{4\pi r Z_t} e^{-jkr} e^{j\omega t} \hat{\theta} \quad (2.26)$$

Performing a Fourier Transform on this equation:

$$2\pi V_r \delta(\omega - \omega_0) = 2\pi j \frac{Z_r a(\theta, \omega) \eta_0 dlk}{4\pi r Z_t} e^{-jkr} \sin \theta V_t \delta(\omega - \omega_0) \quad (2.27)$$

Since $H(\omega_0) = \frac{V_r}{V_t} \delta(\omega - \omega_0)$, dividing both sides of the previous equation by $2\pi V_t$ will yield $H(\omega_0)$:

$$H(\omega_0) = j \frac{Z_r a(\theta, \omega_0) \eta_0 dlk}{4\pi r Z_t} e^{-jkr} \sin \theta \quad (2.28)$$

If we let $b(\theta, \omega_0) = j \frac{Z_r a(\theta, \omega_0) \eta_0 dlk}{4\pi Z_t} \sin \theta$, then $H(\omega)$ can be rewritten as a function of θ , ω and r :

$$H(\theta, \omega_0, r) = \frac{b(\theta, \omega_0) e^{-jkr}}{r} \quad (2.29)$$

This is the channel response between two antennas in the far-field at frequency ω_0 . This is exactly as expected; power gain is proportional to HH^* , which decreases as $\frac{1}{r^2}$, which is also the rate at which the Friis equation (used for far-field free-space gain) decreases.

Next we will apply this result to build the channel matrix \mathbf{H} . Figure 2.6 illustrates a 2×2 MIMO system with each Tx/Rx antenna pair labeled with a different $H(\theta, \omega, r)$.

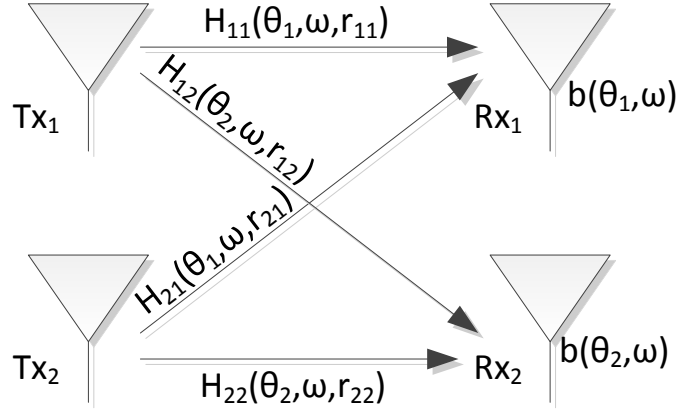


Figure 2.6: 2×2 MIMO System Model

For each transmit/receive pair of antennas ij , the distance r_{ij} is calculated, which is in turn used (along with ω and receive antenna orientation θ_j) to calculate $H_{ij}(\theta_j, \omega, r_{ij})$, which populate \mathbf{H} :

$$\mathbf{H} = \begin{bmatrix} \frac{b(\theta_1, \omega)e^{-jkr_{11}}}{r_{11}} & \frac{b(\theta_2, \omega)e^{-jkr_{12}}}{r_{12}} \\ \frac{b(\theta_1, \omega)e^{-jkr_{21}}}{r_{21}} & \frac{b(\theta_2, \omega)e^{-jkr_{22}}}{r_{22}} \end{bmatrix} \quad (2.30)$$

For the far field, $r_{11} \approx r_{12} \approx r_{21} \approx r_{22}$, which may result in a high condition number, especially if $\theta_1 = \theta_2$. A high condition number may result in minimal gain in capacity provided by MIMO over a SISO configuration.

Near-Field Channel Matrix Formulation

Our next step is to derive \mathbf{H} using the same methodology as the previous subsection but without far-field assumptions. For simplicity of analysis, we assume $\theta = \frac{\pi}{2}$, resulting in the \hat{r} component going to zero due to $\cos\theta$.

$$\vec{E}(\vec{r}) = j \frac{\eta_0 \dot{I}_t dl}{4\pi} \left(\frac{k}{r} - \frac{j}{r^2} - \frac{1}{kr^3} \right) e^{-jkr} e^{j\omega t} \hat{\theta} \quad (2.31)$$

Using Eq. 2.31 and Eq. 2.22 together, we derive the following:

$$\vec{E}(\vec{r}) = j \frac{\eta_0 v_t dl}{4\pi Z_t e^{j\omega t}} \left(\frac{k}{r} - \frac{j}{r^2} - \frac{1}{kr^3} \right) e^{-jkr} e^{j\omega t} \hat{\theta} \quad (2.32)$$

Once again, the received current in Eq. 2.24 is manipulated to obtain an expression for v_r (Eq. 2.25). Substituting Eq. 2.32 into Eq. 2.25, we have:

$$v_r e^{j\omega t} = v_t \frac{j Z_r a(\frac{\pi}{2}, \omega) \eta_0 dl}{4\pi Z_t} \left(\frac{k}{r} - \frac{j}{r^2} - \frac{1}{kr^3} \right) e^{-jkr} e^{j\omega t} \hat{\theta} \quad (2.33)$$

Performing a Fourier Transform on Eq. 2.33:

$$2\pi V_r \delta(\omega - \omega_0) = 2\pi V_t \frac{j Z_r a(\frac{\pi}{2}, \omega) \eta_0 dl}{4\pi Z_t} \left(\frac{k}{r} - \frac{j}{r^2} - \frac{1}{kr^3} \right) e^{-jkr} \delta(\omega - \omega_0) \quad (2.34)$$

Since $H(\omega_0) = \frac{V_r}{V_t} \delta(\omega - \omega_0)$, dividing both sides of the previous equation by $2\pi V_t$ will yield $H(\omega_0)$:

$$H(\omega_0) = j \frac{Z_r a(\frac{\pi}{2}, \omega_0) \eta_0 dl}{4\pi Z_t} \left(\frac{k}{r} - \frac{j}{r^2} - \frac{1}{kr^3} \right) e^{-jkr} \quad (2.35)$$

If we let $b\left(\frac{\pi}{2}, \omega\right) = j \frac{Z_r a\left(\frac{\pi}{2}, \omega\right) \eta_0 dl}{4\pi Z_t}$, then $H(\omega_0)$ can be rewritten as a function of θ , ω and r :

$$H\left(\frac{\pi}{2}, \omega_0, r\right) = b\left(\frac{\pi}{2}, \omega_0\right) \left(\frac{k}{r} - \frac{j}{r^2} - \frac{1}{kr^3}\right) e^{-jkr} \quad (2.36)$$

This is the channel response between two antennas in the near-field at frequency ω_0 and $\theta = \frac{\pi}{2}$. In the near-field, the $\frac{1}{r^2}$ and $\frac{1}{r^3}$ terms dominate.

Next we will once again apply this result to build the channel matrix \mathbf{H} . Figure 2.6 still describes the same system in the near-field. For each transmit/receive pair of antennas ij , the distance r_{ij} is calculated (being much shorter than in the far-field case), which is in turn used (along with ω_0) to calculate $H_{ij}(\theta_j, \omega_0, r_{ij})$, which populate \mathbf{H} :

$$\mathbf{H} = \begin{bmatrix} b\left(\frac{\pi}{2}, \omega_0\right) \left(\frac{k}{r_{11}} - \frac{j}{r_{11}^2} - \frac{1}{kr_{11}^3}\right) e^{-jkr_{11}} & b\left(\frac{\pi}{2}, \omega_0\right) \left(\frac{k}{r_{12}} - \frac{j}{r_{12}^2} - \frac{1}{kr_{12}^3}\right) e^{-jkr_{12}} \\ b\left(\frac{\pi}{2}, \omega_0\right) \left(\frac{k}{r_{21}} - \frac{j}{r_{21}^2} - \frac{1}{kr_{21}^3}\right) e^{-jkr_{21}} & b\left(\frac{\pi}{2}, \omega_0\right) \left(\frac{k}{r_{22}} - \frac{j}{r_{22}^2} - \frac{1}{kr_{22}^3}\right) e^{-jkr_{22}} \end{bmatrix} \quad (2.37)$$

2.3.2 AWGN Channel

For the AWGN channel, The \mathbf{H} in Eq. 2.19 is deterministic, while the additive noise vector \vec{n} has a Gaussian distribution $\tilde{n}_1(0, \sigma^2) + jn_2(0, \sigma^2)$. The value σ^2 is used to determine SNR for capacity calculations.

2.3.3 Normalization

Normalization is performed on the channel matrix \mathbf{H} by multiplying it by

$$\left(\frac{1}{N_t N_r} \|\mathbf{H}\|_F^2\right)^{\left(-\frac{1}{2}\right)} \quad (2.38)$$

or equivalently, by multiplying by the square root of the product of the number of receive and transmit antennas and dividing by the value of the Frobenius norm of \mathbf{H} [48]. Normalizing a matrix by its Frobenius norm forces the sum of its eigenvalues (i.e. the sum of the square of its singular values) to equal 1, and therefore allows us to investigate distribution of eigenvalues among the independent parallel channels in the system.

This also allows us to explicitly set the SNR (the ratio of received signal power to noise power at the receiver) in the capacity equation (defined in the next section), rather than having to calculate the received power by multiplying some defined transmit power by the squared unnormalized channel matrix. Also, by multiplying by the square root of the product of number of transmit and receive antennas, we preserve the capacity gains provided by having multiple independent streams in MIMO, allowing for comparison with other similarly normalized MIMO or SISO systems.

2.3.4 Capacity Equations

As discussed in the background chapter, the capacity of a single communications channel is known to be $\log_2(1 + SNR)$ (assuming normalized bandwidth). In MIMO communications, the channel matrix \mathbf{H} can be decomposed to form $R_{\mathbf{H}}$ (rank of \mathbf{H}) independent channels, each with its own applied power at the transmitter. The applied power is some fraction of the total transmit power, P_t , and the sum of the powers of each independent channel is equal to P_t . Each independent channel has a power gain proportional to an eigenvalue of the channel matrix, λ_n^2 , where n is the index of the independent channel. Therefore, the received power for independent channel n is equal to $k_n P_t \lambda_n^2$, where k_n is the fraction of the power P_t applied to independent channel n . The SNR of this single, independent channel is therefore $\frac{k_n P_t \lambda_n^2}{N_0}$ where N_0 is the noise power of the independent channel. If we

define the overall SNR of the receiver to be $\frac{P_t}{N_0}$, then the independent channel SNR is equal to $SNR \cdot k_n \lambda^2$. In short, k_n is the normalized power allocation of the transmitter, and the generalized MIMO capacity equation becomes the sum of the capacity of the independent channels:

$$C = \sum_{n=1}^{R_{\mathbf{H}}} \log_2 \left(1 + SNR \cdot k_n \vec{\lambda}_n^2 \right) \quad (2.39)$$

The optimal distribution of power \vec{k} between the independent channels depends on the transmitter channel knowledge. If the MIMO system has no feedback mechanism or time-division duplexing with which to estimate \mathbf{H} , then the optimal power allocation is uniform distribution of power among the independent channels, i.e. $k_n = \frac{1}{N_t}$ for all n , where N_t is the number of transmit antennas. Therefore, the capacity of a MIMO channel where the channel matrix is unknown at the transmitter is:

$$C = \sum_{n=1}^{R_{\mathbf{H}}} \log_2 \left(1 + \frac{SNR}{N_t} \vec{\lambda}_n^2 \right) \quad (2.40)$$

If the transmitter has a method of accurately determining the channel matrix, it can perform eigenvalue decomposition (or singular value decomposition, where eigenvalues are equal to the square of the singular values) to determine the channel eigenvalues. With this information, the transmitter can perform the waterfilling algorithm (outlined in the background chapter) to determine the optimal power distribution P_n^* for each of the $R_{\mathbf{H}}$ independent channels. Normalizing the vector of transmit powers \vec{P}^* by $\|\vec{P}^*\|$ yields $k_n = \frac{P_n^*}{\|\vec{P}^*\|}$, and therefore the corresponding MIMO capacity for waterfilling is:

$$C = \sum_{n=1}^{R_{\mathbf{H}}} \log_2 \left(1 + \frac{SNR \cdot P_n^*}{\|\vec{P}^*\|} \vec{\lambda}_n^2 \right) \quad (2.41)$$

2.3.5 Channel and Capacity Simulation

In order to investigate the performance of this electric field-based line-of-sight AWGN channel model which includes near-field components, a simulation was constructed in MATLAB. This simulation uses Eq. 2.37 to generate a channel matrix \mathbf{H} used in capacity calculation.

This simulation sweeps over SNR (0 to 15 dB) and array separation (from 0.2 to 20 λ). First, it calculates the distance between each pair of transmit and receive antennas r_{ij} using the antenna separation and array separation value. It is assumed that $\theta = \frac{\pi}{2}$, and that all Hertzian dipoles in both receive and transmit arrays are co-planar and parallel. Next, using the channel matrix equations (Eq. 2.37) from the previous section (note: the near-field effects in this equation are negligible for far-field separation distances, and thus this equation can be used for both near- and far-field scenarios. As a result, this equation is used in this simulation for all array separation distances.), the channel matrix \mathbf{H} is calculated.

The purpose of this simulation is to compare the effects of near versus far field on the capacity of line-of-sight MIMO, not the effect of increased path loss due to increased array separation on the capacity, and therefore the channel matrix \mathbf{H} must be normalized as described in the previous section to isolate the effect of near-field components in the model.

Next, singular value decomposition (SVD) is performed on the normalized channel matrix \mathbf{H}_{norm} to determine singular value array $\vec{\lambda}$. The rank of \mathbf{H} ($R_{\mathbf{H}}$) corresponds to the number of non-zero elements in $\vec{\lambda}$. (It should be noted that the square of each singular value is equal to an eigenvalue of \mathbf{H}_{norm}). If the channel is unknown at the transmitter, uniform power distribution is used and MIMO capacity is computed as in equation Eq. 2.40. If the channel is known at the transmitter through some mechanism, it can calculate channel eigenvalues and

use waterfilling to allocate power to the independent channels as P^* , resulting in capacity defined by Eq. 2.41.

Our simulation showed that for uniform power allocation, the capacity plot converged towards a plane as the array separation distance increased, as illustrated in Fig. 2.7. This is to be expected, as in the far-field, the $\frac{1}{r}$ term dominates in both the electric field and channel equations, the distances between transmit and receive antenna pairs become proportionally similar, and the distribution of the eigenvalues becomes such that one value approaches zero and the rank of the matrix essentially trends to one, indicating a single spatial channel. With the decomposition of the channel matrix trending towards a single channel, and with the normalization of the channel matrix removing the effects of path loss associated with separation distance, the capacity plot trends asymptotically towards a constant when varying array separation (a constant which is equal to $\log_2\left(1 + \frac{SNR}{N_t}\right)$). In short, the benefits of MIMO disappear for a line of sight AWGN channel in the far-field, with the capacity trending towards a SISO value.

In the near-field, however, (in the range at and below $\lambda = 1$), we see that a slight increase in capacity is observed as the array separation distance decreases, particularly at high SNR values. This can be attributed to the fact that at lower array separation distances, the distances between transmit and receive antenna pairs become proportionally less similar, indicating the signal received at each receive antenna has a dominant component from one transmit antenna and a less dominant component from another. Therefore in the absence of reflections and a scattering environment, MIMO systems perform better in the near-field than in the far field.

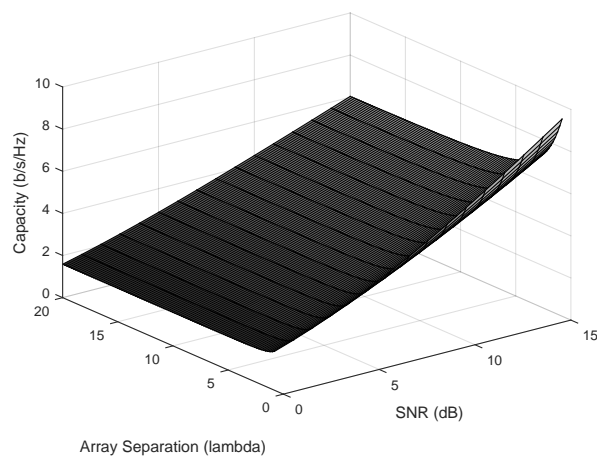


Figure 2.7: Capacity with Uniform Allocation vs. SNR and Spacing

2.3.6 Background for Selection of Free-Space Green's Function as Basis

The following is adapted from Orfanidis textbook on Electromagnetic Waves and Antennas [19], but is adapted for arbitrary-oriented dipoles instead of z-oriented dipoles, non-

parallel dipoles, or coplanar dipoles. It is also adapted to use a 3-term King current distribution approximation instead of the sinusoidal assumption due to the fact that some antennas in a log periodic array will be significantly longer than a half-wavelength. The goal is to find the mutual- and self-impedance at each element in the system in free-space, which can then be used in a system of equations to find the voltage at the receiving dipole or dipoles presented over a load for a unit input. This is the free-space channel from probe input to receiver output, including near-field effects and coupling. This channel includes all antenna effects. Because the far-field approximation does not hold, the concept of antenna gain patterns and angle of arrival have limited meaning, as electric fields from one element to another do not follow a typical distribution across the antenna as if the incident field was a plane wave with definite direction of arrival. While reflected wave components may exhibit a plane wave-like behavior at the receiver due to the increased travel distance of the wave between transmitter and receiver, the dominant line of sight field and some reflections may not. In free space, the only field of interest will be the line of sight case, meaning the line of sight case can be analyzed for choice of channel approximation basis in the non-far field, as well as the conditions in which this approximation basis holds.

The free-space system that approximates the line of sight conditions of the channel of interest to be modeled is the first task in the choice approximation basis function. The channel of interest to be modeled consists of probe antenna log-periodic arrays each with fourteen-elements, oriented perpendicular to the X-Y plane and aimed at a point in the center of the X-Y plane, and receiver dipoles oriented in the Z direction, with centers located along a plane parallel to the X-Y plane. As a first approximation, a single log-periodic antenna and a single dipole will be analyzed.

To model the channel from a log-periodic antenna to a dipole antenna, a relation between

the input of the log periodic antenna and output of the dipole must be established. To accomplish this, the current distribution on each antenna element and the electric fields of each antenna must be established.

Each element in a log-periodic antenna is itself a dipole antenna. The length and spacing of each element in the array is related to the length and spacing of the previous element by a factor τ . The starting and ending dipole lengths are chosen such that half of the shortest and longest wavelengths of interest are between the lengths of the shortest and longest elements. This ensures that for any input frequency in the range of interest will be relatively close in half-wavelength to the length of one of the array antenna elements. The number of elements and the initial spacing parameter are determined according to the desired antenna gain, directivity, and other parameters desired.

In finding the E-field for a dipole as in figure 2.8, the following variables must be defined. The orientation of the dipole is in the \hat{r}_m direction. Each half of the dipole has length h_m . The center of the dipole is located at the vector position \vec{r}_{m_0} . The top of the antenna therefore is at position $\vec{r}_{m_0} + h_m\hat{r}_m$, and the bottom is at position $\vec{r}_{m_0} - h_m\hat{r}_m$.

The observation point at which the E-field is observed is vector position \vec{w} . Distance R is the distance from an arbitrary point on antenna m defined by $\vec{r}_{m_0} + \alpha_m\hat{r}_m$ (where α_m is a scalar value between $-h_m$ and h_m) to the observation point \vec{w} , $|\vec{w} - \vec{r}_{m_0} - \alpha_m\hat{r}_m|$. Distance R_0 is the distance from the antenna center to the observation point $|\vec{w} - \vec{r}_{m_0}|$. Distance R_1 is the distance from the antenna top to the observation point, $|\vec{w} - \vec{r}_{m_0} - h_m\hat{r}_m|$. Distance R_2 is the distance from the antenna bottom to the observation point, $|\vec{w} - \vec{r}_{m_0} + h_m\hat{r}_m|$.

The radial vector from the antenna $\hat{\rho}_m$ is in the direction of the observation point and perpendicular to \hat{r}_m , the orientation of the antenna. The observation location vector \vec{w} can therefore be expressed as:

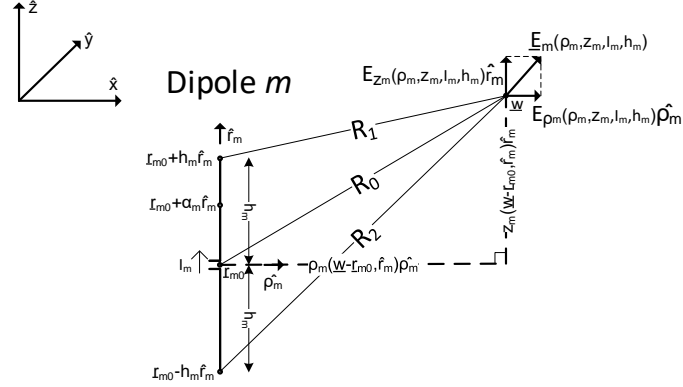


Figure 2.8: Dipole Electric Field Formulation

$$\vec{w} = \vec{r}_{m_0} + z_m \hat{r}_m + \rho_m \hat{\rho}_m \quad (2.42)$$

where \vec{r}_{m_0} is the center of the dipole, $z_m \hat{r}_m$ is an antenna directional component, and $\rho_m \hat{\rho}_m$ is a radial component. The component z_m can be calculated with vector projection as:

$$z_m = \frac{(\vec{w} - \vec{r}_{m_0}) \cdot \hat{r}_m}{\hat{r}_m \cdot \hat{r}_m} \hat{r}_m \quad (2.43)$$

while ρ_m can be calculated with vector rejection as:

$$\rho_m = \vec{w} - \vec{r}_{m_0} - \frac{(\vec{w} - \vec{r}_{m_0}) \cdot \hat{r}_m}{\hat{r}_m \cdot \hat{r}_m} \hat{r}_m \quad (2.44)$$

With this component definition of \vec{w} , the distances R , R_0 , R_1 , and R_2 can be redefined as:

$$R = \sqrt{(z_m - \alpha_m)^2 + \rho_m^2} \quad (2.45)$$

$$R_0 = \sqrt{z_m^2 + \rho_m^2} \quad (2.46)$$

$$R_1 = \sqrt{(z_m - h_m)^2 + \rho_m^2} \quad (2.47)$$

$$R_2 = \sqrt{(z_m + h_m)^2 + \rho_m^2} \quad (2.48)$$

These component definitions of distances allow for a straightforward evaluation of magnetic vector potential, and subsequently electric field expressions.

As adapted from [19] to match the arbitrary vector dipole notation in this analysis, the \hat{r}_m -component of the magnetic vector potential $A_{\hat{r}_m}$ is:

$$A_{\hat{r}_m}(z_m, \rho_m) = \frac{\mu}{4\pi} \int_{-h_m}^{h_m} I(\alpha'_m) \frac{e^{-jkR}}{R} d\alpha'_m \quad (2.49)$$

with z_m , ρ_m , h_m , α_m , and R as previously defined, k is the wavenumber at the frequency of analysis, and μ is the permeability of free space. Using Maxwell's equations, this can be utilized to find the \hat{r}_m and $\hat{\rho}_m$ components of the electric field. The relevant forms of the equations used are:

$$j\omega\mu\epsilon E_{\hat{r}_m} = \partial_{\hat{r}_m}^2 A_{\hat{r}_m} + k^2 A_{\hat{r}_m} \quad (2.50)$$

$$j\omega\mu\epsilon E_{\hat{\rho}_m} = \partial_{\hat{\rho}_m} \partial_{\hat{r}_m} A_{\hat{r}_m} \quad (2.51)$$

$$\mu H_\phi = -\partial_{\hat{\rho}_m} A_{\hat{r}_m} \quad (2.52)$$

$$\partial_{\hat{\rho}_m} (\rho_m H_{\hat{\phi}_m}) = j\omega\epsilon\rho_m E_{\hat{r}_m} \quad (2.53)$$

$$j\omega\epsilon E_{\hat{\rho}_m} = -\partial_{\hat{r}_m} H_{\hat{\phi}_m} \quad (2.54)$$

Using these relations and the definition of $A_{\hat{r}_m}$, in conjunction with the fact that the \hat{r}_m component of the electric field must vanish along the antenna's surface, along with assumptions the current distribution $I_m(\alpha_m)$ is symmetric in α_m and is zero at the ends of the antenna, we can define the components of the electric field at the observation point as a function of current distribution along the antenna, and the position of the observation point in relation to the position and orientation of the antenna.

$$j\omega\mu\epsilon E_{\hat{r}_m}(z_m, \rho_m) = \frac{\mu}{4\pi} \int_{-h_m}^{h_m} I(\alpha'_m) (\partial_{\hat{r}_m}^2 + k^2) \frac{e^{-jkR}}{R} d\alpha'_m \quad (2.55)$$

$$-4\pi j\omega\epsilon\rho_m E_{\hat{\rho}_m}(z_m, \rho_m) = \int_{-h_m}^{h_m} I(\alpha'_m) (\partial_{\hat{r}_m}^2 + k^2) \left((z_m - \alpha'_m) \frac{e^{-jkR}}{R} \right) d\alpha'_m \quad (2.56)$$

Using a differential identity, defined end-point conditions, and a redefinition of the integral into parts, the following equations which express the \hat{r}_m and $\hat{\rho}_m$ electric field components at the observation point \vec{w} are formed:

$$\begin{aligned}
 E_{\hat{r}_m}(z_m, \rho_m) = & \frac{1}{4\pi j\omega\epsilon} \left[\int_{-h_m}^{0-} \frac{e^{-jkR}}{R} \left(I''(\alpha'_m) + k^2 I(\alpha'_m) \right) d\alpha'_m \right. \\
 & + \int_{0+}^{h_m} \frac{e^{-jkR}}{R} \left(I''(\alpha'_m) + k^2 I(\alpha'_m) \right) d\alpha'_m \\
 & \left. + 2I'(0+) \frac{e^{-jkR_0}}{R_0} - I'(h) \left(\frac{e^{-jkR_1}}{R_1} + \frac{e^{-jR_2}}{R_2} \right) \right]
 \end{aligned} \tag{2.57}$$

$$\begin{aligned}
 E_{\hat{\rho}_m}(z_m, \rho_m) = & \frac{1}{-4\pi j\omega\epsilon\rho_m} \left[\int_{-h_m}^{0-} (z_m - \alpha'_m) \frac{e^{-jkR}}{R} \left(I''(\alpha'_m) + k^2 I(\alpha'_m) \right) d\alpha'_m \right. \\
 & + \int_{0+}^{h_m} (z_m - \alpha'_m) \frac{e^{-jkR}}{R} \left(I''(\alpha'_m) + k^2 I(\alpha'_m) \right) d\alpha'_m \\
 & \left. + 2I'(0+)z_m \frac{e^{-jkR_0}}{R_0} - I'(h) \left((z_m - h_m) \frac{e^{-jkR_1}}{R_1} + (z_m + h_m) \frac{e^{-jR_2}}{R_2} \right) \right]
 \end{aligned} \tag{2.58}$$

The final step for obtaining the accurate electric field from a dipole is to establish an accurate approximation of the current along the dipole. A procedure from [19] is utilized to numerically compute the current distribution of the antenna utilizing Hallen equation solutions "with point-matching, pulse basis functions, and exact kernel with M=100 upper-half current samples". The numerical solution is then fit to a 3-term approximation defined as:

$$I(\alpha_m) = A_1 [\sin(k|\alpha_m|) - \sin(kh_m)] + A_2 [\cos(k\alpha_m) - \cos(kh_m)] + A_3 \left[\cos\left(\frac{k\alpha_m}{2}\right) - \cos\left(\frac{kh_m}{2}\right) \right] \tag{2.59}$$

with derivatives used in the electric field equations defined as:

$$I''(\alpha'_m) + k^2 I(\alpha'_m) = -k^2 A_1 \sin(kh_m) - k^2 A_2 \cos(kh_m) - k^2 A_3 \left[\cos\left(\frac{kh_m}{2}\right) - \frac{3}{4} \cos\left(\frac{k\alpha'_m}{2}\right) \right] \quad (2.60)$$

$$I'(0+) = -I'(0-) = kA_1 \quad (2.61)$$

$$I'(h_m) = -I'(-h_m) = kA_1 \cos(kh_m) - kA_2 \sin(kh_m) - \frac{1}{2} kA_3 \sin\left(\frac{kh_m}{2}\right) \quad (2.62)$$

With the component definition of the electric field in conjunction with a current approximation, the complete electric field from one antenna can be defined completely along a second antenna, allowing for calculation of mutual impedance, and thereby allowing one to find the voltage or current induced at each antenna from the excitation of one or more of the antennas in the system.

Let a system of two antennas be defined as antennas m and n , with arbitrary vector orientations \hat{r}_m and \hat{r}_n respectively. Figure 2.9 defines the the variables in this system. The two antennas have centers at \vec{r}_{m_0} and \vec{r}_{n_0} respectively, and half-lengths h_m and h_n respectively. The observation point is now defined as a position on antenna n , $\vec{r}_{n_0} + \alpha_n \hat{r}_n$ rather than an arbitrary point in space \vec{w} . Using this definition, the variables z_m and ρ_m must be redefined.

$$\vec{r}_{n_0} + \alpha_n \hat{r}_n = \vec{r}_{m_0} + z_m \hat{r}_m + \rho_m \hat{\rho}_m \quad (2.63)$$

once again, where \vec{r}_{m_0} is the center of the dipole, $z_m \hat{r}_m$ is an antenna directional component, and $\rho_m \hat{\rho}_m$ is a radial component. z_m can be calculated with vector projection as:

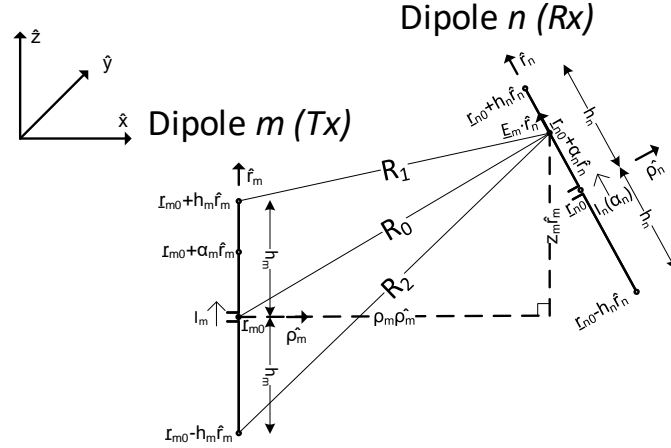


Figure 2.9: Dipole Mutual Impedance Formulation

$$z_m(\alpha_n) = \frac{(\vec{r}_{n0} + \alpha_n \hat{r}_n - \vec{r}_{m0}) \cdot \hat{r}_m}{\hat{r}_m \cdot \hat{r}_m} \hat{r}_m \quad (2.64)$$

while ρ_m can be calculated with vector rejection as:

$$\rho_m(\alpha_n) = \vec{r}_{n0} + \alpha_n \hat{r}_n - \vec{r}_{m0} - \frac{(\vec{r}_{n0} + \alpha_n \hat{r}_n - \vec{r}_{m0}) \cdot \hat{r}_m}{\hat{r}_m \cdot \hat{r}_m} \hat{r}_m \quad (2.65)$$

these definitions are important as they will allow a projection of the electric field onto the orientation vector of the receiving antenna, thus finding the electric field component perpendicular to the receive antenna as a function of position on the receive antenna. This electric field along the receive antenna, as well as the approximated current along the receive antenna, can be utilized to find the mutual impedance of the second antenna on the first antenna. First, the induced open-circuit voltage on the antenna n due to antenna m is:

$$V_{nm,oc} = -\frac{1}{I_n} \int_{-h_n}^{h_n} (\vec{E}_{nm}(\alpha_n) \cdot \hat{r}_n) I_n(\alpha_n) d\alpha_n \quad (2.66)$$

where α_n is a scalar from $-h_n$ to h_n that defines position on antenna n , I_n is the current at the center of antenna n ($\alpha_n = 0$), $I_n(\alpha_n)$ is the current at position α_n on antenna n , and $E_{nm}(\alpha_n)$ is the electric field at the point $\vec{r}_{n0} + \alpha_n \hat{r}_n$ on antenna n due to antenna m . Using equations 2.57 and 2.58, $E_{mn}(\alpha_n)$ is defined as:

$$\vec{E}_{nm}(\alpha_n) = E_{\hat{r}_m}(z_m(\alpha_n), \rho_m(\alpha_n)) \hat{r}_m + E_{\hat{\rho}_m}(z_m(\alpha_n), \rho_m(\alpha_n)) \hat{\rho}_m \quad (2.67)$$

The dot product of this field with the orientation vector \hat{r}_n is therefore the electrical field component along antenna n . The current $I_n(\alpha_n)$, also used in the open-circuit equation, is found using the 3-term fit Hallen current approximation for antenna (n with coefficients A_1 , A_2 and A_3 recalculated for antenna n). With the new approximation coefficients, $I_n(\alpha_n)$ can be defined using 2.59. Finally, using $I_m = I_m(0)$ and $I_n = I_n(0)$, and the open-circuit voltage equation 2.66, the mutual impedance is defined as:

$$Z_{nm} = \frac{V_{nm,oc}}{I_m} = -\frac{1}{I_m I_n} \int_{-h_n}^{h_n} (\vec{E}_{nm}(\alpha_n) \cdot \hat{r}_n) I_n(\alpha_n) d\alpha_n \quad (2.68)$$

In addition to mutual impedance between each and every combination of elements in the system (both within the log-periodic antenna and between the elements of the log periodic antenna and the receiving dipole antenna), the self impedance of each element must be calculated. (NOTE: this is the part that is resulting in a "bad" half-wave dipole approximation and should be scrutinized the most.) Figure 2.10 shows a horizontally-magnified dipole antenna m , with radius a_m . All other variables remain the same as for the previously presented

electric field analysis of dipole m . According to [19], the self-impedance can be calculated with the same formula, treating the surface of the antenna, $\vec{r}_{m0} + \alpha_m \hat{r}_m + a_m \hat{\rho}_m$, as the "second antenna" along which the electric field is calculated for the impedance equation 2.68. Because the two aspects of the same antenna are oriented identically in the \hat{r}_m direction, only the \hat{r}_m component of the E field will be present in the impedance calculation.

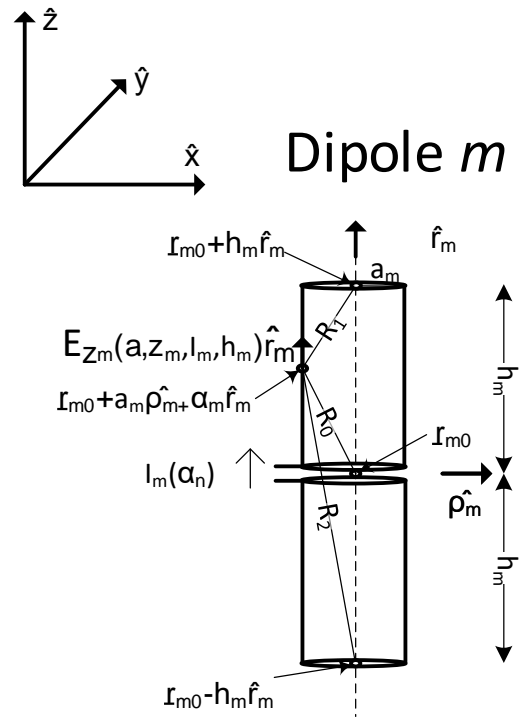


Figure 2.10: Dipole Self Impedance Formulation

It should be noted that this approach is presented in [19] in the context of a sinusoidal current approximation, which only applies to antennas around a half-wavelength in length. Because elements of the log periodic antenna may be considerably longer than a

half-wavelength at the frequency of analysis, this approximation cannot be used. However, the current approximation method used in prior sections utilizes assumptions such as the \hat{r}_m component of the electric field being equal to zero on the antenna surface, which is reflected in the developed electrical field equations.

CHAPTER 3

Small Anechoic Chamber Feasibility for MIMO-OTA Testing

The first contribution of this work is a cost-effective small anechoic chamber for MIMO-OTA testing demonstrating the effect of size constraints on the performance of an anechoic chamber for testing MIMO-OTA signals in a single-cluster environment with Laplacian Power Azimuthal Spectrum. Typical large anechoic chambers used in MIMO-OTA testing can often cost in excess of one million USD. A small chamber could be constructed for \$200 thousand USD, a significantly more cost-effective solution. Previous work on this problem focuses on minimizing the number of probes necessary to reproduce such an environment, and does not focus on constraining these probes to a small chamber. This previous work, therefore, does not investigate parameters such as chamber dimensions, antenna arrangement, or frequency. The motivation for this work is to present a system for inexpensive pre-certification of next generation devices that can help meet the demands and calls for greater broadband wireless access.

The following section includes details on the theory behind the plane wave and Laplacian PAS Electric field synthesis. Section 3.2 includes the system design and design of the chamber used in analysis. Section 3.3 includes the results of the Laplacian PAS channel simulations performed in MATLAB, and Sec. 3.4 covers the electromagnetic simulation results. The conclusions and future work are described in Sec. 3.5.

3.1 Electromagnetic Field Synthesis

In this section, we review previous work to understand the ability of a limited number of antennas to synthesize a desired electric field in a test zone. In the first subsection, spherical wave expansion theory is reviewed to investigate the number of probe antennas required to synthesize a field in a test zone of finite size. In the subsequent subsection, the ability of an array of antennas to synthesize a Laplacian PAS, and therefore model a single cluster, is discussed.

3.1.1 Number of probe antennas

A study of spherical wave expansion of a plane wave was performed as an initial investigation into the number of probe antennas required to generate a target E-field in a test zone to within a desired degree of accuracy. An arbitrary electromagnetic field can be “expanded into spherical waves in source-free regions of space limited by spherical surfaces centered at the origin of a spherical coordinate system” [18]. This electric field expansion is expressed as:

$$\vec{E}(r, \theta, \phi) = \frac{k}{\sqrt{\eta}} \sum_{csmn} Q_{smn}^{(c)} \vec{F}_{smn}^{(c)}(r, \theta, \phi) \quad (3.1)$$

where $\vec{F}_{smn}^{(c)}$ is the spherical wave function, with c indicating the radial dependency, s indicating the spherical wave function type, m indicating the order of the wave function, and n indicating the degree of the wave function. $Q_{smn}^{(c)}$ is the spherical wave coefficient, η is the admittance of the medium, k is the wave number, and (r, θ, ϕ) indicates the spherical coordinate of a point.

In the special case of expansion of a plane wave, many of these spherical wave coefficients

are approximately equal to zero, leaving coefficients for the two fundamental spherical wave functions with order -1 and 1, and degree 1 to N , or $4N$ coefficients total. Choice of N is arbitrary, and should be equal to infinity to contain all degrees (modes) of the expansion. However, a highly accurate approximation can be achieved if N is chosen to be r_0k , where k is the wavenumber of the plane wave, and r_0 is the radius of the desired spherical surface boundary. Modes above this value of N are comparatively negligible [18].

In [49], the spherical wave expansion is extended to a cylindrical case, and a 2-D cross section of the cylindrical solid is analyzed in terms of a spherical wave expansion. Additionally, [25] relates the number of modes in the spherical wave expansion to the number of (far-field) antennas required to accurately synthesize this field. In the case of the E-field perpendicular to the 2-D test zone as described in the paper, to achieve a test zone of radius r , a minimum number of probes K are required, where K is defined in Eq. (3.2) as

$$K = 4\pi r/\lambda + 1 \tag{3.2}$$

where λ is the wavelength of the plane wave. This equation was derived under the assumption that uniform circular spacing of antennas around the test zone in the far-field (full-ring test setup) was utilized, and that plane waves may arrive from any angle. If the direction of plane wave arrival (or other field arrival) is limited to a specific direction or range of directions, this number may be reduced. It is this reduction that will make a small chamber test setup possible.

3.1.2 3GPP SCME Channel Model

Our goal is to understand the trade-offs of minimizing the chamber size (including minimizing the number of probes and separation distance between probes) and the ability to

accurately synthesize a desired field. To investigate this goal, we need to further discuss the desired field to be synthesized.

The 3GPP MIMO-OTA Subgroup (MOSG) [20] is standardizing a channel model based upon the 3GPP Spatial Channel Model Extended (SCME) [50]. The SCME models a multipath fading channel with power-delay parameters with azimuthal-angular dependence. This angular dependence results from spread of power that is created from an environment based around a given cluster. The cluster of the power has been shown to have a Laplacian [25] distribution, which is defined in unnormalized form by Eq. (3.3)

$$P(\phi) = \begin{cases} e^{-|\sqrt{2}\phi/\sigma|} & \phi \in [-\pi, \pi) \\ 0 & \text{otherwise} \end{cases} \quad (3.3)$$

where ϕ is the azimuthal angle, and σ is the standard deviation of the Laplacian distribution. This equation assumes a cluster arrival from 0 degrees; the equation can be shifted in ϕ for a cluster arrival from another angle.

Laitinen et al. [25] generate a target 2-D Laplacian PAS in a test zone by sampling the unnormalized truncated Laplacian PAS function from 360 azimuthal directions with 1 degree spacing. This set of sampled amplitudes is applied to 360 plane waves arriving from each corresponding azimuthal direction. Each plane wave is given a random phase sampled from a uniform distribution. The sum of the 360 plane waves forms the target E-field in the test zone. The target E-field is uniformly sampled around the perimeter of the test zone, r_0 . The unweighted E-field, $E_k(r_0, \phi)$ contribution of each probe antenna in the probe array is determined at the same set of sample points, and an E-field 2-norm matching is performed to determine the complex coefficients of each probe antenna, c_k . After 2-norm matching, the synthesized E-field is approximately equal to the target E-field as in Eq. (3.4).

$$e(r_0) = 20 \log_{10} \left(\max_{0^\circ \leq \phi < 360^\circ} \left(\frac{|\vec{E}_{Synth}(r_0, \phi) - \vec{E}_{Target}(r_0, \phi)|}{\max_{0 < r \leq r_0, 0^\circ \leq \phi < 360^\circ} |\vec{E}_{Target}(r, \phi)|} \right) \right) \quad (3.5)$$

$$\vec{E}_{Target}(r_0, \phi) \approx \vec{E}_{Synth}(r_0, \phi) = \sum_{k=1}^N c_k \vec{E}_k(r_0, \phi) \quad (3.4)$$

The reflectivity (error) of the synthesized field from the target field is calculated across the test zone as a function of radius as in Eq. (3.5). This figure of merit will be used to analyze the performance of small chambers.

In previous work, the size of the test zone and angular spread were varied to determine the minimum number of OTA probes in various spacings needed to achieve at most -15 dB of reflectivity in the test zone in each case [25]. Additionally, this previous work assumed a large chamber without non-ideal effects due to reflections. Our contribution is an investigation of chamber design with the goal of minimizing the chamber dimensions while considering practical probe antenna locations and effects of reflections on field generation.

3.2 Small chamber system

The small anechoic MIMO-OTA test chamber is designed to create a synthetic wireless environment for one cluster. This cluster models the multi-path behavior as a tapped-delay line with a Laplacian PAS. The parameters of the multi-path channel are controlled by the RMS delay spread and the angular spread of the distribution of power, which are incorporated in the channel emulator. The channel emulator is driven by the 4×4 MIMO signaling and has N outputs corresponding to the N probe antennas with vertical (or horizontal) polarization. The method for creating the random channel is described in the section 3.1, which provides

a set of weights that are used to control the probes and generate a desired field in the test zone.

The ability to generate any arbitrary field in the test zone is related to the number of probes and their configuration. As such, this section describes the parameters of the chamber for evaluation of different test sizes. We assume the 2-D case where the elevation angle is $\theta = 90^\circ$. Figure 3.1 shows the basic arrangement of the chamber, with the width W of the chamber determined by the vertical span of the N antennas in the diagram, and the height of the chamber determined by the distance between the test zone and the probe antenna array A , and the test zone radius r_0 . The device under test (DUT) is centered in the test zone radius and will be rotated in 3-D to evaluate the performance as a function of DUT orientation to the test field.

The goal of this work is to determine the feasibility of testing a wide range of devices, from laptops to mobile phones, in a small anechoic chamber. Our simulations evaluate a wide range of values to test the corner cases of the system. In Table 3.1, we list the values for the physical and test parameters that are used in the simulations. Our simulations include two different methods that allow for simulating a wide range of chamber parameters including dimensions, frequency of operation, and Laplacian PAS spread. Also, one of these methods (HFSS) provides a method for considering practical chamber effects such as reflections from the chamber walls. The details of each type of simulation is described in the following sections.

3.2.1 Numerical Model

A simulation of the system in a vacuum (without a surrounding chamber) was performed in Mathworks Matrix Laboratory (MATLAB) sweeping over the set of system parameters

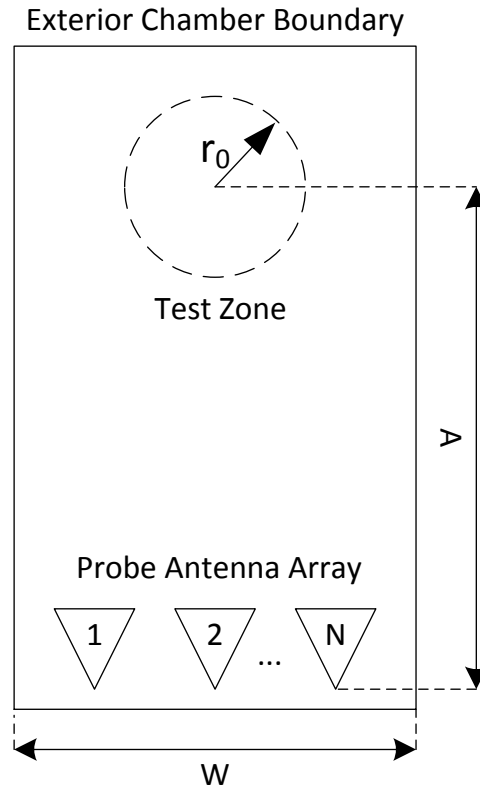


Figure 3.1: Small Anechoic Chamber Dimensions

listed Table 3.1. In the simulation a target Laplacian PAS was generated as in [25]. 2-norm matching was performed to determine the complex coefficients of each probe antenna, and the synthesized field from the probe antennas with applied weights was generated as in Eq. (3.4). The reflectivity of the synthesized field at the test zone perimeter was then determined (Eq.(3.5)). This simulation utilized a horn antenna radiation pattern with each antenna pointed at the center of the test zone, which allows for antenna configurations to be more like those found in an actual small anechoic chamber. Due to the random nature of the target E-field (caused by the random phase of each plane wave), a Monte Carlo analysis was performed to ensure a certain level of performance with a given system configuration. The statistical distribution of reflectivity was calculated for each system configuration from

Table 3.1: Simulation Parameters

Parameter	Value
Laplacian PAS spread (σ - degrees)	25, 35, 45
Frequency (f - GHz)	0.7, 2.4, 5.9
Test zone radius (r_0 - m)	0.10, 0.15, 0.20
Width (W - m)	0.95, 1.00, 2.00
Probe Antennas (N)	3 ... 6

the analysis.

In addition to the simulation scenarios described above, an additional set of simulations was performed for comparison to the simulations performed in the following subsection. The electromagnetic simulation program used in the following subsection did not have preset horn antenna sources, but did have an ideal Hertzian dipole source that could be utilized. Also, the complexity and long simulation time of this program limited the number of system configurations that could be simulated. As a result, a subset of simulations was run in MATLAB for comparison with the electromagnetic simulations using a Hertzian dipole antenna instead of a horn antenna.

The simulations include Laplacian standard deviation (σ) of 25, 35 and 45 degrees, test zone radius r_0 of 0.1 m, and two chamber configurations. Chamber configuration 1 consisted of 6 antennas, 700 MHz and antenna array width of 2.0 m. Configuration 2 consisted of 3 antennas, 2 GHz, and antenna array width of 0.95 m. Antennas were polarized in the positive X direction (perpendicular to the test zone, i.e. vertical polarization). Antenna polarization in the Y direction (parallel to the test zone, i.e. horizontal polarization) was also considered separately.

3.2.2 Computational Electromagnetic Model

The entire anechoic chamber system was also modeled in Ansys's High Frequency Structure Simulator (HFSS), a finite element method (FEM)-based electromagnetic simulation program. This allows for validation of the MATLAB simulations in a 3-D system. Two models were developed in HFSS; one with the antennas and test zone placed in a vacuum to compare results directly to those generated in MATLAB, and one with a small anechoic chamber with non-ideal absorbing materials encasing both the antennas and the test zone. The chamber model shown in Fig. 3.2 consists of an outer layer of stainless steel, and an inner absorbing material modeled after the Cuming LF-77 absorber. The Cuming LF-77 was modeled as three layers, each of thickness 0.75 inches, and each with complex permittivity and permeability values provided by the manufacturer at frequencies of 2 GHz and 3 GHz. Values of complex permittivity and permeability at 700 MHz were determined by extrapolation. The space both inside and outside the chamber was modeled as a vacuum.

As mentioned previously, the antennas used for the HFSS simulations performed in this paper are Hertzian dipoles, polarized first in the X direction (vertical), and then in the Y direction (horizontal) in a second simulation set. The interior width of the chamber is the width of the antenna array plus a space of 0.25 times the antenna spacing added to each side of the chamber. Antennas are placed 0.1 meters from the bottom of the chamber. The radius from the center of the test zone to the line of antennas is 1 meter. The center of the test zone is placed 0.3 meters from the top of the chamber. The depth of the chamber (front to back) was 1 meter, and the plane containing the probe antenna array and test zone is located 0.5 meters from both the front and back of the chamber. The test zone over which the field is matched is a circle with a radius of either 0.1, 0.15 or 0.2 meters depending

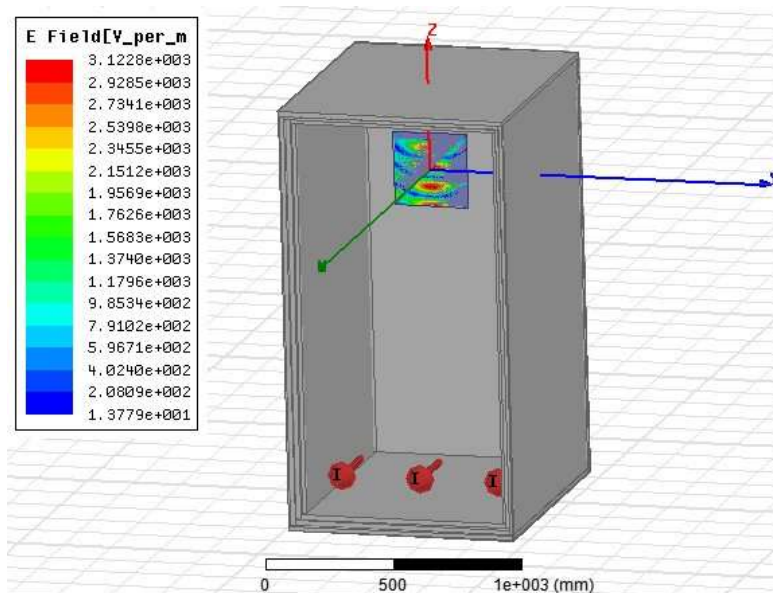


Figure 3.2: HFSS Chamber Model of a Small Chamber

on the simulation. The number of antennas and spacing of the antennas is as defined in the MATLAB simulation in the previous section. Figure 3.2 illustrates the chamber as modeled in HFSS. Note that the Hertzian dipole antennas are illustrated as arrows in the chamber model, with the tail indicating the location of the antenna, and the cone-shaped head indicating the polarization of the antenna.

3.3 Analytical Results

In an effort to determine the feasibility of various chamber configurations in synthesizing a Laplacian PAS field of various azimuthal spreads, a MATLAB script performed a Monte Carlo analysis for each configuration to determine the reflectivity distribution (as detailed in Sec. 3.2). The mean and standard deviation of the reflectivity was determined to within 95% confidence of being within an error of 0.25 dB.

The results of the simulations with horn antenna radiation pattern are analyzed with -15 dB as the maximum level of reflectivity. General trends of the 324 combinations of simulation parameters are that lower frequencies, lower test zone radius, smaller Laplacian spreads, and more antennas yield superior reflectivities. Eighty five configurations were observed with mean reflectivities below -15 dB.

In terms of frequency, 55 configurations with a frequency of 700 MHz, 29 configurations with a frequency of 2.4 GHz, and one configuration with a frequency of 5.9 GHz had a mean reflectivity of less than -15 dB. Clearly target fields of lower frequencies are easier to synthesize than those of higher frequencies. This is due to the longer wavelength of lower frequencies, resulting in lower variation across the test zone, which is easier to synthesize accurately.

In terms of test zone radius, 58 configurations with a test zone radius of 0.1 m, 26 configurations with a test zone radius of 0.15 m, and one configuration with a test zone radius of 0.2 m had a mean reflectivity of less than -15 dB. Target fields of a smaller test zone are easier to synthesize accurately than those of a larger test zone due to less variation in a smaller test zone when compared to a larger test zone at a fixed frequency of operation.

In terms of number of antennas, 9 configurations with 3 antennas, 14 configurations with 4 antennas, 27 configurations with 5 antennas, and 35 configurations with 6 antennas had a mean reflectivity of less than -15 dB. This indicates that target fields can be more accurately synthesized with a greater number of antennas. This is due to the fact that greater numbers of antennas can allow for greater variation of the synthesized test field.

In terms of Laplacian PAS spread, 32 configurations with a spread of $\sigma = 25$ degrees, 29 configurations with a spread of $\sigma = 35$ degrees, and 24 configurations with a spread of $\sigma = 45$ degrees had a mean reflectivity of less than -15 dB. This does not indicate a strong

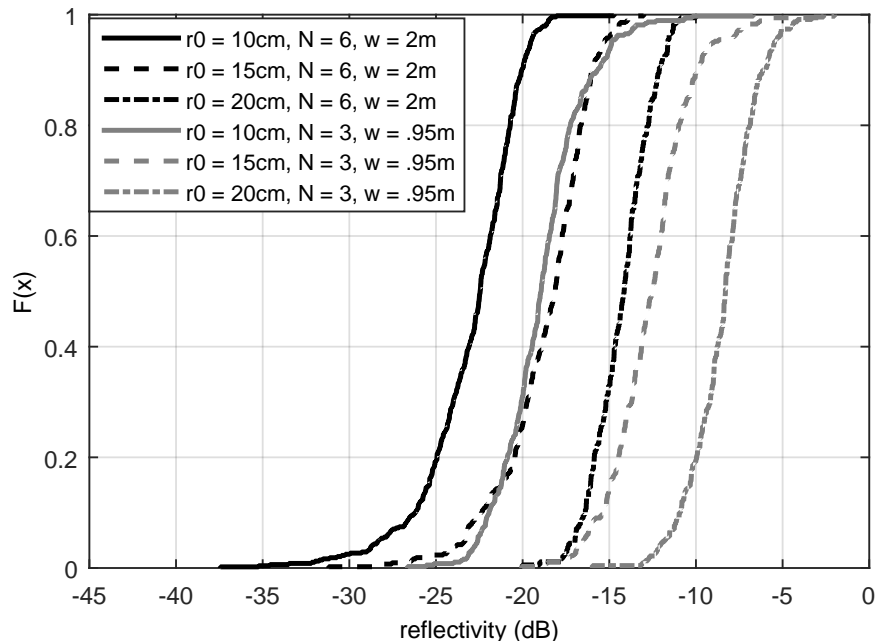


Figure 3.3: CDF of Reflectivity for Select Configurations, 700 MHz and 35 degree spread

trend between Laplacian PAS spread and accuracy of field synthesis. This is likely due to the fact that this field synthesis depends mostly on the direction of arrival of the power and thus there is more correlation between antenna spacing and Laplacian spread in terms of field synthesis accuracy. For wider Laplacian spreads, wider antenna spacings tend to produce more accurate field synthesis, while for narrow Laplacian spreads, smaller antenna spacings produce a more accurate synthesized field.

As for the distribution of the reflectivity, the majority of the observed standard deviations fall between 2 dB and 3 dB in the configurations with mean reflectivity below -15 dB. Figure 3.3 shows the distribution of two sample configurations at 700 MHz with a 35 degree spread, a larger chamber 2m wide with 6 probe antennas, and another chamber 0.95 m wide with 3 probe antennas.

The Laplacian spread of $\sigma = 35^\circ$ is particularly important, as it occurs as the spread

for the Laplacian PAS in numerous standards [20]; chamber configurations with a spread of 35 degrees are evaluated. For the smaller chamber (antenna array width = 0.95 m) with 3 antennas is considered, the only acceptable configuration is with a test zone radius of 10 cm. With 6 antennas, a test zone radius of 10 cm and 15 cm are acceptable. If the width is set to 2 m and the number of antennas to 5 or 6, a 15 cm test zone radius is achieved for 5 antennas at 700 MHz and 6 antennas at both 700 MHz and 2.4 GHz. A 10 cm test zone radius is achieved for 5 antennas and 2.4 GHz.

3.4 Electromagnetic Simulation Results

After investigating the synthesis of the E-field with horn probe antennas in a test zone in MATLAB, further investigation was performed on the synthesis of the E-field using Hertzian dipole antennas using both MATLAB and Ansys HFSS. First, the simulations were performed in MATLAB as described in section 3.2 for the subset of configurations that will be replicated in HFSS. Next, as described previously, the chamber was modeled twice in HFSS, first with all parts of the chamber set to a vacuum material (to for direct comparison of HFSS results to those produced in MATLAB), and then with the materials set to a stainless steel enclosure and three-layer absorber to model an actual chamber. The simulations were performed with vertical polarization for both the target field and the probe antennas.

HFSS simulation results were observed to have a different zero-phase point for the field generated from each Hertzian dipole antenna with respect to that calculated in MATLAB using ideal Hertzian dipole equations. As a result, the complex coefficients for each antenna calculated in MATLAB for generating a target field could not be used directly in HFSS. Instead, the E-field contribution of each Hertzian dipole probe antenna was measured separately at a set of 360 equally-spaced points around the test zone perimeter within

HFSS. Using this field data along with the target Laplacian PAS field calculated at the same points, 2-norm matching was performed to determine the complex weights to be applied to each Hertzian dipole probe antenna in HFSS. Also, because the resultant HFSS field data obtained after applying complex weights to each antenna matched that of the sum of the complex-weighted field data measured from each antenna separately (as expected), the resultant synthesized HFSS field could be calculated outside of HFSS (in MATLAB) directly from the unweighted field data in the test zone of each independent antenna. As a result, for each chamber configuration (solution frequency, antenna array size/configuration, chamber material), an unweighted field was measured at a set of test zone points from each antenna in HFSS, and this field data was exported.

Table 3.2: Simulation Results

r_0 (m)	N	Lap. σ	Freq. (GHz)	Width (m)	Matlab, vacuum		HFSS, vacuum		HFSS, chamber	
					mean ref. (dB)	std. dev. ref. (dB)	mean ref. (dB)	std. dev. ref. (dB)	mean ref. (dB)	std. dev. ref. (dB)
0.1	6	25°	0.7	2.0	-36.72	2.42	-36.28	2.27	-21.51	4.46
0.1	6	35°	0.7	2.0	-34.69	3.52	-34.27	3.41	-22.17	4.47
0.1	6	45°	0.7	2.0	-30.79	4.56	-30.32	4.59	-22.42	4.76
0.1	3	25°	2.0	0.95	-17.15	3.70	-17.33	3.98	-15.12	2.98
0.1	3	35°	2.0	0.95	-14.37	3.65	-13.47	3.58	-12.99	3.17
0.1	3	45°	2.0	0.95	-12.27	3.57	-11.39	3.42	-11.08	3.13

From this HFSS measured field data from each antenna for each chamber configuration, a MATLAB script was developed which determined complex antenna coefficients using the method described in the previous paragraph. These coefficients were used to synthesize the field using the sum of weighted field data from each antenna. The reflectivity of the

synthesized field was determined by comparing it to the target field at the radius of the test zone. A Monte Carlo analysis was performed using this procedure to determine the mean and standard deviation of the reflectivity distribution to within a 95% confidence of being within 0.25 dB of the mean. The results of this simulation are also presented in Table 3.2.

From the results, one can see that the mean and standard deviation in the MATLAB simulations and the HFSS vacuum simulations are nearly identical, always within 1 dB of each other. This validates that the Hertzian dipole equations used in MATLAB are consistent with the Hertzian dipole simulated in HFSS.

The performance of the chamber was noticeably less than that of the vacuum, which is expected, as the presence of reflected power (due to imperfect absorption by the absorbing material) makes matching the synthesized field to the target field more difficult. The difference between the chamber and vacuum cases is most pronounced at 700 MHz, with a difference of nearly 10 to 15 dB. The difference between the chamber and vacuum cases was less pronounced at 2 GHz, with a difference of approximately 0.3 to 2.2 dB. This is due to the reduced contribution of reflected energy to the test zone field. This indicates that for 2 GHz, MATLAB simulations of Laplacian PAS synthesis in a vacuum will be reasonably close to that synthesized in an actual chamber, and can be used as a predictor of chamber performance.

Additional identical simulations were performed with horizontally-polarized Hertzian dipole antennas located in the same locations as the vertically-polarized antennas. The target field was generated using 360 plane waves in the same manner as above, but with polarizations tangential to the test zone circle in the direction of arrival. In all cases, both vacuum and simulated chamber, the reflectivity was observed to be approximately 1 dB, indicating significant error. As such, horizontally-polarized target fields are not able to be

reproduced accurately with this antenna configuration. An alternative implementation or configuration of horizontally-polarized antennas will likely synthesize horizontally-polarized fields accurately.

3.5 Conclusions

In this chapter, we have demonstrated through simulation that a small anechoic chamber (built with practical materials) can be successfully utilized as a MIMO-OTA test chamber for the sufficiently-accurate synthesis of a vertically-polarized single-cluster Laplacian PAS in a test zone under several frequencies and chamber configurations [12]. This investigation serves as a first step to identifying the performance capabilities and limitations of a small anechoic chamber in terms of test zone size, chamber size, number of probes, and frequency range.

The configuration of horizontally-polarized antennas such that a horizontally-polarized target field (i.e. a target E field with \hat{Y} and \hat{Z} vector components) can be synthesized must be investigated in future work, as our work showed that horizontally-polarized antennas co-located with vertically-polarized antennas failed to accurately synthesize a horizontally-polarized target field. One potential configuration will be an array of horizontally-polarized antennas in an array perpendicular to the array of vertically-polarized antennas, thus creating a “cross” of antennas at the bottom of the chamber. Another possibility is to create a more extensive 2-dimensional grid of antennas at the bottom of the chamber for both horizontal and vertical antenna polarizations, which may further increase the accuracy of the synthesized field of both polarizations.

In general, the investigation in this paper found that frequencies of 700 MHz and 2.0 GHz, Laplacian PAS distributions with standard deviations of 25 and 35 degrees, and a test zone

radius of 10 cm have been shown to produce or nearly produce a sufficiently low reflectivity figure in the test zone. Further study of probe number and chamber dimensions may expand the capabilities of the chamber.

The use of actual horn antennas rather than ideal Hertzian dipole antennas in HFSS is an important next step in future work. This will investigate the impact of non-ideal effects such as coupling and reflections between antennas that will lower the performance of the system.

One final area requiring further study is the determination of complex antenna weights from actual field measurements around the test zone. Measurements must be performed using an antenna in the test zone to estimate the contribution of each probe antenna to the field in the test zone. Previous work has been performed in this area [22] in order to overcome near-field effects, reflections and scattering in a ring chamber in generating a plane wave. A similar procedure can be employed in a small anechoic chamber to overcome these same non-ideal properties.

CHAPTER 4

Near-Field Channel Model Framework

The purpose of this chapter is to develop a mathematical framework for describing the narrowband RF channel within a small anechoic chamber. This framework extends a complex numerical model into a relatively simple mathematical approximation that can be applied to both calculated and measured channels. This approximation serves as the basis for the work in the following chapter, which expands this method to a refined wideband model. This model can then be used for the purpose of MIMO system analysis, the ultimate goal of this work.

The small chamber will most often utilize an array of log-periodic probe antennas with fixed positions and orientations and an array of DUT antennas, which will be for the purpose of analysis defined as dipole antennas. As a first approximation, a SISO channel between a single log-periodic probe antenna (which consists of an array of co-polarized dipoles) and a single dipole DUT antenna (of arbitrary orientation relative to the log-periodic array) is modeled in free space.

Fig. 4.1 shows the breakdown of contributions in chapters 4 and 5. The contributions for this chapter are emphasized in bold.

The first contribution of this chapter is the formulation of a numerical method for determining the channel between arrays of dipole antennas with arbitrary orientations and spacings, which can then be adapted to a general array consisting of the log-periodic antenna (an array of dipoles) and an additional DUT dipole. In the literature investigated in Chapter 2, every treatment of the near-field of dipole antennas and mutual-impedance makes

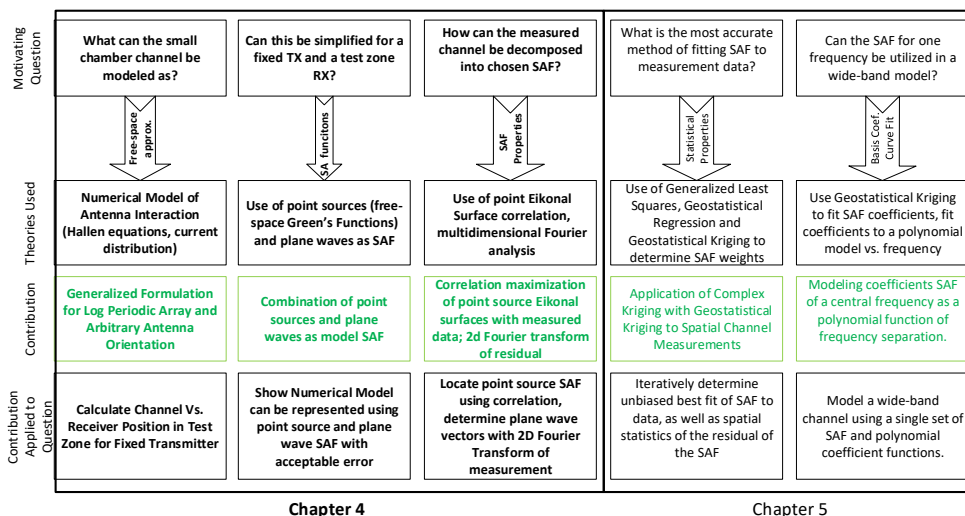


Figure 4.1: Chapter 4 Contribution Flowchart

the assumption of co-polarized dipole antennas, which yields expressions and equations not directly applicable to arrays of arbitrary orientation. Combined with transmission line theory for feeding the log-periodic antenna, an impedance matrix relating each and every dipole port is constructed, which can be used to relate currents and voltages, and in turn produce an expression for the channel from the input of the log-periodic antenna to the output of the DUT dipole.

The second contribution of this chapter is a justification of the usage of plane waves and point sources as joint basis functions for describing and modeling an arbitrary channel. Modeling a channel as a function of DUT dipole position in terms of simple basis functions is far less computationally-complex than computing the channel using the numerical method described previously. In addition, basis functions that describe the numerical channel within acceptable accuracy can be utilized to model measured channel data with additional super-imposed features such as reflections. This novel method of joint basis functions provides

a reduction in the number of terms required to express the channel relative to using plane waves as basis functions alone.

The final contribution of this chapter is a method to fit the joint basis functions, described in the previous section, to a numerical channel or measured channel data. A correlation method for iteratively fitting point sources to sampled or calculated data followed by selecting a series of plane waves by performing Fourier analysis on the residual is utilized as a method for selecting which basis functions to use for the channel model and determine the complex weights of each basis function.

The following section (4.1) outlines the adapted numerical method for calculating the channel between two ports in an arbitrary-orientation dipole array. Section 4.2 outlines the justification and advantage for the usage of point sources and plane waves as joint basis functions. Section 4.3 proposes a method of fitting the joint basis functions from section 4.2 to channel data (calculated or measured), and illustrates the validity of the usage of joint basis functions using a channel calculated from section 4.1.

4.1 Formulation of Channel using Dipole Arrays

The contributions of this section are as noted the first column of Fig. 4.1. In this section, we extend the work of Orfanidis [19], extrapolating the work presented in chapter 25 (Coupled Antennas), Sections 1 through 5 for arbitrary-oriented dipoles instead of Z -oriented dipoles, non-parallel dipoles, or coplanar dipoles. In addition, a four-term current distribution approximation for each dipole is utilized instead of the sinusoidal assumption due to the fact that some elements in a log periodic array will be significantly longer than a half-wavelength.

The motivation of this extension is to find the mutual- and self-impedance at each element

in the system in free-space, which is used in a system of equations to find the voltage at the receiving dipole or dipoles presented over a load for a unit input. This is the free-space channel from probe input to receiver output, including near-field effects, coupling, and all antenna properties. Because the far-field approximation does not hold (as the short distance leads to non-planar wave fronts in the test zone, and fields and gains that vary significantly in the proximity of the transmit antennas), the concept of antenna gain patterns and angle of arrival have limited meaning, as electric fields from one element to another do not follow a typical distribution across the antenna as if the incident field was a plane wave with definite direction of arrival. While reflected wave components may exhibit a plane wave-like behavior at the receiver due to the increased travel distance of the wave between transmitter and receiver, the dominant line of sight field and some reflections may not. In free space, the only field of interest will be the line of sight case, meaning the line of sight case can be analyzed for choice of channel approximation basis in the non-far field, as well as the conditions in which this approximation of basis holds.

The free-space system that approximates the line of sight conditions of the channel to be modeled is the first task in the choice approximation basis function. The channel of interest to be modeled consists of probe antenna log-periodic arrays each with fourteen-elements, oriented on a plane perpendicular to the X-Y plane and with bore sight aimed at the center of the projection of the region of possible DUT positions onto the X-Y plane, and DUT dipoles oriented in the Z direction, with centers located along a plane parallel to the X-Y plane. As a first approximation, a single log-periodic antenna and a single dipole (SISO channel) will be analyzed.

4.1.1 Mathematical Channel Model with Arbitrary Dipole Orientations

To model the channel from a log-periodic antenna to a dipole antenna, a mathematical relation between the input of the log-periodic antenna and output of the dipole must be established. To accomplish this, the current distribution on each antenna element and the electric fields of each antenna must be established, and the mutual- and self-impedances of all elements must be calculated. Refer to Chapter 2, specifically 2.3, for the procedure of deriving these values for dipole antennas.

A review of the final equations and variable definitions established in the preliminary sections is reproduced here for clarity. Let a system of any arbitrary two antennas from the dipole array be defined as antennas m and n , with arbitrary vector orientations \hat{r}_m and \hat{r}_n respectively. Figure 4.2 illustrates the variables used in this system.

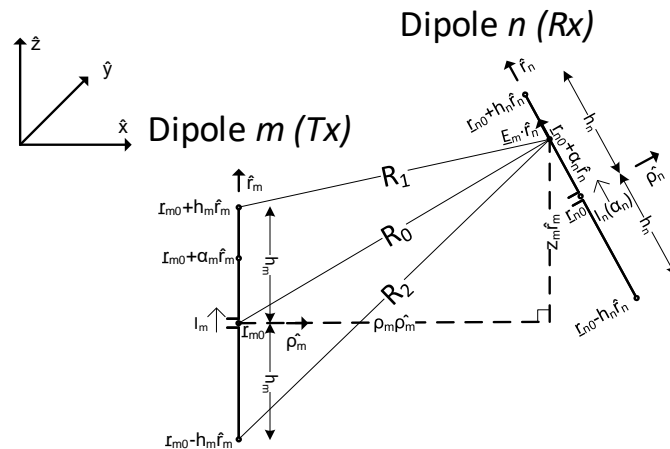


Figure 4.2: Dipole Mutual Impedance Formulation

The two dipoles have centers at \vec{r}_{m_0} and \vec{r}_{n_0} respectively, and half-lengths h_m and h_n respectively. The field observation position vector from antenna m is now a position on antenna n , $\vec{r}_{n_0} + \alpha_n \hat{r}_n$ (antenna n center position vector plus a scaled version of antenna n orientation vector \hat{r}_n , scaled by α_n which can vary from $-h_n$ to h_n) rather than an arbitrary point in space. Using this definition, the variables z_m and ρ_m , cylindrical coordinates of a point on antenna n relative to the center of antenna m , can be related to the position on antenna n with the following equation:

$$\vec{r}_{n_0} + \alpha_n \hat{r}_n = \vec{r}_{m_0} + z_m \hat{r}_m + \rho_m \hat{\rho}_m \quad (4.1)$$

z_m and ρ_m can be calculated in terms of α_n with vector projection and rejection as performed in Chapter 2. These variables can be used to define the electric field from antenna m along antenna n , $E_{\hat{r}_m}(z_m, \rho_m) + E_{\hat{\rho}_m}(z_m, \rho_m)$, or in terms of α_n , $\vec{E}_{nm}(\alpha_n) = E_{\hat{r}_m}(\alpha_n) + E_{\hat{\rho}_m}(\alpha_n)$. Finally, this electric field can be projected onto the orientation vector \hat{r}_n to determine the electric field component along antenna n , $E_{\hat{r}_n}(\alpha_n)$.

The current along each antenna (e.g. $I(\alpha_m)$ along antenna m) is determined with a numerical 3-term approximation as discussed in Chapter 2. Orfanidis defines a procedure to numerically compute the current distribution of the antenna utilizing Hallen equation solutions “with point-matching, pulse basis functions, and exact kernel with $M = 100$ upper-half current samples” [19]. A detailed explanation of this process is provided in Chapter 2.

Using the current distribution and electric field equations, the mutual impedance of the antenna n on the antenna m can be calculated. First, the induced open-circuit voltage on antenna n due to antenna m is:

$$V_{nm,oc} = -\frac{1}{I_n} \int_{-h_n}^{h_n} (\vec{E}_{nm}(\alpha_n) \cdot \hat{r}_n) I_n(\alpha_n) d\alpha_n \quad (4.2)$$

where I_n is the short-circuit current at the center of antenna n ($\alpha_n = 0$). Finally, using $I_m = I_m(0)$ and $I_n = I_n(0)$, and the open-circuit voltage equation 4.2, the mutual impedance is defined as:

$$Z_{nm} = \frac{V_{nm,oc}}{I_m} = -\frac{1}{I_m I_n} \int_{-h_n}^{h_n} (\vec{E}_{nm}(\alpha_n) \cdot \hat{r}_n) I_n(\alpha_n) d\alpha_n \quad (4.3)$$

In addition to mutual impedance between each and every combination of elements in the system (both within the log-periodic antenna and between the elements of the log periodic antenna and the receiving dipole antenna), the self-impedance of each element must be calculated. Figure 4.3 shows a horizontally-magnified dipole antenna m , with radius a_m . All other variables remain the same as for the previously presented electric field analysis of dipole m . The self-impedance can be calculated with the same formula as with mutual-impedance, treating the surface of the antenna, $\vec{r}_{m0} + \alpha_m \hat{r}_m + a_m \hat{\rho}_m$, as the “second antenna” along which the electric field is calculated for the impedance (4.3) [19]. Because the two aspects of the same antenna are oriented identically in the \hat{r}_m direction, only the \hat{r}_m component of the E field will be present in the impedance calculation.

The port of each dipole element in the M-element log-periodic antenna plus the port of the single receiving dipole forms an $M + 1$ port network, as shown in Figure 4.4. Using the procedures described to determine the mutual- and self- impedance of a pair of arbitrarily-oriented dipoles, an impedance matrix for the $M + 1$ port network can be constructed, with each element (i, j) of the matrix describing the trans-impedance of element i on element j . The trans-impedance matrix can be converted to the trans-admittance matrix, necessary for

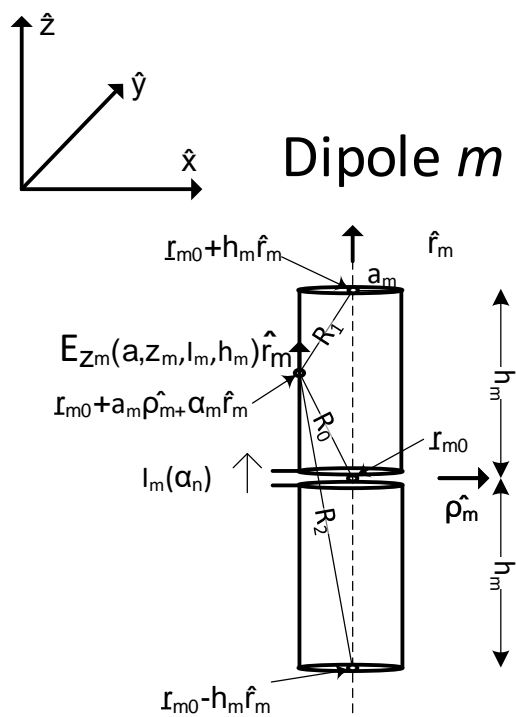


Figure 4.3: Dipole Self Impedance Formulation

combining two networks in parallel, using the following relation:

$$\mathbf{Y}_A = \mathbf{Z}_A^{-1} \quad (4.4)$$

In parallel with this network of coupled antennas is a feedline network that feeds each antenna of the log-periodic array from a single excitation on port 1, as shown in Figure 4.5. The feedline network does not feed the receiving dipole antenna. Because the coupling of the feedline network onto the lone dipole and its load is significantly less than the coupled

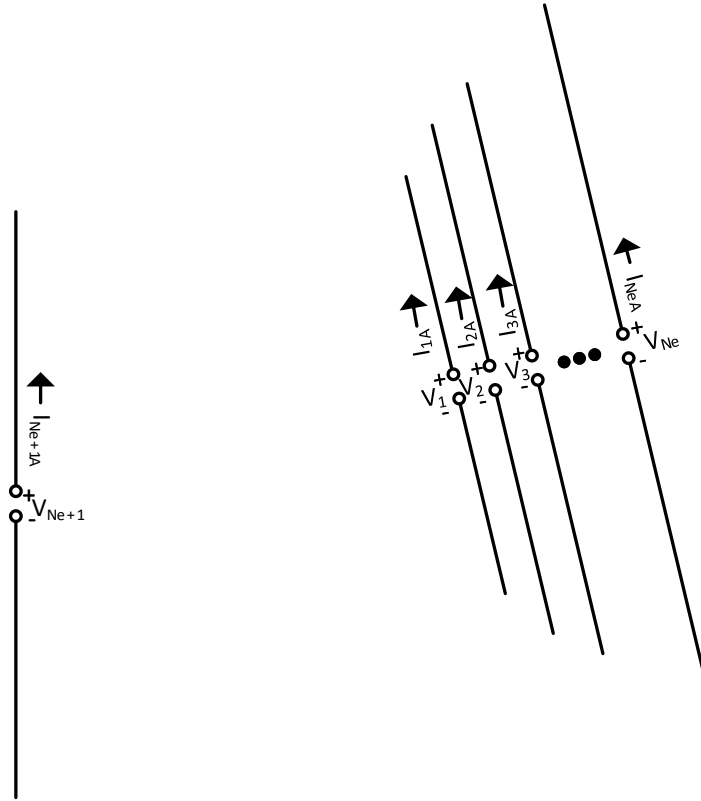


Figure 4.4: Antenna Array and Dipole Port Definitions

signal from the elements of the log-periodic array, it can be reasonably approximated as zero admittance from any log-periodic port to the dipole port. The feedline network can be described using transmission line theory; Stutzman and Thiele [51] present a feedline admittance matrix in Section 14.10 of their text *Antenna Theory and Design*. This matrix, for the log-periodic antenna alone, can be defined as \mathbf{Y}_{TLF} . Combining this with the zero admittance from the log-periodic array to the dipole antenna, a total network feedline admittance matrix can be defined in the following equation:

$$\mathbf{Y}_T = \begin{bmatrix} \mathbf{Y}_{TLP} & \mathbf{0} \\ \mathbf{0} & \mathbf{0} \end{bmatrix} \quad (4.5)$$

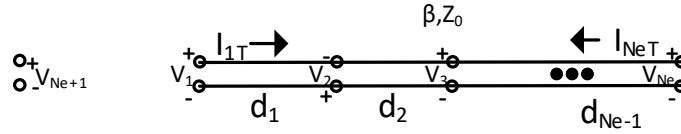


Figure 4.5: Transmission Line Network Definition

Finally, the admittance networks Y_T and Y_A are defined as in parallel for the 15 ports, as in Figure 4.6. Because these two networks are in parallel, the admittance matrices can simply be added to form the admittance matrix for the entire 15 port network.

$$\mathbf{Y} = \mathbf{Y}_A + \mathbf{Y}_T \quad (4.6)$$

The admittance matrix can be inverted to obtain the system impedance matrix $\mathbf{Z} = \mathbf{Y}^{-1}$ for the entire network. The column vectors of the voltages and currents of the $M + 1$ port network, as shown in Figure 4.6, are defined as \vec{V} and \vec{I} respectively. Applying the basic relationship between currents and voltages at the ports of the network, we have $\vec{V} = \mathbf{Z}\vec{I}$.

If we rearrange this equation such that the right hand side equals zero, using an identity matrix \mathbf{I} , and combining the voltage and current vectors into a single column vector through vertical concatenation, we have:

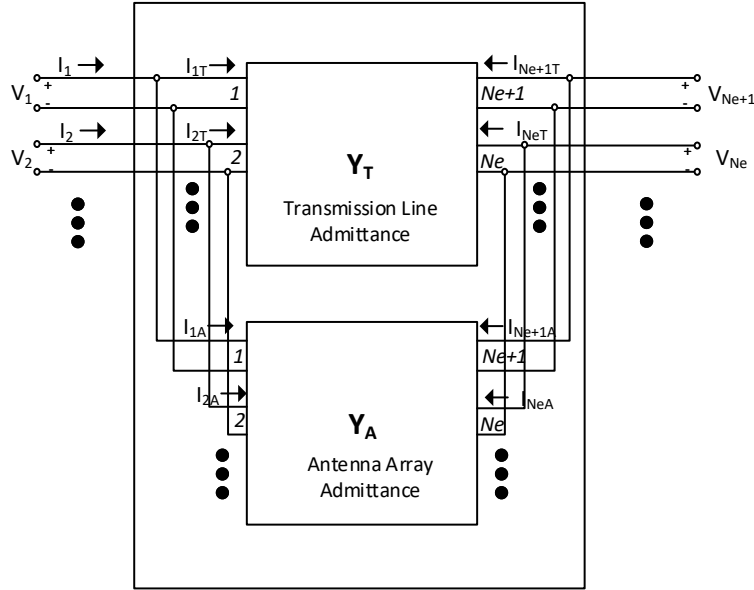


Figure 4.6: Definition of Parallel Admittance Networks

$$\begin{bmatrix} -\mathbf{I} & \mathbf{Z} \end{bmatrix} \begin{bmatrix} \vec{V} \\ \vec{I} \end{bmatrix} = \vec{0} \quad (4.7)$$

In addition to this set of equations, we must define two more to obtain a channel matrix from this set of equations. The first is to define the input voltage, $V_1 = 1$ applied at port 1. The added equation row will therefore have a 1 at the column corresponding to V_1 in the column vector, and has a 1 appended to the end of the right-hand side column vector. This forces V_1 to 1 in the system of equations.

Secondly, we know that the current at port $M + 1$ (I_{M+1}), the dipole, times the load impedance attached to the dipole, Z_L , is equal to V_{M+1} . Therefore, $-V_{M+1} + I_{M+1}Z_L = 0$. The added row to the left hand side matrix should have -1 at the column corresponding

to V_{M+1} , and Z_L in the column corresponding to I_{N_e+1} , and zero appended to the column vector on the right-hand side.

$$\begin{bmatrix} -\mathbf{I} & \mathbf{Z} \\ 1 & \vec{0} \\ \vec{0}1 & \vec{0}Z_L \end{bmatrix} \begin{bmatrix} \vec{V} \\ \vec{I} \end{bmatrix} = \begin{bmatrix} \vec{0} \\ 1 \\ 0 \end{bmatrix} \quad (4.8)$$

If we define the left hand side matrix as \mathbf{A} , and the right hand side vector as \vec{b} , then the vector of voltages and currents can be solved for by taking the pseudoinverse of \mathbf{A} times \vec{b} .

$$\begin{bmatrix} \vec{V} \\ \vec{I} \end{bmatrix} = \mathbf{A}^\dagger \vec{b} \quad (4.9)$$

where \mathbf{A}^\dagger is the pseudoinverse of \mathbf{A} . Finally, the channel can be determined by taking the ratio of the output voltage, V_{M+1} , to the input voltage, V_1 .

$$H = \frac{V_{M+1}}{V_1} \quad (4.10)$$

The channel can be described as a complex function of the positions, orientations, lengths of all $M + 1$ elements, and frequency, using equations in this section. However, because M of the elements are included in the log-periodic antenna, these elements are of fixed length relations, related position and spacing, and common orientation. The receiver dipole will also have a fixed length. As a result, the channel is a function of log-periodic position and orientation, and dipole position and orientation. Due to the configuration of the small chamber for which the channel modeling is being performed, the log-periodic antennas can be considered to have fixed position and orientation for a small number of discrete locations

in the chamber. The receiver dipole, however, may be located anywhere near the chamber center. In short, a meaningful channel model for the purposes of our analysis will be a function of receiver position and orientation only. For simplicity, a single receiver orientation is considered (Z-oriented) and a fixed position height is considered. As such, the channel model in proceeding sections will be a function of X-Y receiver position and frequency only, and a separate model will be determined for each of several defined log-periodic positions and orientations.

4.1.2 Numerical Computation of Dipole Array Channel

A general procedure to numerically calculate the channel using the equations described in the previous section is as follows. First, the position and orientation vectors, lengths, and radii for each dipole in the system are defined, as well as the frequency of analysis. Next, each and every pair of antenna elements i, j are selected pair by pair (including cases where $i = j$). The current distribution along antennas i and j are calculated using point matching, pulse basis functions, and King's 3-term approximation, as discussed in the previous section. This approximation determines three fit coefficients used in standard expressions for accurately modeling current distribution. The current distribution for antenna i is used in integral equations defining the electric field due to i at points along antenna j . The electric field along j due to i is used in conjunction with the current distribution on j in integral equations to determine the mutual impedance of j on i .

Each of these integrations is performed using the Gauss-Legendre method, a numerical method of approximating an integral, which first algorithmically selects a vector of locations along the antenna being integrated over and corresponding weights. The integrand is then evaluated at each of the locations in the vector along i . Finally, the vector of integrands

is multiplied by the corresponding weights and summed, with the sum approximating the integral. For each point α_j selected along j , use Gauss-Legendre to calculate the electric field due to i on j , $\vec{E}_{ji}(\alpha_j)$, (and in turn the entire integrand for the mutual impedance equation), then use Gauss-Legendre again to calculate the integral in the mutual impedance (4.3). If $i = j$, then perform the procedure using the surface of the antenna (at the radius of the dipole) as antenna j and the center of the antenna as antenna i ; both have identical sample points along the antenna and identical current distribution.

Populate an impedance matrix with the mutual- and self-impedances calculated with double Gauss-Legendre integration. Take the inverse of this to produce the admittance matrix of the antenna network, \mathbf{Y}_A . Calculate the transmission line network admittance matrix between the log periodic elements \mathbf{Y}_{LP} using the procedure discussed in the previous section, and then form the matrix \mathbf{Y}_T as in (4.5). Sum the admittance matrices to determine the system admittance matrix \mathbf{Y} as in (4.6). Take the inverse of Y to obtain the system impedance network \mathbf{Z} . Using (4.8) to relate the voltages and currents of the system, define unit excitation at the input port of the log-periodic antenna, and the dipole voltage equal to the dipole current times the antenna load, and solve the system of equations using (4.9). Finally, extract the voltages at the log-periodic input and dipole output, and calculate the channel as in (4.10).

As explained in the previous section, we wish to model the channel as a function of DUT dipole position and frequency. Using the procedure just described, the channel can be calculated for a series of DUT dipole locations comparable to a range of DUT dipole locations in the chamber being modeled.

4.1.3 Numerical Computation Setup and Results

The described numerical computation method is applied to a fourteen-element log-periodic and dipole antenna of typical position and orientation in a small anechoic chamber. An operating frequency of 5.45 GHz is chosen, at the center of the 5 GHz ISM bands. An Octoscope BOX-38 small anechoic chamber has interior dimensions of 81 cm width (x), 55 cm depth (y), and 49 cm height (z). The receiving dipole in this simulation is a z -oriented half-wave dipole (with λ corresponding to 5.45 GHz), and with a center z coordinate fixed at 15.3 cm (to match the dipole z coordinate in a subsequent measurement campaign). The x and y positions are varied in an approximately 22 cm by 19 cm rectangular test zone (large enough to include most small devices under test (DUT)) centered on the center of the chamber floor. The log periodic antenna is modeled after the probe antenna used in conjunction with Octoscope's BOX-38 for WiFi testing. It has a value of $\tau = 0.85$, and element lengths from 0.64 cm to 6.2 cm. The coordinate of the tip of the log periodic antenna is approximately (0.7,-0.44, 0.27) in meters with the bottom/back/left of the chamber defined as the origin and the up/away/right directions when facing the front of the chamber are the positive directions of the x , y , and z axes respectively. The orientation of the dipole is boresight in the direction of the center of the interior bottom floor of the chamber, along a plane perpendicular to the floor of the chamber. Fig. 4.7 illustrates the system as described, with the black outline representing the boundaries of the chamber interior, the green rectangle representing the boundaries of the test zone along which the blue dipole will move, and a red fourteen-element log-periodic antenna near the front/right/top corner of the chamber. As a first-approximation, the system is modeled as the log periodic and dipole antennas in free-space, without any interactions with the chamber.

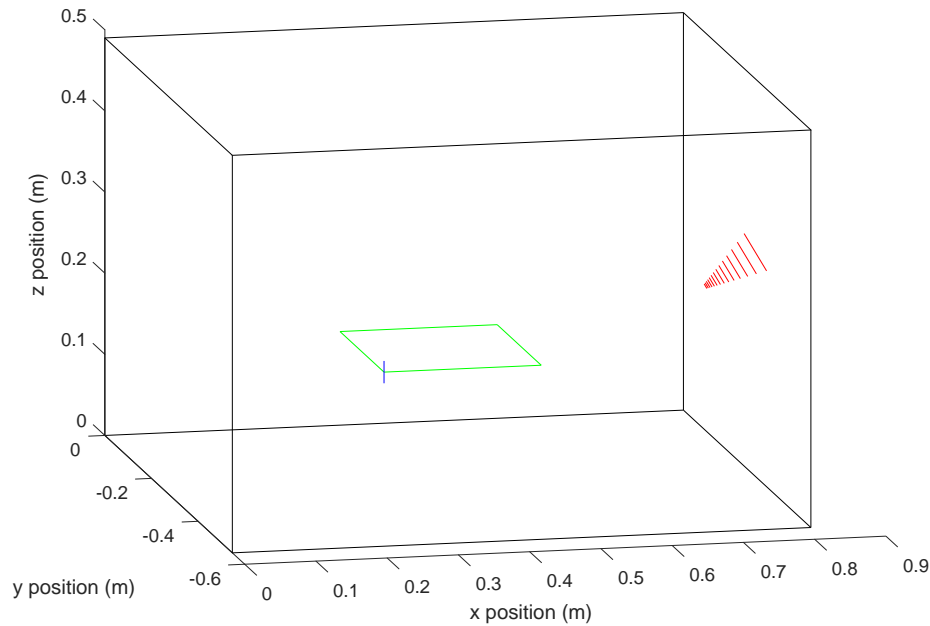


Figure 4.7: Modeled System for Numerical Computation

The channel between the log periodic input and dipole output is calculated on a grid of 17 evenly-spaced x by 14 evenly-spaced y receiver positions spanning the entire test zone, resulting in test zone sample spacings of 0.26λ in the y direction and 0.25λ in the x direction. Because the system is only being analyzed with a single frequency excitation, the free-space electric field should be limited to a spatial period of λ in any direction, and therefore sample spacing should be at most 0.5λ in each direction if discrete Fourier analysis is to be performed on the sampled field. This will be important in subsequent sections, so a sample spacing choice that meets this requirement was selected to meet this requirement. Using the sample spacing of the channel (which is proportional to the electric field) of 0.25λ is a sample density of approximately double the minimum requirement, and is therefore sufficient to prevent aliasing in Fourier analysis. This will also allow the observation of

spatial variation of the electric field phase structure (or more specifically, the structure of the corresponding channel) which will aid in selection of modeling functions.

The following plots show the resultant channel between the log periodic antenna and dipole antenna for dipole positions over the test area defined above. Fig. 4.8 shows the channel magnitude versus dipole position. As expected, if one considers the gain patterns of dipole antennas and log periodic antennas, one would expect the channel to have lower gain when the signal propagates away from the log periodic antenna at an angle farther away from boresight (e.g. when the receiver is below the boresight direction of the antenna) and when the signal propagates toward the dipole from a direction approaching parallel to the dipole orientation, even in the case of close proximity. The log periodic antenna is located beyond the lower right corner of the x and y range of the plot, and this corner of the plot has slightly decreased gain relative to the rest of the test zone despite closer proximity as expected. The remainder of the test zone has a path from transmitter to receiver in higher gain regions of the transmit and receive antenna gain patterns, so we expect that the channel magnitude would slowly fall off with increased distance between transmit and receive antennas, which is exactly what happens; the channel gain slowly rolls off as the receiving antenna moves towards the upper left part of the plot. In short, the magnitude of the numerical channel is as expected.

Fig. 4.9 shows the channel phase shift versus dipole position. Due to the relatively coarse sampling of the channel over the test zone, combined with the discontinuity as phase transitions from $-\pi$ to π , the interpolated phase plot is quite jagged along the discontinuity. Despite this, it is clear that the equiphase fronts have a well-defined curvature, emanating from a point or region located below the lower right corner of the plot, exactly where the antenna is located. Therefore the phase of the numerical channel is also as expected.

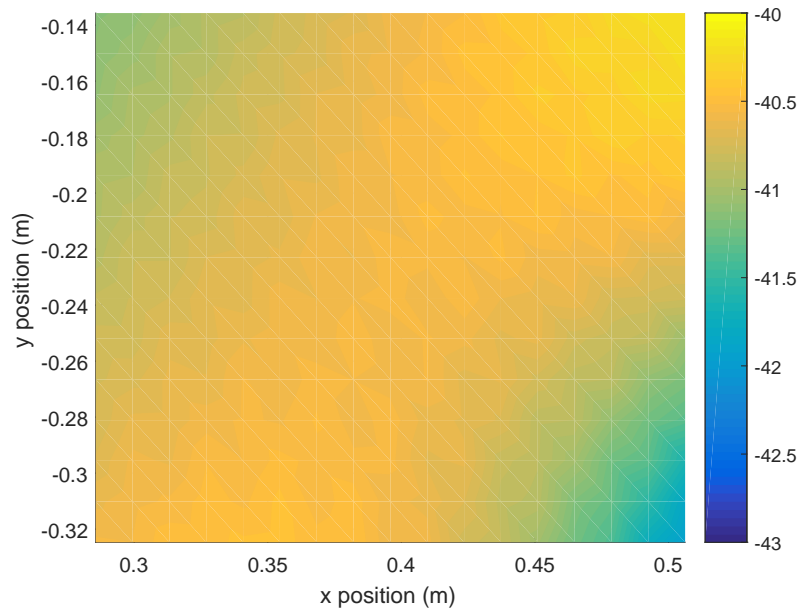


Figure 4.8: Magnitude of Channel Vs. Dipole Position

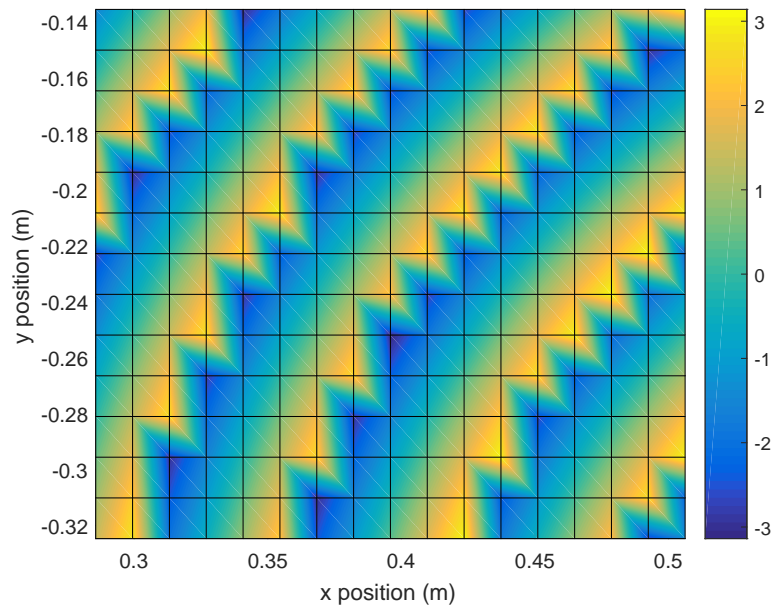


Figure 4.9: Phase of Channel Vs. Dipole Position

Due to the presence of curved wave fronts almost as if emanating from a point in space, it is logical to consider using a complex-weighted field from a point source as a first approximation of the channel. To refine the channel, a spectral decomposition of the residual from the point source can be used to select dominant plane wave components and their corresponding weights to be summed with the weighted point source approximation. The following section outlines the theory behind this method, a procedure for its implementation, and validation of the model error relative to the modeled numerically-computed field.

4.2 Dipole Array Channel with Spatial Attribute Function Decomposition

The second contribution of this chapter, as noted in the second column of Fig. 4.1, is presented in this section. We investigate a spatial modeling framework as presented by Smith in his course on Spatial Data Analysis, specifically from the section on General Spatial Prediction Models [52]. Here we model a deterministic “global” trend $\mu(\vec{r})$ (where \vec{r} is spatial position in the observation region) from the sampled spatial channel $H(\vec{r})$. In the following chapter we analyze the statistical properties of the residual $\varepsilon(\vec{r})$, where $\varepsilon(\vec{r}) = H(\vec{r}) - \mu(\vec{r})$.

In [52], the global trend $\mu(\vec{r})$ is modeled as the weighted sum of spatial attribute functions. A spatial attribute function is a smooth, finite and continuous function over a sampled observation region (in our case, the rectangular test zone). Each spatial attribute function $x_k(\vec{r})$ is weighted by a constant term β_k (which is determined through fitting of the spatial attribute functions to the sampled data). A constant term β_0 is included in the model to include any constant mean term over the sampled region. This sum of weighted spatial attribute functions defines the global trend as $\mu(\vec{r}) = \beta_0 + \sum_{k=1}^K \beta_k x_k(\vec{r})$, where K is the

number of spatial attribute functions. Let \mathbf{X} be a matrix where each row corresponds to each observation position \vec{r}_j of J observation positions. The first column, column 0, of \mathbf{X} is populated with $1 + i$ (corresponding to a complex β_0). Each subsequent column k is populated with the value of $x_k(\vec{r}_j)$. The size of \mathbf{X} is therefore J by $K + 1$. Assign β_0 through β_K to a column vector $\vec{\beta}$, containing all $K + 1$ complex weights. Using \mathbf{X} and $\vec{\beta}$, a vector of global trend values at each observation point can be defined as in (4.11).

$$\vec{\mu} = \mathbf{X}\vec{\beta} \quad (4.11)$$

This can be used in the expression for the residual as in (4.12).

$$\vec{\varepsilon} = \vec{H} - \mathbf{X}\vec{\beta} \quad (4.12)$$

If we assume that $\vec{\beta}$ should be chosen to minimize the residual $\vec{\varepsilon}$, we can use ordinary least squares to solve for $\vec{\beta}$ that best fits the spatial attribute functions to the observed data at the observation points. This leads to the additional restriction that the spatial attribute functions are pair-wise linearly-independent over the set of observation points, and thus $\mathbf{X}'\mathbf{X}$ must be non-singular [52]. The least squares solution of $\vec{\beta}$ is defined as in (4.13), which uses the Moore-Penrose pseudoinverse of \mathbf{X} .

$$\vec{\beta} = (\mathbf{X}'\mathbf{X})^{-1}\mathbf{X}'\vec{H} \quad (4.13)$$

It should be noted that $\mathbf{X}'\mathbf{X}$ forms a Gram matrix, each entry of which is in essence an inner-product over all observation points for each pair of spatial attribute functions (basis functions; each column of \mathbf{X} corresponds to the basis function evaluated at every observation

point). Diagonal-dominant matrices (i.e. ones where for each row the magnitude of the diagonal element is greater than the sum magnitude of all other elements) have the property of being non-singular [53]. Therefore choosing spatial attribute functions that make the Gram matrix diagonal-dominant would make it non-singular. If we can make non-diagonal elements of the Gram matrix small (either by pair-wise inner product threshold enforcement or by other properties of chosen functions), then we can make the Gram matrix diagonal-dominant, and thus non-singular.

4.2.1 Plane Waves as Spatial Attribute Functions

One candidate spatial attribute function is a plane wave. Any function in space can be described as the sum of an infinite number of three-dimensional plane waves. Each plane wave is described by a wave vector \vec{k} (defining spatial frequency and direction of travel), observation position \vec{r} , and complex weight containing magnitude and phase information E_0 . The plane wave equation Eqn. 4.14 is:

$$E_{PW}(\vec{r}) = E_0 e^{-j\vec{k}\cdot\vec{r}} \quad (4.14)$$

A three-dimensional Fourier Transform of a spatial function will express that function in terms of its wavenumber spectrum. Mersereau and Speake [54] illustrate the properties and use of multidimensional Fourier transforms, with discussion in terms of complex exponentials and general spectra rather than plane waves and wavenumber spectra, however the same general principles apply. Using spectral theory, if this spatial function is sampled in each dimension with sample spacings at most equal to the inverse of double the spatial frequency in any direction, and sampled over the entire volume of the desired signal volume, then the three-dimensional Discrete Fourier Transform (DFT) of the sampled signal will produce a

discrete wave vector spectrum [54].

The discrete wavevector spectrum has coordinates consisting of the wave vector \vec{k} of a plane wave, with the function value at that coordinate equal to the complex weight E_0 of the plane wave of that wave vector. Each of the unweighted exponential plane waves ($e^{-j\vec{k}\cdot\vec{r}}$) can be considered a spatial attribute function of the sampled signal, and the weights of each attribute function E_0 can be considered a corresponding β as defined in the previous section; the sum of weighted plane waves will reconstruct the sampled signal [54].

Certain aspects of discrete, space-limited spatial sampling must be considered in a similar way to signals sampled in time. The spatial sampled signal should be windowed to reduce false high-frequency components formed by the DFT algorithm (where the sampled region itself is assumed periodic itself in space, which would be discontinuous as opposite edges of the arbitrary sampled region are not continuations of each other. Discontinuities between assumed periods of a spatially-periodic signal contain frequency content that does not exist outside the context of assumed periodicity of a truncated sampled signal, and do not exist in reality). Also, the spatial sampled region may be zero-padded to increase wave vector resolution, and more accurately determine the wave vector of each spatial attribute function. Without zero padding, wave vector content between wave vectors in the wave vector domain will leak to surrounding wave vectors. Zero padding interpolates values in the wave vector domain, and will reach a peak at the wave vector of the actual dominant spectral component. The wave vector at the peak can then be extracted. It should be noted that while both windowing and zero padding will provide a more accurate picture of the wave vector content of a signal, the original signal has been altered prior to analysis and therefore values of the DFT output will no longer correspond to the exact complex coefficients for each wave vector and its corresponding plane wave.

Modeling a spatial function as an infinite sum of plane waves, or even a sum of every plane wave produced by a DFT, produces a cumbersome or impossibly large set of spatial attribute functions to be a useful channel model. A modest sacrifice of accuracy for a reduction in number of terms can be achieved by setting a minimum magnitude threshold for frequency domain components, and extracting only plane wave functions with weights exceeding this magnitude. Careful selection of this threshold must be performed to meet a desired or required accuracy, or alternatively, peak spectral components can be iteratively fit and removed until this level of accuracy is achieved. Utilizing the wave vector spectrum of a zero padded, windowed spatially sampled function allows for increased wave vector accuracy with each iteration (as well as avoidance of false peaks caused by the discontinuity due to assumed repetition of the sampled region), and as a result, fewer plane waves can be used to model a spatial function to a desired degree of accuracy.

In regards to plane waves in two and three dimensions, a plane wave in three dimensions is defined by a three-dimensional wave vector, and a three-dimensional plane wave observed on an arbitrary plane will appear as a two-dimensional plane wave with a wave vector equal to the projection of the three-dimensional wave vector onto the plane of observation. This results in a two-dimensional wave vector. If we assume that the observation region is on the X - Y plane, then the projection of the 3-D wave vector onto this plane is simply the x - and y - components of the wave vector, with the z -component discarded. The reasoning for this is that along the X - Y plane, the z component of the position vector is constant. The constant position z -component occurs in the plane wave exponential multiplied by the z -component of the wave vector, resulting in a constant additive term in the exponential function. This constant additive term can be factored out of the plane wave exponential as a constant phase shift term, leaving the plane wave term in terms of x and y position

only and their corresponding x and y wave vector components, which is the definition of a 2-D plane wave. Therefore a signal sampled in two-dimensional planar space, which consists of a sum of 3-D plane waves, can be modeled as a sum of 2-D plane waves. The wave vectors of these 2-D plane waves on the plane of interest can be determined using a two-dimensional Discrete Fourier Transform of the spatially-sampled function. Subsequently, the spatial attribute functions for the channel model can be reduced to 2-D plane waves if the observation region exists along a 2-D plane, thus reducing the complexity of the problem. (Also, without extending the sample space to include sampling along a third dimension, no spectral information along the third dimension can be ascertained.)

One final attribute of plane waves is how to ensure the pair-wise inner product of two plane waves is sufficiently low over all sample points in the observation region. Wave vectors extracted directly from the DFT output of the sampled function (without zero padding) will have integer-related periods over all spatial dimensions, and as a result are guaranteed to have a pair-wise inner product of zero over all sample points. However, as discussed before, spectral leakage due to spectral content falling between sampled wave vector points require multiple plane waves to represent that content, increasing model complexity. If wave vectors are determined from peaks of the DFT of the zero-padded function, the pair-wise wave vector spacing between plane waves is no longer guaranteed to produce an inner product of zero over the sampled region, which may result in a non-diagonal-dominant Gram matrix (which may not be non-singular). If the peaks of the zero-padded signal are used to determine wave vectors, then a test to exclude plane waves that have a pair-wise inner product above a defined threshold can be implemented. At the very least, a test to ensure a Gram matrix is non-singular should be implemented upon each additional chosen plane wave.

4.2.2 Point Sources as Spatial Attribute Functions

A second candidate spatial attribute function is a point source, the free-space Green's function solution to the Helmholtz equation [19]. This exponential function has the form:

$$E_{PS}(\vec{r}) = \frac{e^{-jk\|\vec{r}-\vec{r}_0\|}}{4\pi\|\vec{r}-\vec{r}_0\|} \quad (4.15)$$

where k is the wave number of the point source, \vec{r} is the observation position vector in space, and \vec{r}_0 is the point source position vector in space. The point source function occurs as a kernel in the integrals found in the dipole channel formulation in Sec. 4.1. Because integrals can be approximated as weighted Riemann sums of the arguments, it follows that the dipole electric field (and thus the dipole channel) could be roughly approximated with one or more weighted point sources.

Using point sources as an approximation function poses two problems. First is determining the location of each point source from sampled data. A method must be developed that can determine if sampled channel points contain an underlying signal that correlates to a point source at a specific point. Next is determining if each pair of point sources has a sufficiently low inner-product over the set of sample points, and excluding point sources that have a high inner product with previously selected point sources. This is important for creating a non-singular Gram matrix as explained in the previous section. With these two problems solved, a least-squares method can be utilized to determine the weights of the point sources that minimize the residual of the estimated channel.

4.2.3 Point Source Location

To solve the initial problem of locating one or more point sources, it is helpful to visualize a point source field, and its observation on a rectangular plane. Fig. 4.10 illustrates surfaces of constant phase from a point source. For a selected constant arbitrary phase, a point source excitation with constant wavenumber $k = \frac{2\pi}{\lambda}$, will have concentric spherical wavefronts corresponding with the selected arbitrary phase, each separated by the wavelength λ from the previous and subsequent wavefront. This is illustrated in Fig. 4.10 by the two red line segments, each labeled λ . In geometrical optics, these constant-phase surfaces are known as Eikonal surfaces [51].

If these Eikonal surfaces from a point source are observed on a flat rectangular observation region, as represented by the black rectangle in the figure, arc-shaped wavefronts are observed (Eikonal curves). The separation of these Eikonal curves along the plane are not λ and are not uniformly-spaced (as the point source is not co-planar with the observation region, and therefore the plane is not normal to the Eikonal surfaces). It should be noted that the observed phase in Fig. 4.9 has arc-shaped Eikonal curves similar to those in 4.10, which indicates that a point-source spatial attribute function may be a logical choice.

Any Eikonal surface pattern in a planar 2-dimensional sample region can be formed by a single point in a half-space above the plane of observation, and the reflection of that point in the half-space below the plane of observation. If we know which half-space in which the antenna is located, which is where the field originates and therefore where point source approximations should be located, we can determine a single, unique point from a set of Eikonal surfaces.

Keeping the wavenumber k of the analyzed system constant (and thus keeping frequency

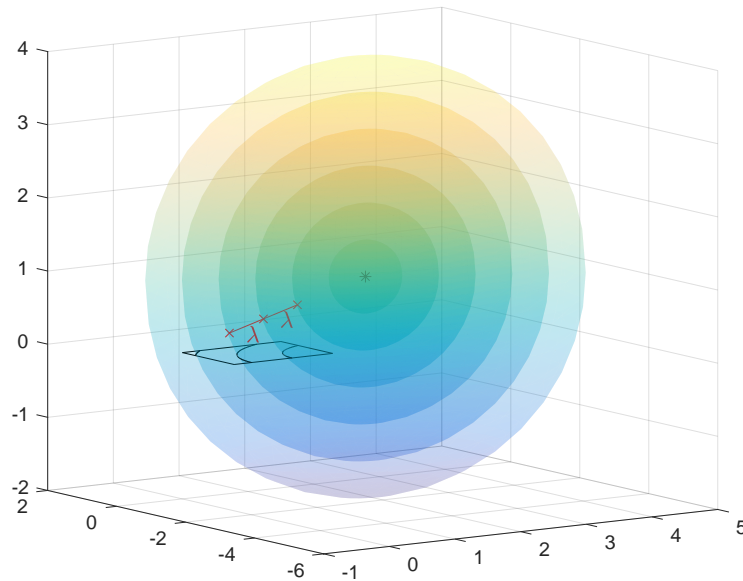


Figure 4.10: Visualization of Point Source Wave Fronts

and wavelength constant), a sampled channel in the rectangular observation region will consist of complex samples at each point, containing amplitude and phase information. The expected contribution of a point source at an arbitrary location \vec{r}_0 can be calculated at each and every observation point, and a correlation between the point source contribution and the sampled channel can be calculated. If the phase fronts (and as a result all phases) in the point source and an underlying component of the sampled channel align, then the magnitude of the correlation will be high.

Utilizing this property of high correlation at a likely point source, we can perform a global search of point sources \vec{r}_0 in the upper half-space above the observation plane to maximize the correlation between the point source and the sampled channel. The value of \vec{r}_0 at the maximum is a likely candidate point source. The sampled channel as a result contains

the Eikonal surface structure within the sampled data. This optimization problem can be expressed as in (4.16):

$$\hat{\vec{r}}_0 = \arg \max_{\vec{r}_0 | \vec{r}_{0z} > r_z} \left| \sum_{i=1}^N H(\vec{r}_i) e^{jk \|\vec{r}_i - \vec{r}_0\|} \right| \quad (4.16)$$

where $\hat{\vec{r}}_0$ is the estimated point source location, \vec{r}_0 is an arbitrary point source location, N is the number of channel sample points, r_z is the z-coordinate of the observation region, and $H(\vec{r}_i)$ is the sampled channel at observation point \vec{r}_i . A correlation threshold can be specified such that no value of $\hat{\vec{r}}_0$ is returned if the maximum value of the argument is below this threshold. This threshold value can be selected through experimentation, and can be used to prevent the selection of a point source if sufficient correlation with the sampled data is not achieved.

The estimated point source at $\hat{\vec{r}}_0$ from phase correlation maximization can then be fit to the observed channel data using least squares to obtain a complex coefficient and then subtracted from the sampled channel data to obtain a residual. Subsequent point sources can iteratively be extracted from and fit to the residual. However, care must be taken when selecting additional point sources to ensure a low inner-product with other point sources, which in turn will help prevent a singular Gram matrix.

4.2.4 Inner Product of Point Sources

With the determination of each additional candidate point source, a sufficiently-low inner product between it and every previous point source should be enforced, with new points with a high inner product being excluded for inclusion in the model. While performing this calculation for each and every candidate point is possible, an additional constraint on the optimization problem described in the previous section can be enforced to increase the

chances of finding a candidate point source with a low inner product with other previously-selected point sources.

Engquist and Zaho [55] investigated the separability of Helmholtz Green's functions at high frequencies. This paper establishes bounds on the inner-product between two point sources in an observation region as a function of their separation from each other and the observation zone. The formulation in this paper was too complex to implement as a constraint function for optimization. However, the principle that the inner product of two point sources decreases over an observation region as the separation increases provided motivation for performing a numerical analysis and empirical distribution of inner product versus point source separation distance.

For an observation zone matching the dimensions of the numerical computation sample zone in Sec. 4.1.3, a grid of sampled observation points with separation of $\frac{\lambda}{20}$ in both X and Y directions was established, and a 3-dimensional grid of potential source points spanning the width and height of the chamber and the depth of the chamber from a depth of a half-wavelength behind the observation zone to the rear of the chamber. The source point grid has a spacing of $\frac{\lambda}{3}$ in the X , Y , and Z directions. Every inner product (i.e. cross-correlation) of each possible combination of source points in this region was calculated, resulting in over 166 million separations and cross-correlations. Fig. 4.11 is a histogram normalized such that the integral of each vertical slice equals one (and is thus a PDF for a given separation).

We can see that as point sources increase in separation, the probability of the cross-correlation being very low increases significantly. At a separation of 6λ , the probability of an cross-correlation being below 0.1 is nearly 1.0. Conversely, when the separation is less than 0.5λ , the probability of the cross correlation being above 0.8 is nearly 1.0. Essentially, this indicates that a minimum point source separation of somewhere between 0.75λ and 2λ would

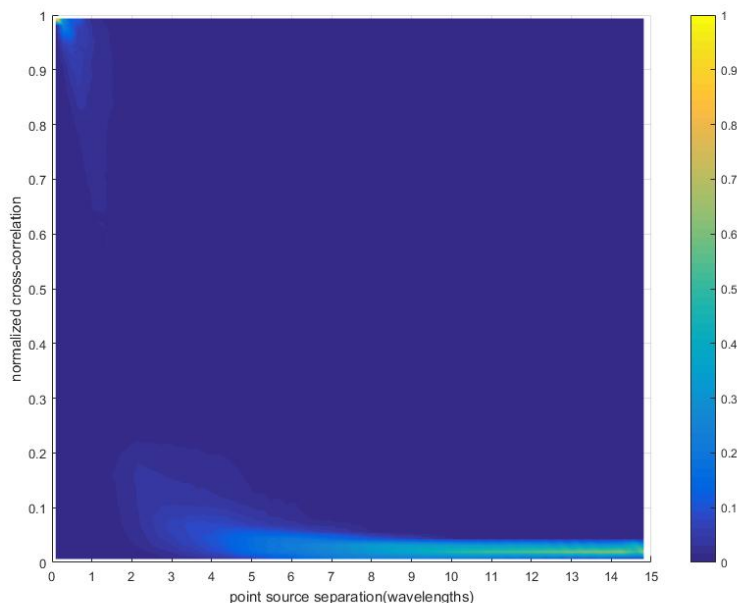


Figure 4.11: Normalized Histogram of Cross-Correlation Vs. Separation

be sufficient to increase the probability of a low cross-correlation to be significant enough to investigate. Setting a minimum separation too high may exclude valid candidate points that would increase the accuracy of the model, while setting the minimum separation too low would increase the number of points excluded due to the inner-product being above a set threshold, and therefore the computational time of the algorithm searching for new points that meet this threshold requirement.

Significant testing of manual adjustment of the minimum separation and cross-correlation threshold with measured channel data yielded a minimum separation of 0.75λ and cross-correlation threshold of 0.08, which allowed the multiple point source correlation algorithm to run with sufficiently-small error and reasonable run time. More detail on the channel measurements used for this process will be discussed in the following chapter.

4.2.5 Use of Point Source and Plane Waves as Joint Spatial Attribute Functions

Plane waves and waves from a point source are related. Using the concept of Eikonal surfaces, plane waves contain planar Eikonal surfaces separated by a wavelength λ , and have constant amplitude over space. At a large observation distance, over a relatively small observation region, the local Eikonal surfaces of a point source are approximately planar due to a small spherical sector solid angle and large spherical sector radius $\|\vec{r} - \vec{r}_0\|$. Also, the relative change in radius, δ , from the point source over the distant observation region is small relative to the radius from the point source (i.e. $\|\vec{r} - \vec{r}_0\| \gg \delta$), and therefore the point source coefficients $\frac{1}{4\pi\|\vec{r} - \vec{r}_0\|} \approx \frac{1}{4\pi(\|\vec{r} - \vec{r}_0\| + \delta)}$, yielding a nearly-constant amplitude across the observation zone. As a result, in a small observation region distant from a point source, the planar Eikonal surfaces and constant amplitude indicate that a distant point source is approximately a plane wave. Therefore, a joint usage of close point sources and plane waves is essentially equivalent to using purely point sources (with some close and some very distant) to model the channel. However, even though these spatial attribute functions are essentially the same, we can utilize the special shape properties of Eikonal surfaces of near point sources and the Fourier properties of plane waves to fit each to a data set in an observation region and generate a model.

4.3 Fitting of Spatial Attribute Functions to Numerical Channel

The third contribution of this chapter is presented in this section, as noted in the third column of Fig. 4.1. The methods of phase correlation maximization as outlined in Sec. 4.2.3

and spatial spectral decomposition as outlined in Sec. 4.2.1 are combined into a procedure to model the channel. The following procedure is performed on data sampled in an observation region that meet the previously-outlined spatial Nyquist sampling requirements.

This method can be utilized to reduce the total number of components (plane wave plus point sources) required to model a signal (or in this case a channel) when compared to a pure sum-of-plane waves model, thus reducing model complexity.

4.3.1 Point Source Fitting

The first part of the procedure involved determining point sources and corresponding complex weights of the sampled channel. This utilizes methods discussed in Sec. Sec. 4.2.3.

1. Collect the sampled channel data $H(\tilde{\mathbf{r}})$ at all measurement points $\tilde{\mathbf{r}}$ in the observation region for a single wavelength λ .
2. Define a search region for point sources \vec{r}_0 for the correlation maximization algorithm.
3. Define minimum point source separation constraint 0.75λ and maximum inner-product for point source pairs (0.08).
4. Run a global optimization routine on $\hat{\vec{r}}_{0_1} = \arg \max_{\vec{r}_{0_1} | \vec{r}_{0_1z} > r_z} | \sum_{i=1}^N H(\vec{r}_i) e^{jk||\vec{r}_i - \vec{r}_{0_1}||} |$ to determine an initial point source $\hat{\vec{r}}_{0_1}$.
5. Calculate the contribution of the point source $\hat{\vec{r}}_{0_1}$ at each observation location $\tilde{\mathbf{r}}$: $E_{PS_1}(\tilde{\mathbf{r}})$.
6. Use least squares to calculate the complex weight β_1 of the point source that best fits the sampled channel data and minimizes the residual $\vec{\varepsilon}_1(\tilde{\mathbf{r}})$, $H(\tilde{\mathbf{r}}) = \beta_1 E_{PS_1}(\tilde{\mathbf{r}}) + \vec{\varepsilon}_1(\tilde{\mathbf{r}})$.
7. Calculate the residual $\varepsilon_1(\tilde{\mathbf{r}})$ after the least squares fit.

8. Repeat steps 4 through 7 using $\vec{\varepsilon}_1(\tilde{\mathbf{r}})$ instead of $H(\tilde{\mathbf{r}})$, with the optimization in step 4 subject to the constraints defined in step 3, to calculate \hat{r}_{0_2} , $E_{PS_2}(\tilde{\mathbf{r}})$, β_2 , and $\vec{\varepsilon}_2(\tilde{\mathbf{r}})$.
9. Repeat step 8 using $\vec{\varepsilon}_2(\tilde{\mathbf{r}})$ instead of $\vec{\varepsilon}_1(\tilde{\mathbf{r}})$, then $\vec{\varepsilon}_3(\tilde{\mathbf{r}})$ instead of $\vec{\varepsilon}_2(\tilde{\mathbf{r}})$, to calculate as many point sources \hat{r}_{0_n} and complex weights β_n as needed, either an arbitrary number or until a point source is under a defined correlation threshold. The final residual $\vec{\varepsilon}_n(\tilde{\mathbf{r}})$ will be used for refinement with plane waves.

4.3.2 Refinement Using Plane Waves

The residual from the point source fitting, $\vec{\varepsilon}_n(\tilde{\mathbf{r}})$, is then modeled with plane waves iteratively until a desired accuracy is reached.

1. Using the residual $\vec{\varepsilon}_n(\tilde{\mathbf{r}})$ over all measurement points $\tilde{\mathbf{r}}$ in the observation region for a single wavelength λ , apply a 2-dimensional Hanning window and zero pad the data in both X and Y directions until the desired DFT frequency resolution is obtained.
2. Perform a 2-dimensional DFT on the data from step 1. Calculate the wave vectors for each point in the frequency domain.
3. Find the wave vector \vec{k}_1 corresponding to the maximum of the DFT output. This is the wave vector of the first plane wave to be fit.
4. Calculate the contribution of the plane wave $E_{PW_1}(\tilde{\mathbf{r}}) = e^{-j\vec{k}_1 \cdot \tilde{\mathbf{r}}}$ at each observation point $\tilde{\mathbf{r}}$.
5. Perform a least squares fit of the plane wave to the point source residual $\vec{\varepsilon}_n(\tilde{\mathbf{r}})$ to find the value β_{PW_1} that minimizes the plane wave residual $\vec{\varepsilon}_{PW_1}(\tilde{\mathbf{r}})$ in the equation:

$$\vec{\varepsilon}_n(\tilde{\mathbf{r}}) = \beta_{PW_1} E_{PW_1}(\tilde{\mathbf{r}}) + \vec{\varepsilon}_{PW_1}(\tilde{\mathbf{r}}).$$

6. Determine the residual $\vec{\varepsilon}_{PW_1}(\tilde{\mathbf{r}})$ after the least squares fit.
7. Perform steps 1 through 6 using $\vec{\varepsilon}_{PW_1}(\tilde{\mathbf{r}})$ instead of $\vec{\varepsilon}_n(\tilde{\mathbf{r}})$ to find β_{PW_2} and $\vec{\varepsilon}_{PW_2}(\tilde{\mathbf{r}})$.
8. Repeat step 7 replacing the previous residual with the new residual each time to calculate β_{PW_n} and $\vec{\varepsilon}_{PW_n}(\tilde{\mathbf{r}})$.
9. Stop this procedure when the mean Error Vector Magnitude (EVM), the mean magnitude of the residual, is below a defined threshold.

4.4 Validation of Spatial Attribute Function Selection with Numerical Channel

The algorithm defined in the Sections of 4.3 was performed on the numerical dipole array channel developed in Sec. 4.1.3. The mean and standard deviation of the Error Vector Magnitude (EVM) of different combinations of point sources and plane waves to determine the effect of each type of (and number of each) spatial attribute function on the accuracy of the model. Models consisting of only point sources and only plane waves were also calculated using just the appropriate half of the algorithm in the previous section. Finally, the value of mean plus 1 standard deviation of the EVM of each case is observed, indicating that approximately 84 percent (50 percent plus one σ) of EVM from the model over the observation area is below the stated value.

Figure 4.12 is a plot of the LogNormal mean EVM for between 0 and 3 point sources (spherical components) and 0 and 5 plane waves (planar components). For 0 point sources and 0 plane waves, the error is 0 dB, or 100 percent error, by definition (nothing modeled). A model consisting of a single point source and no plane waves provides an EVM of -18.3

dB, meaning that on the average, the error signal contains 1.5 percent of the power of the channel being modeled. A single plane wave without any point sources, on the other hand, has an EVM of -8.2 dB. Four plane waves are required to achieve an EVM less than a single point source. This indicates that a point source is an excellent initial choice of a spatial attribute function!

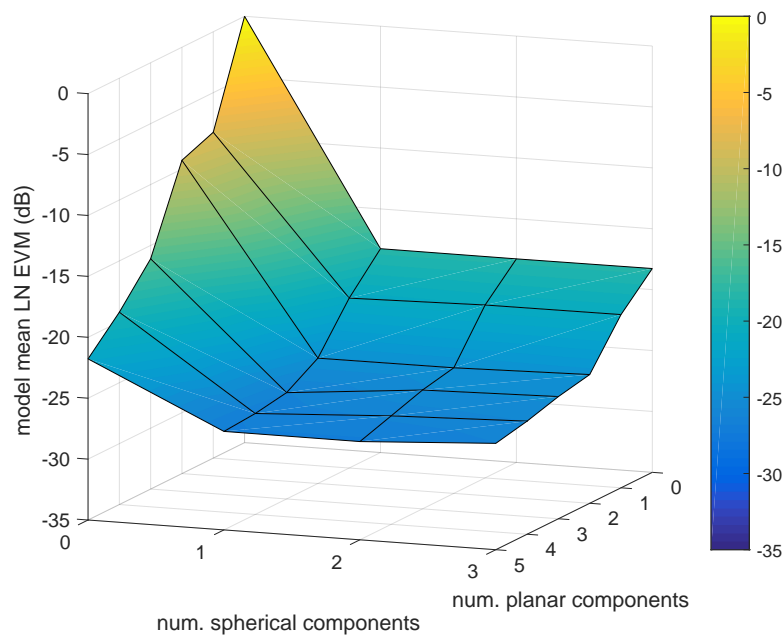


Figure 4.12: LogNormal Mean EVM For Combinations of Spatial Attribute Functions

As expected, additional point sources do not decrease the EVM by a significant amount. The point sources are modeling free-space radiation from a relatively small antenna array. The minimum separation constraint for subsequent point sources after the first is at least 0.75λ , putting the second or third point source in a region away from the antenna for which the channel is being modeled. As a result, the second and third point sources had very low maximum correlations, and had very low magnitude coefficients when fit to the residual

data. As a result, they had extremely low contribution to the model, and while they do no harm to the model, these point sources can be excluded. It should be noted that the system being modeled in this case is free-space and involves no reflections; additional point sources will be useful in modeling source reflections, as will be seen in the following chapter.

Finally, we observe combinations of point sources and plane waves, as the plane waves serve to refine the point source model. With one point source and two plane waves, a mean EVM of -24.7 dB is achieved. One point source and 5 plane waves achieves a -26.9 dB EVM. As the number of plane waves increases, the advantage of the point source component of the model is still present, though its benefit decreases. The clear benefit of a joint point source and plane wave model is in models with a relatively low number of terms, and produces significantly lower EVM than a comparable number of plane waves alone.

In terms of standard deviation, models of only a couple plane waves have a standard deviation of between 1.5 dB and 2 dB, models of only point sources have about 2 dB standard deviation, and combinations have between 2 dB and 2.5 dB. This is illustrated in Fig. 4.13.

In Fig. 4.14, we observe mean plus σ , meaning that 84 percent of modeled locations are as accurate as the value in this plot. Because the standard deviations were relatively constant between 1.5 and 2.5, very little changes in terms of the advantage of point sources and combinations over plane waves alone, though the gap closes a small amount. Even a single point source still has 84 percent of EVM below -16.3 dB.

In short, the low EVM for a relatively low number of spatial attribute functions indicates that point sources, and joint point sources and plane waves are validated as an effective way of modeling the synthetic numerical dipole array channel with an acceptable accuracy of between -15dB and -20dB or better. This modeling algorithm will be applied to real channel measurements in the following chapter.

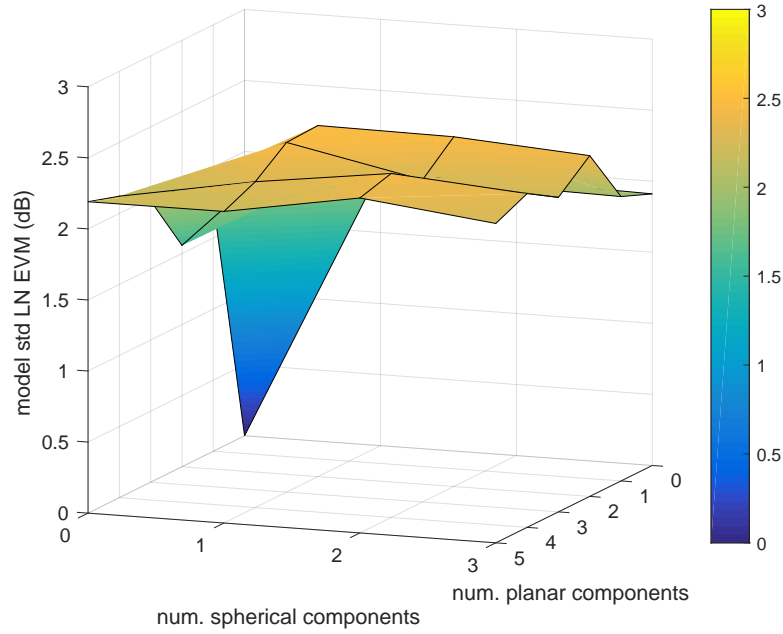


Figure 4.13: Standard Deviation of EVM For Combinations of Spatial Attribute Functions

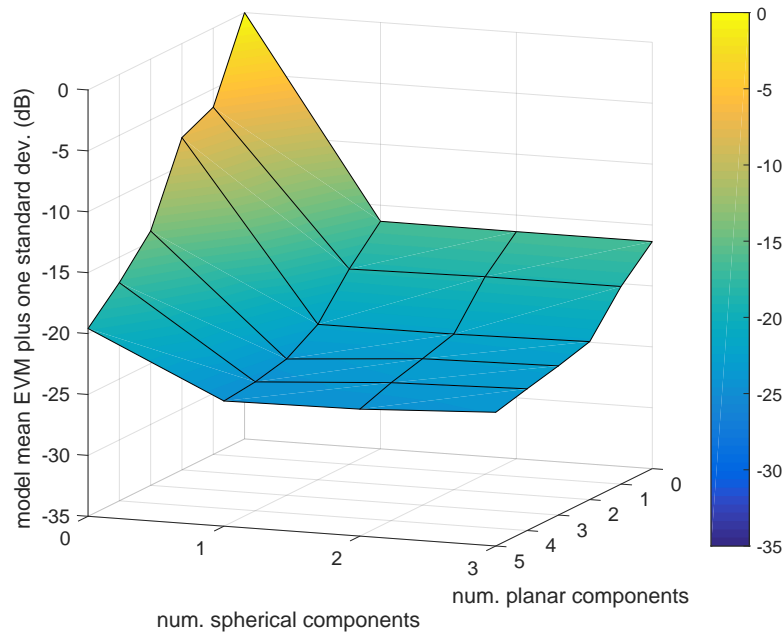


Figure 4.14: LogNormal Mean + 1 SD EVM For Combinations of Spatial Attribute Functions

4.5 Conclusions

The channel modeling algorithm presented in this chapter has been validated to produce acceptable error for a small number of spatial attribute functions, and therefore is effective as a modeling tool for relatively simple, accurate description of the channel between a log-periodic array and a dipole antenna. Given the principles outlined in this chapter, it could in theory be adapted to other antenna types and environments for investigation and modeling of other channels, both real and synthetic. In addition, additional variables could be added to the model, such as transmitter antenna position and orientation, and receiver orientation and/or vertical position. A combination of point source and plane waves would still be sufficient for description of such channels, however the number of each type of basis function will vary depending on the environment, including receiver observation zone size, distance between transmitter and receiver, number of reflections and the power of each reflection, and physical size of transmitter and receiver arrays. The next chapter will investigate a real, non-free-space system in which added factors such as reflections will be introduced.

CHAPTER 5

Statistical and Frequency Extensions of Near-Field Channel Model

The purpose of this chapter is extend the mathematical framework derived in the previous chapter to incorporate statistical information from the spatial attribute function residual, as well as extend the model as a function of frequency. This produces a model that has improved EVM over the spatial attribute function fitting method alone, and is broadband. In addition, this chapter utilizes channel measurements taken inside a small anechoic test chamber between log-periodic probe antennas in four locations and a receiver dipole antenna placed along a grid to sample the channel space. The models for each probe antenna resulting from this measurement campaign can therefore be combined to calculate a MIMO channel between the probes and an arbitrarily-positioned receiver dipole array. The MIMO analysis of this channel model will be performed in the next chapter.

Fig. 5.1 shows the breakdown of contributions in chapters 4 and 5. The contributions for Chapter 5 are emphasized in bold.

The first contribution of this chapter is to improve the accuracy and EVM of the channel model presented in the previous chapter utilizing statistical information from the residual of the fitted spatial attribute functions. This is achieved by applying methods of Geostatistical Regression [56] [52] and Complex Geostatistical Kriging [57], methods taken from the field of Geostatistics (so-called due to its original application to Geology and mining). This field of analysis focuses on statistical properties of random signals in space (or space and time),

CHAPTER 5. STATISTICAL AND FREQUENCY EXTENSIONS OF NEAR-FIELD CHANNEL MODEL

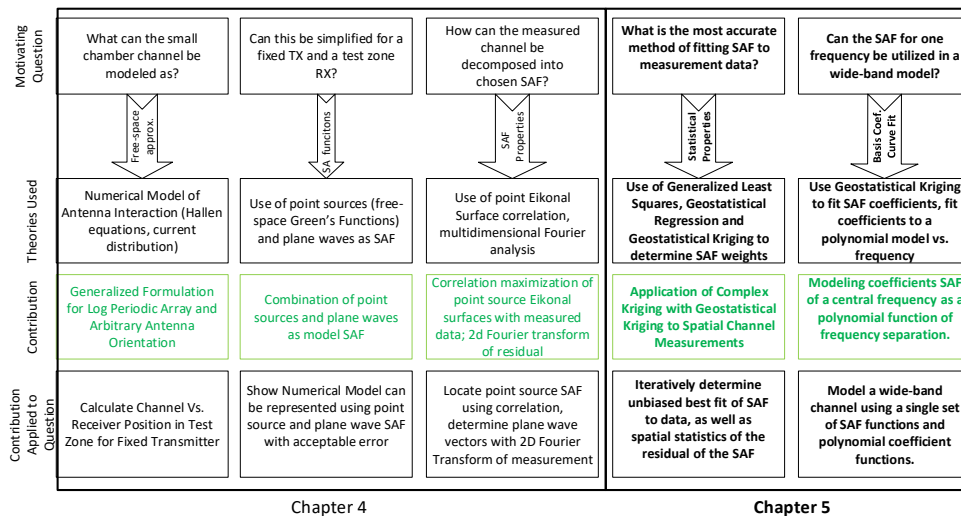


Figure 5.1: Chapter 5 Contribution Flowchart

and the use of these statistics in conjunction with spatial measurements to estimate the signal at any location. This application is new and novel, as no application of this field to spatial channel modeling has been found in the literature. In addition, no use of Complex Geostatistical Kriging in conjunction with the iterative process of Geostatistical Regression has been located in the literature.

The second contribution of this chapter is extending our narrow-band model, which determines spatial attribute functions, complex weights, statistics, etc. at a single frequency, to a broadband model as a function of frequency. Using a common set of frequency-scaled spatial attribute functions, complex weights for each are determined over a wide range of frequencies, and a polynomial regression is performed to determine a function for each weight as a function of frequency. This extends our novel Geostatistical channel model to a Wideband Geostatistical channel model.

Sec. 5.1 outlines the methods of Geostatistical Regression and Complex Geostatistical

Kriging, and combines the two into a complex iterative Geostatistical Regression algorithm for spatial attribute function determination. Sec. 5.2 presents a method of adapting spatial attribute functions over a wide frequency band, and modeling the complex function coefficients as a function of frequency, yielding a Wideband Geostatistical model. Sec. 5.3 describes the system being modeled in detail, while Sec. 5.4 explains the measurement campaign performed on that system. Sec. 5.5 applies the Wideband Geostatistical modeling process on the measurement data to produce a model for the measured system.

5.1 Accurate Method of Fitting Spatial Attribute Functions to Measured Data

The method of ordinary least squares (OLS), utilized in the previous chapter for fitting each spatial attribute component to the sampled channel (or subsequently the residual of the sampled channel after each fitted spatial attribute function (SAF) is subtracted), can be used to simultaneously estimate the complex coefficients of each SAF. The system can be modeled with a matrix \mathbf{X} , where each column is a spatial attribute function, and each row is a channel sample location (in other words, each element is the value of an unweighted spatial attribute function evaluated at a sample location). In addition to the spatial attribute functions, an additional column is added to the matrix consisting of a unit constant, which will correspond to a complex additive constant (an extra value to be determined in the vector of complex weights to be estimated) to force a zero-mean residual. \mathbf{X} is multiplied by a column vector of complex weights for each spatial attribute function, $\vec{\beta}$, which can be calculated to minimize the residual $\vec{\varepsilon}$ when subtracted from the vector of sampled data at each sample location, \vec{y} . This system can be expressed as:

$$\vec{y} = \mathbf{X}\vec{\beta} + \vec{\varepsilon} \quad (5.1)$$

The residual $\vec{\varepsilon}$ is assumed to be normally-distributed with variance σ^2 and zero mean. The OLS solution of this equation that minimizes the sum of the residual $\sum \vec{\varepsilon}$ is (5.2), the pseudoinverse of \mathbf{X} times the sampled data \vec{y} .

$$\vec{\beta}' = (\mathbf{X}^H \mathbf{X})^{-1} \mathbf{X}^H \vec{y} \quad (5.2)$$

where H is the Hermetian transpose, and $'$ represents the estimation of a variable, two notation conventions used through this chapter. This assumes that the Gram matrix, $\mathbf{X}^H \mathbf{X}$, is non-singular. In the previous chapter, special care was taken to select SAF that yielded a non-singular Gram matrix.

It should be noted that OLS is only appropriate for a classical regression model, which assumes that the elements of the residual $\vec{\varepsilon}$ are statistically independent [52], thus $\text{cov } \varepsilon = \sigma^2 \mathbf{I}_n$, where σ^2 is the residual variance, \mathbf{I}_n is the $N \times N$ identity matrix (where N is the length of $\vec{\varepsilon}$). This means that the residual is unrelated at two separate locations in space, even if the separation of those locations is extremely small. This assumption is not necessarily true, and spatial correlation of the residual as a function of separation must be investigated, and if present, taken into account in the regression process.

5.1.1 Generalized Least Squares

When the correlation matrix \mathbf{C} of the residual is known *a priori*, if non-diagonal elements are non-zero, then the residual ε is no longer considered spatially-independent. Through the use of a decomposition of the \mathbf{C} matrix into a Cholesky matrix \mathbf{T} and its transpose,

$\mathbf{C} = \mathbf{T}\mathbf{T}^H$, (5.1) can be pre-multiplied on both sides by the inverse of \mathbf{T} to transform the equation to one in which the transformed residual term has statistically-independent entries [52]. This residual independence yields a transformed equation (5.3) in which β' can be solved using OLS.

$$\vec{\beta}' = ((\mathbf{T}^{-1}\mathbf{X})^H(\mathbf{T}^{-1}\mathbf{X}))^{-1}(\mathbf{T}^{-1}\mathbf{X})^H(\mathbf{T}^{-1}\vec{y}) \quad (5.3)$$

Through manipulation and reverse substitution of the Cholesky decomposition [52], the estimation of β' (known as Generalized Least Squares (GLS) regression) is expressed in terms of the correlation matrix \mathbf{C} in (5.4).

$$\vec{\beta}' = (\mathbf{X}^H\mathbf{C}^{-1}\mathbf{X})^{-1}\mathbf{X}^H\mathbf{C}^{-1}\vec{y} \quad (5.4)$$

This estimate of $\vec{\beta}'$ once again requires \mathbf{C} to be known *a priori*. In most applications, however, both the complex weights $\vec{\beta}'$ of the SLA and a model of the correlation of the residual \mathbf{C}' (and associated model parameters) must be simultaneously estimated. This simultaneous estimate can be performed using an iterative algorithm called Geostatistical Regression [56] [52], outlined in Section 5.1.4. First, a method of modeling the spatial cross-correlation of the residual must be established.

5.1.2 Covariograms and Spatial Dependence

A statistical analysis and covariance (and correlation) model of the residual data $\vec{\varepsilon}$ must be performed for use in the iterative Geostatistical Regression process. A useful method to model spatial dependencies is the variogram (and covariogram). In a covariogram $C(h)$, the covariance of two processes at two points in space ($\text{cov}(\varepsilon(\vec{x}_1), \varepsilon(\vec{x}_2))$) is a function of the

separation of the two points in space alone ($h = \|\vec{x}_1 - \vec{x}_2\|$), independent of where the points are [52].

A convenient way to calculate and express the manner in which two processes are expected to differ in space is to observe the expected squared difference of the residual $E[\varepsilon(\vec{x}_1) - \varepsilon(\vec{x}_2)]^2$ [52]. Through expansion and manipulation, the definition of the covariogram can be utilized, and the expected squared residual difference becomes $2[C(0) - C(h)]$. Normalizing this by a factor of a half, the variogram can be defined as $\gamma(h) = C(0) - C(h)$. Finally, using $C(0) = \sigma^2$, the relation between the variogram and covariogram becomes $C(h) = \sigma^2 - \gamma(h)$.

Residual data can be used to construct an empirical covariogram using the following procedure [52].

1. For a set of residual data $\vec{\varepsilon}$, calculate the squared difference of each and every pair of residual data and the separation h between the points at which the residual is sampled.
2. Divide the span of calculated separations h into evenly-spaced bins from 0 to h_{max} .
3. Group the squared difference data into respective bins based on their corresponding separation h
4. Calculate the mean squared difference for each bin (thus estimating the expected squared difference for each h bin).

The resulting bin mean values versus bin h (normalized by one half) form the empirical variogram. It should be noted that bin size and maximum separation h_{max} should be chosen such that each bin contains at least 30 points [52]. This is a general rule of thumb, and is applied to assure a sufficient number of points such that their average approaches the expected value.

The empirical covariogram can be analyzed to choose an appropriate covariogram model. The empirical covariogram can then be fit to a candidate model using OLS, or each bin can be weighted such that data from bins with more points have a greater weight than data from bins with fewer points (a process known as weighted least squares).

Two issues arise from this procedure as it applies to channel modeling. First, the variogram is defined only in terms of point separation h , which means that the variogram is independent of direction of separation. This indicates that the underlying covariogram is assumed to be isotropic. If the empirical variogram is calculated with bins in two dimensions (thus in terms of separate x and y separation distances), the variogram can be inspected for anisotropic behavior. This will likely exhibit as an ellipse with a major and minor axis and a rotation. Correctional rotation and directional scaling can be applied to the empirical variogram data to create an equivalent isotropic model. Chapter 2 contains additional information on isotropy in variograms.

Second, and perhaps most importantly, the variogram models discussed in [56] and [52] all utilize real-valued data, producing a positive definite variogram. The residual of the channel model being developed will be complex-valued. While the general concepts and procedure remain as described, complex candidate models and empirical variogram methods must be utilized to apply these methods to a complex channel model.

5.1.3 Complex Geostatistical Covariance Model

Both issues of complex covariance modeling and anisotropy have been addressed by De Iaco and Posa [57]. The following is a summary of the method extracted from this paper for use in the iterative Geostatistical Regression procedure in the following section.

For complex random fields, the complex covariance is defined as:

$$C(\vec{h}) = E[(Z(\vec{x}_1) - \mu)\overline{(Z(\vec{x}_1 + \vec{h}) - \mu)}] \quad (5.5)$$

where $Z(\vec{x}) = X(\vec{x}) + iY(\vec{x})$ is the complex field at position \vec{x} , μ is the mean of Z (which is equal to zero in the context of our residual field), and \vec{h} is the separation vector (which it should be noted accounts for separation distance and direction). The covariance function can be written in terms of two functions, one for the real part and one for the imaginary part (5.6), the real part is the sum of the autocovariance of X and autocovariance of Y , and the imaginary part is the difference of the cross-covariance of Y and X , and cross-covariance of Y and X [57].

$$C(\vec{h}) = C^{re}(\vec{h}) + iC^{im}(\vec{h}) = (C_X(\vec{h}) + C_Y(\vec{h})) + i(C_{YX}(\vec{h}) - C_{XY}(\vec{h})) \quad (5.6)$$

The imaginary part of this complex function is not a covariance function, which means an alternate form for expressing a complex covariance must be determined. An admissible covariance model is [57]:

$$C(\vec{h}; \vec{c}, \vec{\theta}) = \cos(\vec{h} \cdot \vec{c})\tilde{C}(\vec{h}; \vec{\theta}) + i \sin(\vec{h} \cdot \vec{c})\tilde{C}(\vec{h}; \vec{\theta}) \quad (5.7)$$

where \vec{h} is a separation vector, \vec{c} is a translation vector that relates the real and imaginary cross-covariances, and $\vec{\theta}$ is a parameter vector for a selected real covariance function \tilde{C} . The real covariance function will be selected after inspection of the empirical covariance and variogram.

With preliminary variables and equations established, the following procedure from [57] was followed:

1. Calculate auto-covariance and cross-covariance for the real and imaginary parts of each and every pair of residual signal $\vec{\varepsilon}'$, and calculate the separation vector \vec{h} for each pair.
2. Divide the 2-dimensional separation vector space into separation vector bins, and calculate the mean $C_X(\vec{h}_i)$, $C_Y(\vec{h}_i)$, $C_{YX}(\vec{h}_i)$, and $C_{XY}(\vec{h}_i)$ for each bin. Calculate $C^{re}(\vec{h}_i)$ and $C^{im}(\vec{h}_i)$ for each bin \vec{h}_i . Observe the behavior of C_{re} and C_{im} versus \vec{h}_i to select a $\tilde{C}(\vec{h}_i; \vec{\theta})$ which follows the trends of the observed functions.
3. In both [57] and for this procedure, a Gaussian covariance model was selected for $\tilde{C}(\vec{h}; \vec{\theta})$. The form of this model is in (5.8). The parameter vector $\vec{\theta}$ consists of the parameters $\sigma^2 = C(0)$, the angle corresponding to maximum range θ , maximum range a_θ , and minimum range a_ϕ (range in perpendicular direction to maximum range). In other words, $\vec{\theta} = (\sigma^2, \theta, a_\theta, a_\phi)$. With the exception of σ^2 , the elements of $\vec{\theta}$ define the anisotropy present in the observed covariance and compensate for it. Note that $\vec{h} = (h_1, h_2)$, the x and y separation components, in (5.8) and subsequent equations.

$$\tilde{C}(\vec{h}; (\theta, a_\theta, a_\phi)) = e^{-\left[\left(\frac{\cos(\theta)h_1 - \sin(\theta)h_2}{a_\phi} \right)^2 + \left(\frac{\sin(\theta)h_1 + \cos(\theta)h_2}{a_\theta} \right)^2 \right]} \quad (5.8)$$

This equation, in conjunction with (5.7), produces the complex covariance model in (5.9).

$$C(\vec{h}; \vec{c}, \vec{\theta}) = \sigma^2 \left[\cos(\vec{h} \cdot \vec{c}) \tilde{C}(\vec{h}; (\theta, a_\theta, a_\phi)) + i \sin(\vec{h} \cdot \vec{c}) \tilde{C}(\vec{h}; (\theta, a_\theta, a_\phi)) \right] \quad (5.9)$$

4. Let N_i equal the number of bins \vec{h}_i . The translation vector \vec{c} can be estimated through OLS using $C^{re}(\vec{h}_i)$ and $C^{im}(\vec{h}_i)$ in conjunction with (5.7). The resulting equation for

estimating \vec{c} is (5.10).

$$\vec{c} = \begin{bmatrix} \sum_{i=1}^{N_l} h_{1,i}^2 & \sum_{i=1}^{N_l} h_{1,i}h_{2,i} \\ \sum_{i=1}^{N_l} h_{1,i}h_{2,i} & \sum_{i=1}^{N_l} h_{2,i}^2 \end{bmatrix}^{-1} \begin{bmatrix} \sum_{i=1}^{N_l} \arctan\left(\frac{C^{im}(\vec{h}_i)}{C^{re}(\vec{h}_i)}\right)h_{1,i} \\ \sum_{i=1}^{N_l} \arctan\left(\frac{C^{im}(\vec{h}_i)}{C^{re}(\vec{h}_i)}\right)h_{2,i} \end{bmatrix} \quad (5.10)$$

5. Use an optimization routine (non-linear least squares or other) to find the parameter vector $\vec{\theta}$ that minimizes the sum

$$\vec{\theta} = \arg \min_{\vec{\theta}} \sum_{i=1}^{N_l} [(C^{re}(\vec{h}_i) - \sigma^2 \cos(\vec{h}_i \cdot \vec{c})\tilde{C}(\vec{h}_i; \vec{\theta}))^2 + (C^{im}(\vec{h}_i) - \sigma^2 \sin(\vec{h}_i \cdot \vec{c})\tilde{C}(\vec{h}_i; \vec{\theta}))^2] \quad (5.11)$$

6. Using $\vec{\theta}$ and \vec{c} in conjunction with (5.9), we now have a complex covariance model $C(\vec{h}; \vec{c}, \vec{\theta})$.

With this complex covariance model, a full covariance matrix \mathbf{V} can be calculated. If N_l measurement locations (corresponding to the number of elements in the sample vector y), then \mathbf{V} is an $N_l \times N_l$ matrix, with element $V_{i,j} = C(\vec{x}_i - \vec{x}_j) = C(h_{i,j}; \vec{c}, \vec{\theta})$. The full covariance matrix \mathbf{V} is related to the correlation matrix \mathbf{C} by a factor of the variance ($\mathbf{V} = \sigma^2\mathbf{C}$) [52]. Because of this relationship, the GLS estimation of $\vec{\beta}'$ (5.4) can be rewritten in terms of the full covariance matrix instead of the correlation matrix (5.12).

$$\vec{\beta}' = (\mathbf{X}^H \mathbf{V}^{-1} \mathbf{X})^{-1} \mathbf{X}^H \mathbf{V}^{-1} \vec{y} \quad (5.12)$$

This GLS equation utilizing a full covariance matrix determined from the complex covariance model produces a better estimate of $\vec{\beta}'$. This better estimate of $\vec{\beta}'$ in turn is applied to (5.1), which then yields a new residual vector. The new residual vector can be used to

revise the covariance model, and so forth. This directly leads to an iterative refinement of estimated parameters $\vec{\beta}'$, \vec{c}' , and $\vec{\theta}'$, which is presented in the following section.

5.1.4 Geostatistical Regression

Previous work shows a method for iteratively estimating $\vec{\beta}'$ and spherical variogram parameters $\vec{\theta}'$ for real-valued random processes [52]. This procedure is adapted here (with general progression of the algorithm closely following the source) for a complex Gaussian covariogram as developed in the previous section, to iteratively estimate $\vec{\beta}'$, covariogram parameters $\vec{\theta}'$, and translation vector \vec{c}' for a complex random process.

1. Use the procedure from the previous chapter to determine a set of plane wave and point source spatial attribute functions (SAF), and evaluate these functions at all measurement locations at which the measurement y was taken, thus forming a spatial attribute matrix \mathbf{X} . As before, the rows of \mathbf{X} correspond to each sample location, and each column in \mathbf{X} corresponds to a spatial attribute function. An extra row consisting of a unit-magnitude constant (identical for all rows) is added to force the resultant residual to be zero-mean.
2. For the system $\vec{y} = \mathbf{X}\vec{\beta} + \vec{\varepsilon}$ (where β are the complex coefficients of each SAF, and $\vec{\varepsilon}$ is the model residual), perform an initial OLS estimate of $\vec{\beta}'$ (5.13).

$$\vec{\beta}'_0 = (\mathbf{X}^H \mathbf{X})^{-1} \mathbf{X}^H \vec{y} \quad (5.13)$$

Calculate the corresponding residuals (5.14).

$$\vec{\varepsilon}'_0 = \vec{y} - \mathbf{X}\vec{\beta}'_0 \quad (5.14)$$

3. Use the residuals $\vec{\varepsilon}_0$ in conjunction with the procedure in Section 5.1.3 to estimate the empirical complex covariance parameters $C^{re}(\vec{h}_i)$ and $C^{im}(\vec{h}_i)$ for the separation vector space divided into bins \vec{h}_i .
4. Continue to use the procedure in Section 5.1.3 to fit the empirical complex covariance data to the complex Gaussian covariance model. The estimated parameters to fit the model to the data are the translation vector \vec{c}_0 , and the parameter vector $vec\theta'_0 = (\sigma_0'^2, \theta'_0, a'_{\theta_0}, a'_{\phi_0})$. The resulting model is $C'_0(\vec{h}; \vec{c}_0, \theta'_0)$.
5. Fill in the initial estimate of the full covariance matrix (5.15), where each row i , column j pair represents a pair of points x_i and x_j , with separation vector $h_{i,j} = x_j - x_i$. Index i correspond to the row number of spatial attribute matrix \mathbf{X} , which corresponds to the spatial attribute functions evaluated at point x_i .

$$\begin{aligned} \mathbf{V}'_0 &= \mathbf{V}'(\vec{c}_0, \theta'_0) \begin{bmatrix} C'_0(\vec{h}_{1,1}; \vec{c}_0, \theta'_0) & \cdots & C'_0(\vec{h}_{1,n}; \vec{c}_0, \theta'_0) \\ \vdots & \ddots & \vdots \\ C'_0(\vec{h}_{n,1}; \vec{c}_0, \theta'_0) & \cdots & C'_0(\vec{h}_{n,n}; \vec{c}_0, \theta'_0) \end{bmatrix} \\ &= \begin{bmatrix} \sigma_0'^2 & \cdots & C'_0(\vec{h}_{1,n}; \vec{c}_0, \theta'_0) \\ \vdots & \ddots & \vdots \\ C'_0(\vec{h}_{n,1}; \vec{c}_0, \theta'_0) & \cdots & \sigma_0'^2 \end{bmatrix} \end{aligned} \quad (5.15)$$

6. Utilize GLS in conjunction with \mathbf{V}'_0 as in (5.12) to estimate a new value of $\vec{\beta}'_1$ (5.16).

$$\vec{\beta}'_1 = (\mathbf{X}^H \mathbf{V}'_0^{-1} \mathbf{X})^{-1} \mathbf{X}^H \mathbf{V}'_0^{-1} \vec{y} \quad (5.16)$$

Calculate new residuals using the new value of β (5.17).

$$\vec{\varepsilon}'_1 = \vec{y} - \mathbf{X}\vec{\beta}'_1 \quad (5.17)$$

7. Perform Steps 3 and 4 with $\vec{\varepsilon}'_1$ instead of $\vec{\varepsilon}'_0$ to determine the translation vector \vec{c}'_1 , and the parameter vector $\vec{\theta}'_1 = (\sigma'^2_1, \theta'_1, a'_{\theta_1}, a'_{\phi_1})$.
8. Let k equal the current iteration number (if immediately following step 7, $k = 1$), and $k - 1$ is the previous iteration number (if immediately following step 7, $k - 1 = 0$). For each current and previous estimated parameter $((\vec{\beta}'_k, \vec{c}'_k, \sigma'^2_k, \theta'_k, a'_{\theta_k}, a'_{\phi_k}), (\vec{\beta}'_{k-1}, \vec{c}'_{k-1}, \sigma'^2_{k-1}, \theta'_{k-1}, a'_{\theta_{k-1}}, a'_{\phi_{k-1}}))$, calculate the magnitude fractional change of each parameter p' (where p' is any parameter from the list of parameters) from the previous iteration ($k - 1$) to the current iteration (k).

$$\Delta_{k_{p'}} = \left| \frac{p'_k - p'_{k-1}}{p'_{k-1}} \right| \quad (5.18)$$

If the parameter p' is a vector with n parameters (as with $\vec{\beta}'$ and \vec{c}'), then let $\Delta_{k_{\vec{p}'}}$ be the maximum fractional change between iterations of any element of the vector (5.19).

$$\Delta_{k_{\vec{p}'}} = \max \left[\left| \frac{p'_{j,k} - p'_{j,k-1}}{p'_{j,k-1}} \right| : j = 0, 1, \dots, n \right] \quad (5.19)$$

Finally, the maximum fractional change between iterations is (5.20).

$$\Delta_k = \max \left[\Delta_{k_{\vec{\beta}'}} , \Delta_{k_{\vec{c}'}} , \Delta_{k_{\sigma'^2}} , \Delta_{k_{\theta'}} , \Delta_{k_{a'_\phi}} , \Delta_{k_{a'_\theta}} \right] \quad (5.20)$$

9. Define a maximum fractional change threshold $\bar{\Delta}$ (for which the maximum fractional change calculated in the previous step must be under to terminate the algorithm). If the maximum fractional change is below or equal to this threshold ($\Delta_k \leq \bar{\Delta}$) for the current iteration k , then terminate the algorithm and the final estimated model parameters are $(\vec{\beta}', \vec{c}', \sigma^{2'}, \theta', a'_{\theta}, a'_{\phi}) = (\vec{\beta}'_k, \vec{c}'_k, \sigma^{2'}_k, \theta'_k, a'_{\theta_k}, a'_{\phi_k})$. If the maximum fractional change is above this threshold ($\Delta_k > \bar{\Delta}$), increment k by one and repeat Steps 5 through 8 until the maximum fractional change is below or equal to this threshold ($\Delta_k \leq \bar{\Delta}$) for the current iteration k , and extract the final estimated model parameters. In simple terms, the iterative algorithm will terminate when each and every parameter converges and changes by a sufficiently small amount between iterations.

5.1.5 Geostatistical Kriging

In the previous section, we iteratively estimated the Spatial Attribute Function (SAF) complex weights ($\vec{\beta}'$), translation vector (\vec{c}'), and residual statistical model parameter vector ($\vec{\theta}'$) from a series of channel measurements. With these channel model parameters in conjunction with the sampled channel measurements, we can implement a method of estimating the channel at any location in the sampled test area using a method known as Geostatistical Kriging [52]. In Geostatistical Kriging, for a location for which the channel is unknown and estimation is desired (x_0), the SAF can be evaluated at x_0 forming \vec{X}_0 (with capital X representing the Spatial Attribute Matrix and lowercase x representing a position in space) and weighted by the estimated coefficient vector $\vec{\beta}'$ determined in the previous section. Then, using the residual of nearby measurement locations in conjunction with the residual spatial covariance model, the residual at the unobserved point (ε'_0) can be estimated. The following procedure, once again closely following that of [52], details this procedure.

1. Determine a prediction set for the unobserved point x_0 . Only measurements spatially close to x_0 are significantly correlated with the residual at x_0 . Define a threshold h_0 beyond which measurement residuals will be excluded. This can be determined through inspection of the complex covariance function determined in the previous section. For all measurement locations x_i in the measurement set $\{x_n\}$, find a set $\{x\}$ which only includes measurements within a distance of h_0 of the unobserved point x_0 (5.21).

$$\{x\}(x_0) = \{x_i \in \{x_n\} : \|x_0 - x_i\| < h_0\} \quad (5.21)$$

2. Using the prediction set, create an estimate of the prediction covariance matrix for the unobserved point x_0 united with the prediction set $\{x\}$ (5.22). Let row/column one correspond to the unobserved point (and correspond to an index of 0), and all other rows and columns correspond to points in the prediction set (and correspond to an index of 1 through i). Populate a matrix \mathbf{V}' where $V'_{i,j} = C(h_{i,j}; \vec{c}, \vec{\theta}')$. Let \vec{v}' be defined as a row vector where element j is defined by $v_j = C(h_{0,j}; \vec{c}, \vec{\theta}')$, the covariance between point x_j in the prediction set and the unobserved point x_0 .

$$\mathbf{V}'_{prime} = \begin{bmatrix} \sigma^{2'} & \vec{v}'^H \\ \vec{v}' & \mathbf{V}' \end{bmatrix} \quad (5.22)$$

3. Estimate the residual ε'_0 at the unobserved point x_0 through simple Kriging of the residuals of the prediction set $\vec{\varepsilon}'$ (5.23).

$$\varepsilon'_0 = \vec{v}'^H \mathbf{V}'^{-1} \vec{\varepsilon}' \quad (5.23)$$

4. Use the spatial attribute matrix at the unobserved point \vec{X}_0 , complex spatial attribute weights $\vec{\beta}'$, and estimated residual at the unobserved point ε'_0 to estimate the channel at the unobserved point y'_0 (5.24).

$$y'_0 = \vec{X}_0 \vec{\beta}' + \varepsilon'_0 \quad (5.24)$$

5. Finally, this analysis can produce a prediction standard error (5.25).

$$\sigma'_0 = \sqrt{(\sigma^{2l} - \vec{v}_0^H \mathbf{V}'^{-1} \vec{v}_0) + (X_0 - X^H \mathbf{V}'^{-1} \vec{v}_0)^H (X^H \mathbf{V}'^{-1} X)^{-1} (X_0 - X^H \mathbf{V}'^{-1} \vec{v}_0)} \quad (5.25)$$

The process of choosing and fitting Spatial Attribute Functions to measured channel data, then iteratively refining the complex coefficients of these functions in conjunction with developing and iteratively refining a complex covariance model of the residual, results in a model that can be used in conjunction with channel measurements and the process of Kriging to mathematically model the channel at any location in the sampled observation zone. One limitation of this model is that analysis and modeling is performed at a single frequency. To be useful in a wideband system, this model must be extended to be applicable to a wide frequency band.

5.2 Adapting Spatial Attribute Function Set for a Wide-band Model

In the previous chapter, plane wave ($E_{PW}(\vec{\mathbf{r}}) = e^{-j\vec{k}\cdot\vec{r}}$) and point source ($E_{PS}(\vec{r}) = \frac{e^{-jk\|\vec{r}-\vec{r}_0\|}}{4\pi\|\vec{r}-\vec{r}_0\|}$) Spatial Attribute Functions (SAF) were selected for use in our channel model. Both types of function are complex exponentials, containing in the exponential a coefficient to the independent variable(s). In the case of plane waves, the dependent variable is a position vector \vec{r} , while in the case of point sources, the dependent variable is radial distance $r = \|\vec{r}-\vec{r}_0\|$. In the exponential, the coefficient to these dependent variable(s) is wavenumber $k = \frac{2\pi f}{c}$ for point sources, or wavevector $\vec{k} = \frac{2\pi f}{c}\hat{k}$, where f is frequency in Hz, c is the velocity of propagation (speed of light in free space), and \hat{k} is the unit wavevector.

For our narrowband model, which is based on free-space sampling of the channel at a specific frequency f_0 given a unit excitation of the system at the same frequency, the f term in the wavenumber or wavevector expression should be equal to f_0 . This should be true even in reflections of the waveforms from surfaces in the system. However, it should be noted that the 3D plane wave projections onto the X-Y plane that form the 2D plane wave SAF in our model will only contain the \hat{x} and \hat{y} components of \hat{k} . We would expect in 3D space, the wavevector would have the form $\vec{k} = \frac{2\pi f}{c}(k_x\hat{x} + k_y\hat{y} + k_z\hat{z})$, where k_x , k_y , and k_z are the x , y , and z components of the unit vector \hat{k} , with $\sqrt{k_x^2 + k_y^2 + k_z^2} = 1$. This would mean the unit vector of the projection would be $\hat{k}_{proj} = \frac{k_x}{\sqrt{k_x^2 + k_y^2}}\hat{x} + \frac{k_y}{\sqrt{k_x^2 + k_y^2}}\hat{y}$, and the wavevector coefficient would become $\frac{2\pi\sqrt{k_x^2 + k_y^2}f}{c}$. Therefore the apparent frequency of the 2D plane wave would be $\sqrt{k_x^2 + k_y^2}f$, and thus each 2D projected plane wave should contain a constant-scaled version of the excitation frequency f_0 . In short, in each SAF, we have a complex exponential with

f_0 or a constant-scaled version of f_0 in the exponent.

Channel measurements can be performed at a series of narrowly-spaced frequencies to observe the change in channel versus frequency. In the case of a closed, static, linear system consisting of materials that have a small change in properties relative to change in frequency, channel measurements at closely-spaced frequencies will also have a small change in magnitude. This is due to the fact that the geometric paths between transmitter and receiver will remain static independent of frequency, with variation only occurring in the reflection coefficients as a function of frequency in reflecting materials in the system. These variations are small in the system of interest, as the absorbing material properties are relatively constant in the frequency range of analysis.

Because channel signal paths are essentially constant with small frequency changes, it is logical that the resultant channel with a small frequency change is a frequency-shifted version of the underlying components (which are described by SAF), each with coefficients that change slightly as a function of frequency. Because the wavenumber or wavevector is proportional to the frequency of excitation and measurement ($k \propto f_0$), then at a shifted frequency af_0 , where a is a shifting constant of proportionality (with $a = 1$ representing no shift), a wavenumber or wavevector can also be scaled by a .

Using the idea of frequency-shifted SAF as discussed above, a logical extension is to determine the SAF at a single frequency f_0 using the method described in the previous chapter, then for a shifted frequency $f_1 = af_0$, re-calculate the spatial attribute functions at each and every measurement point with the exponent scaled by a , then re-estimate all SAF weights and other estimated parameters. The following section outlines this procedure in detail.

5.2.1 Algorithm for Fitting Spatial Attribute Function Set

The following is a procedure for using the SAF extracted from a single frequency to estimate model parameters over a wide frequency range.

1. Select an initial frequency f_0 corresponding to a frequency used to sample the channel over an observation region.
2. Utilize the procedure from the previous chapter to extract a set of plane wave and point source SAF for the frequency f_0 .
3. Use the procedure from the previous sections to iteratively estimate $(\vec{\beta}', \vec{c}', \sigma^{2'}, \theta', a'_{\theta}, a'_{\phi})$ at f_0 .
4. Select a set of frequencies $\{f_n\}$ near f_0 for which the channel was sampled over the same observation region.
5. For each f_n , determine the scaling constant $a_n = \frac{f_n}{f_0}$. Utilize a_n to scale the dependent term of the exponent of each SAF, and evaluate the SAF at each and every sample location in the observation region. Populate the spatial attribute matrix \mathbf{X}_n for f_n , using the scaled SAF evaluations, where each row of X represents a measurement location, and each column represents a SAF.
6. Utilize the procedure from the previous sections to iteratively estimate $(\vec{\beta}', \vec{c}', \sigma^{2'}, \theta', a'_{\theta}, a'_{\phi})$ at each and every f_n in $\{f_n\}$.
7. The end result is a set of each estimated parameter for a set of frequencies and for a single set of SAF.

This procedure yields each parameter at a corresponding set of frequencies. These parameters can be used to estimate the channel at each measurement point at each frequency, which can then be compared to the measured channel being modeled. The error vector magnitude (EVM) can be calculated at each sample point in the observation region, and a mean EVM can be determined for the model at each frequency. An EVM threshold can be established, and all frequencies with a mean EVM violating this threshold can be excluded from the model at the selected f_0 (and can be included in a model at a separate frequency and corresponding set of SAF).

Finally, The set of frequencies for which the model produces an acceptable EVM can be included in the following step, outlined in the next section.

5.2.2 Modeling Coefficients as Polynomial Functions of Frequency

Regression can be used to fit a polynomial to the parameter estimates. The previous section produced an estimate of each model parameter at each selected measurement frequency. Note that each parameter vector consists of multiple model parameters, each of which should be analyzed separately versus frequency. Additionally, many model parameters are complex-valued, which will not work with a polynomial fit. These should be modeled as two parameters each, one for magnitude, and one for phase angle. Magnitude and angle are each real values, and therefore can be modeled as a polynomial. For each parameter to be modeled, we fit a polynomial as a function of frequency using the set of estimated parameters and measurement frequencies.

Each parameter component estimation from the measurement is plotted versus measurement frequency. A polynomial order is selected to ensure the polynomial follows all significant trends in the component estimation versus frequency.

The complete list of parameters to be modeled using this polynomial method is $\vec{\beta}_{mag}(f)$
 $= (\beta_{0_{mag}}(f), \beta_{1_{mag}}(f), \dots, \beta_{n_{mag}}(f)), \vec{\beta}_{angle}(f) = (\beta_{0_{angle}}(f), \beta_{1_{angle}}(f), \dots, \beta_{n_{angle}}(f)), \vec{c}(f)$
 $= (c_1(f), c_2(f)), \vec{\theta}(f) = (\sigma^2(f), a_\phi(f), a_\theta(f), \theta(f)).$

5.2.3 Final Wideband Model Description

The final wideband model using the parameters as a function of frequency is an extension of (5.24) and (5.23), with \mathbf{V} and \vec{v}_0 expressed as functions of parameters utilized in their population. The channel estimate H' between the transmitter and a receiver at location \vec{x}_0 at frequency f_n is defined in the following equation (5.26),

$$H'(\vec{x}_0, f_n) = \vec{X}(\vec{x}_0, f_n) \vec{\beta}_{mag}(f_n) e^{j\vec{\beta}_{angle}(f_n)} + \vec{v}'_0(\vec{x}_0, \vec{c}(f_n), \vec{\theta}(f_n))^H \mathbf{V}'(\vec{x}_0, \vec{c}(f_n), \vec{\theta}(f_n))^{-1} \vec{\epsilon}' \quad (5.26)$$

where $\vec{X}(\vec{x}_0, f_n)$ is the spatial attribute vector, with each spatial attribute function evaluated at position \vec{x}_0 and frequency f_n , $\vec{\beta}_{mag}(f_n) e^{j\vec{\beta}_{angle}(f_n)}$ is the vector of complex SAF coefficients $\vec{\beta}$ evaluated at frequency f_n , $\vec{v}'_0(\vec{x}_0, \vec{c}(f_n), \vec{\theta}(f_n))$ is a vector of modeled covariances between admissible measurement points \vec{x}_i and location \vec{x}_0 with elements defined by $C(\vec{x}_i - \vec{x}_0; \vec{c}(f_n), \vec{\theta}(f_n))$, $\mathbf{V}'(\vec{x}_0, \vec{c}(f_n), \vec{\theta}(f_n))$ is a matrix of modeled covariances between each pair of admissible measurement points \vec{x}_i and \vec{x}_j with elements defined by $C(\vec{x}_j - \vec{x}_i; \vec{c}(f_n), \vec{\theta}(f_n))$, and $\vec{\epsilon}'$ is a vector of residuals at admissible measurement points \vec{x}_i at frequency f_n .

This modeling procedure is performed for as many subsections of the frequency range to be modeled as required to ensure that each modeled section is below a defined EVM threshold. Let the number of bands be defined as N_B . It also is performed for each individual transmit antenna of N_A transmit antennas. This method therefore requires $N_A \times N_B$ separate

models to define the channel for a wideband MIMO system of N_A transmitters by an arbitrary number of receivers in the observation zone, over N_B frequency bands. The remainder of this chapter is an experimental validation of this statistical wideband channel model using an extensive measurement campaign. The following chamber is an extension of this measurement-based model to MIMO system analysis.

5.3 System Description

The octoBox BOX-38 (Fig. 5.2) by Octoscope, Inc. is a semi-anechoic chamber for over the air (OTA) testing presents a system where the channel is quasi-nearfield due to close proximity of probe antennas (along upper-right side in the figure) and test zone in the center of the box. A line of sight (LOS) channel in free-space comparable to the channel between a log periodic probe antenna and a dipole located in the BOX-38 test zone region in the center of the chamber was simulated and modeled in the previous chapter with accurate results. It is therefore logical to utilize similar measurements from this chamber for performing and validating the channel model extension presented in this chapter.

5.3.1 Chamber Configuration and Properties

The octoBox BOX-38 is a small semi-anechoic chamber. The box acts as a Faraday cage, and its channel between probe antennas and DUT is shielded from signals exterior to the box. Isolation is rated at >80 dB when using cable connection filters. The box interior is lined with an absorbing material that attenuates reflections by approximately 20 dB for frequencies between 700 MHz and 6 GHz. Some elements including the metallic outlet cover on the back interior wall (not covered by absorbing foam) may produce first-order reflection components to the channel, but in general a dominant line of sight (LOS) signal path is

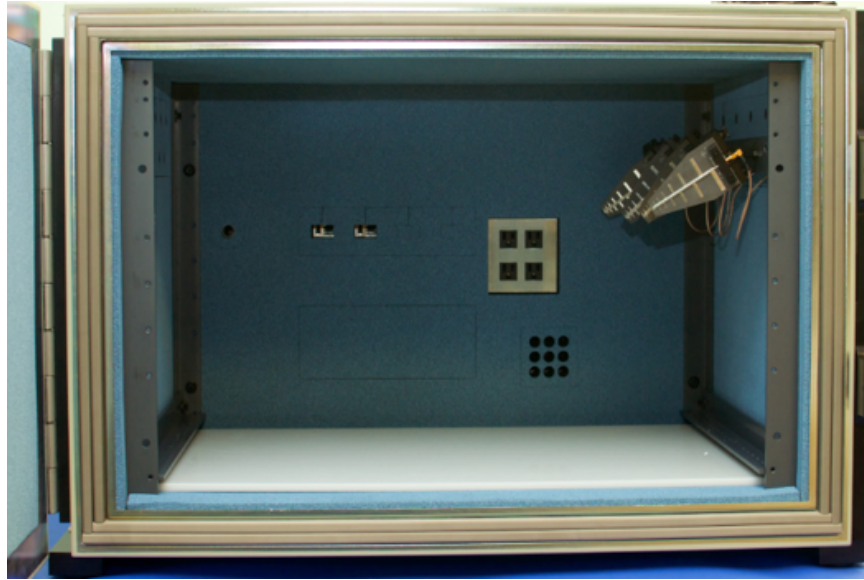


Figure 5.2: Octoscope octoBox BOX-38 Interior

expected.

A plastic frame in the interior allows for the placement of multiple probe antennas, typically either dipole or log periodic. These antennas are connected to SMA bulkheads underneath the absorbing foam, allowing for antenna excitation or connection to a transceiver. A power strip in the rear of the chamber allows filtered mains power to be supplied to a device under test (DUT) and/or a plastic turn table in the test zone of the chamber, allowing for rotation of the DUT orientation about the bottom center of the chamber. Finally, two filtered Ethernet ports are positioned along the rear of the chamber to allow for communication with the DUT and/or turntable control.

The interior dimensions of the chamber (in the open region excluding the absorbing foam within the chamber) are 0.49 m high, 0.81 m wide, and 0.55 m deep.

5.3.2 Antenna Properties

A set of four custom-designed Octoscope OBS-14 (Fig. 5.3) broadband high-gain log-periodic antennas are utilized as probe antennas in the small chamber. These are mounted on the plastic frame along the upper-right edge of the chamber in an array similar to Fig. 5.4. Each element is attached to a gimbal allowing for orientation and boresight adjustment. Each log-periodic antenna is 14-element, and matches the antenna parameters utilized in the log-periodic antenna modeled in the previous chapter. The frequency range of operation for these antennas is 2 GHz to 6 GHz. Antenna is constructed as a microstrip antenna with dimensions 0.127 m by 0.02 m. Fig. 5.5 shows the gain pattern of the OBS-14 antenna at 3 GHz and 6 GHz. The specified impedance of the OBS-14 antenna is 50Ω [4].

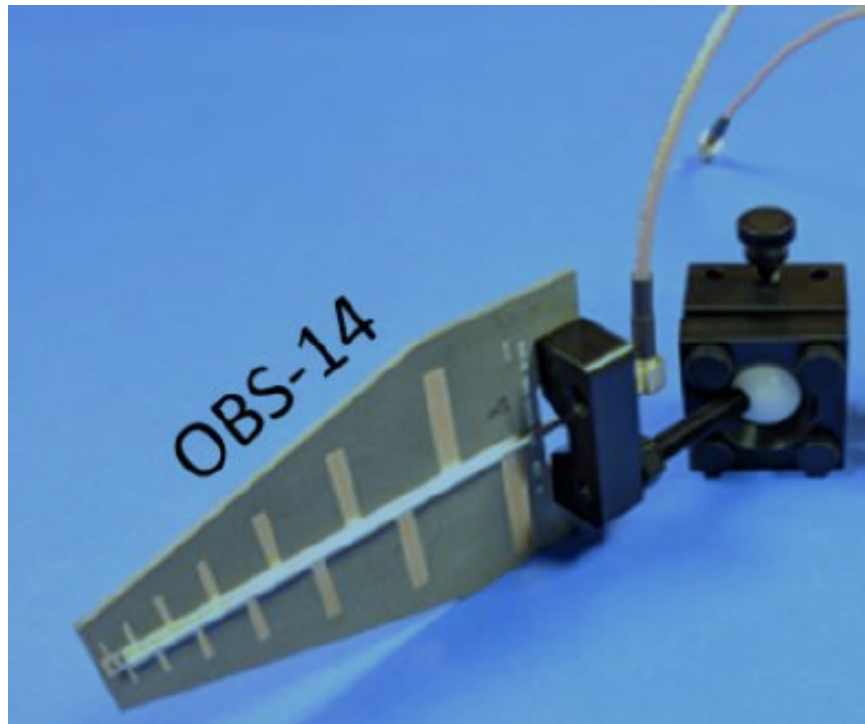


Figure 5.3: Octoscope OBS-14 Log Periodic Antenna [4]

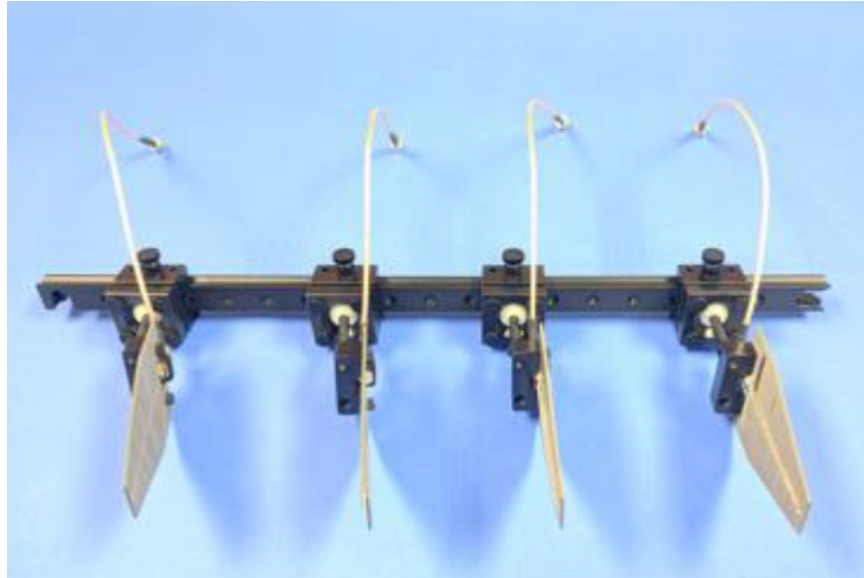


Figure 5.4: Octoscope OBS-14 Array [4]

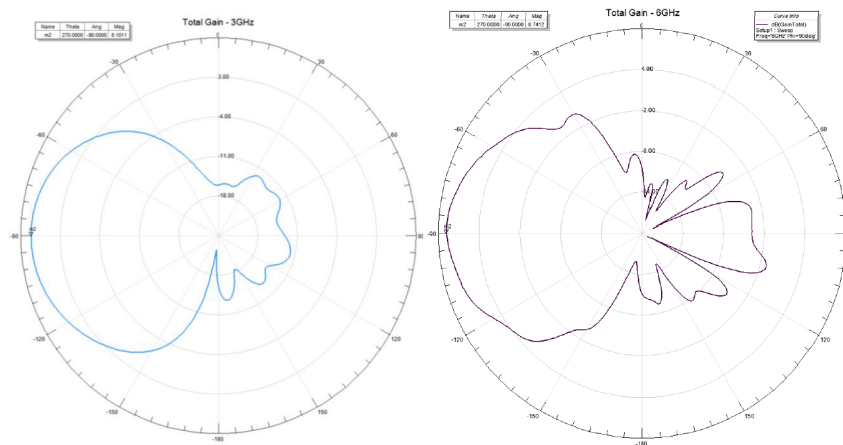


Figure 5.5: Octoscope OBS-14 Radiation Patterns [4]

The receiver dipole antenna is a Pasternack PE51083 rubber duck dual band antenna (Fig. 5.6). This antenna has frequency ranges from 2.4 GHz to 2.5 GHz, and 4.9 GHz to 5.825 GHz. It has a length of 0.108 m, a nominal 2 dBi omnidirectional gain and an input impedance of 50Ω [5]. Further inspection of the antenna revealed a half-wave sleeve dipole

construction.



Figure 5.6: Pasternack PE51083 Rubber Duck Antenna [5]

5.3.3 Measurement Equipment

Channel measurements were taken with a Keisight E5063A-2H5 ENA Vector Network Analyzer (VNA) with ECal automatic calibration set (Fig. 5.7). Each port has an input impedance of 50Ω . This VNA allows for 2-port S-parameter measurements over frequencies from 100 kHz to 18 GHz [6]. Each sweep can be used to sample up to 10001 points.



Figure 5.7: Keysight E5063A VNA [6]

5.4 Measurement Campaign Description

A measurement campaign was designed to spatially sample the channel from each of four stationary Log-Periodic probe antennas located along the top right edge of the chamber interior, with a single sleeve dipole moved along a grid to spatially sample the channel. Broadband 2 port S-parameters were captured with the VNA over the entire 5 GHz U-NII-1 through U-NII-2C frequency bands (a frequency range of 5.15 GHz to 5.725 GHz, the most widely-used frequencies used in 5 GHz WiFi). 1151 frequencies in this range were sampled, resulting in a frequency domain spacing of 500 kHz. Calibration of the VNA was performed using a Keysight E-cal set, and was calibrated to the ends of the SMA cables which connect directly to the SMA bulkheads on the side of the anechoic chamber. All unused anechoic chamber ports were terminated with 50Ω calibration standards, thus terminating all unused antennas with an impedance matching the specified antenna input impedance. Therefore,

the channel being measured is from the chamber probe SMA input to the chamber DUT SMA output. The channel measured includes the properties of the transmit and receive antennas and their interaction with each other through the environment.

As mentioned in previous sections, because the proximity between transmit and receive antennas is near the far-field threshold, interactions between the antennas cannot easily be defined in terms of far-field radiation patterns, isolated, and extracted from the measured channel data. As a result, the channel measurements and channel model will include the antennas as part of the model, indicating that this model generated from these measurements will be specific to this combination of antennas and this setup.

While the value of such a limited, specific model may at first appear to be low, a model specific to this configuration is still a valuable model in the context of a small chamber, where the probe antenna locations in the small chamber are fixed to a small number of possible configurations, receiver antennas are often dipoles, and the receiver antenna locations will be fixed to within a defined measurement zone. As a result, this channel model will provide relevant information about the expected channel and associated capacity and spatial correlation in the measurement region. This information is extremely important in validating the use of a small chamber as a repeatable testing environment.

Channel measurements can be directly derived from S-parameter measurements using the relation $H = \frac{S_{21}}{2}$, which assumes a match between source, characteristic, and load impedances in the system. Assuming the VNA has a source of V_S with 50Ω impedance at port 1, and a load impedance of 50Ω at port 2, and the input impedance of the transmit and receive antennas are also specified as 50Ω , then the input voltage into the system is a voltage divider between the source impedance (50Ω) and the input impedance to the system (also 50Ω), and $V_{in} = \frac{V_S}{2}$. Since $V_{out} = V_{load}$ and $S_{21} = \frac{V_{out}}{V_{in}}$, therefore $S_{21} = \frac{2V_{out}}{V_S}$. Rearranging

this equation, the channel is determined to be $H = \frac{V_{out}}{V_S} = \frac{S_{21}}{2}$. Thus the channel transfer function H is taken as one-half the measured S_{21} for the purpose of analysis.

With the definition of the parameters to be measured, the reasoning for this specific measurement campaign established, and the elements making up the system specified in the previous section, the physical setup of the system elements must be established, as well as a description of measurement campaign positions.

5.4.1 Antenna Orientations and Positions

Let a coordinate system defining locations within the chamber be established with origin in the bottom left back interior corner of the chamber, positive X axis along the bottom back edge of the chamber, negative y axis along the bottom left edge of the chamber, and positive Z axis along the back left side edge of the chamber. Coordinates are in meters, with maximum X and Z and minimum Y values defined by the dimensions of the chamber interior, and minimum X and Z and maximum Y values all defined as equal to zero. This coordinate system will be used to define antenna locations within the chamber.

Each of the four Log-Periodic probe antennas (as specified in the previous section) were attached using gimbals to the plastic support structure along the upper right edge of the chamber interior. Each of the four probes are indexed as 1 through 4, with probe center coordinates $P_1 = (0.7355, -0.4590, 0.3026)$ (near upper front right corner), $P_2 = (0.7644, -0.3374, 0.2935)$, $P_3 = (0.7373, -0.1837, 0.2913)$, and $P_4 = (0.7538, -0.0680, 0.3009)$ (near upper back right corner). Each probe antenna had its boresight aimed toward the bottom center of the chamber. Each probe antenna was oriented along a plane perpendicular to the bottom of the chamber that intersects both the chamber bottom center point and the probe antenna center point. All four probe antennas were connected to SMA bulkhead

connectors to the exterior of the chamber via short SMA cables tucked behind the foam absorber along the chamber wall. Fig. 5.8 shows a diagram of the chamber, including probe antenna positions in the chamber.

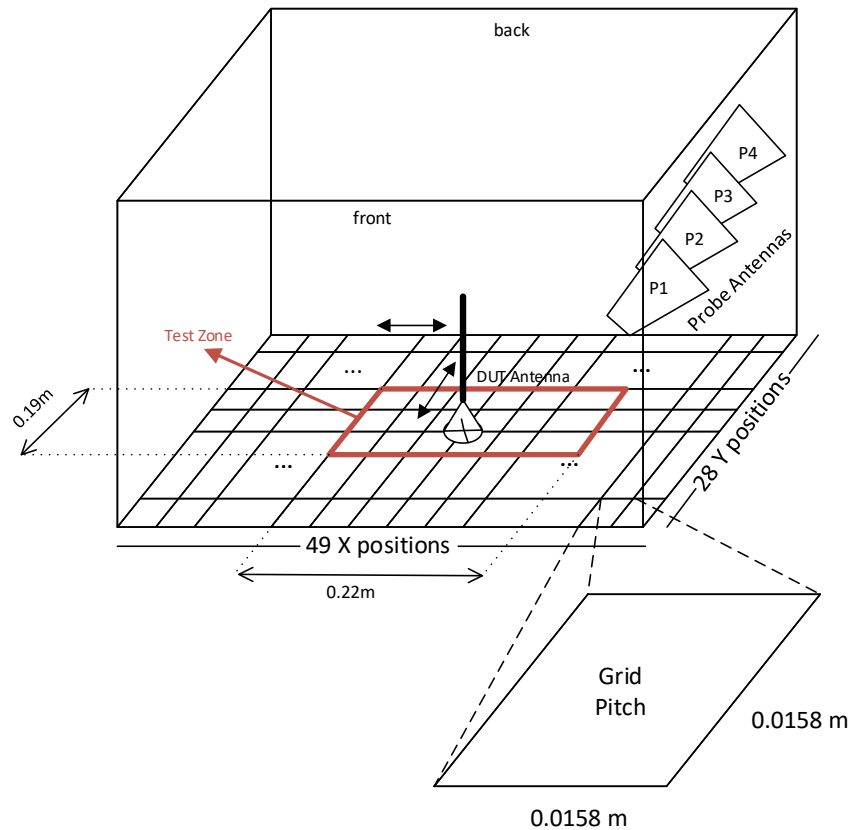


Figure 5.8: Chamber and Measurement System Diagram

A single sleeve dipole (as specified in the previous section) was used as a receiver. The dipole was kept in a Z orientation (and thus perpendicular to the chamber floor). The dipole center was located at $Z = 0.153$, which was kept constant by a plastic support structure holding the antenna in place. This plastic structure also allowed for precise positioning of the antenna along an X-Y grid on the chamber floor, allowing for spatial sampling of

the channel. The dipole DUT antenna is shown in Fig. 5.8, along with the directions of movement represented by arrows in the X and Y directions. The SMA cable connecting the dipole to the SMA bulkhead to the chamber exterior was tucked behind the foam absorbing material to minimize the length of cable exposed in the chamber.

5.4.2 Chosen Measurement Campaign Positions

The entire chamber interior bottom surface was measured in a grid with lines perpendicular to the X and Y axes with a pitch of 0.0158 m. This choice of this pitch is explained after the description of the measurement campaign. Fig. 5.8 illustrates the grid layout on the bottom of the chamber, along with the pitch of the grid.

For the measurement campaign, the VNA was calibrated using the E-cal for the desired frequency range, the two SMA cables from the VNA were attached to the port corresponding to the probe index and the receiver dipole. All other SMA ports were terminated with 50Ω calibration standards. The measurement campaign consisted of:

1. Placing the dipole antenna at the first/next intersection point on the grid.
2. Adjusting the SMA cable to minimize the length exposed beyond the absorbing material.
3. Closing the chamber door securely.
4. Initiating the VNA to take a measurement over the frequency range specified previously.
5. Saving the S parameter data in a file with the probe index and measurement point x and y index.

This procedure was repeated for each measurement position on the chamber floor grid, and that entire process was repeated for each of the four probe antennas acting as transmitter. A total of 49 X positions by 28 Y positions by 4 probes, or 5488 measurements were taken (each containing 2-port S parameters for 1151 frequencies). (Further measurements were taken at 10,001 frequencies between 1 GHz and 6 GHz (with identical spacing), as well as at 6 probe locations for a total of 8232 broadband measurements, but the scope of this investigation was reduced to 4 transmitters in the 5 GHz WiFi frequency range. The additional data set is for an extension of this work to other probe configurations and the 2.4 GHz WiFi band in future work.)

Measurement spacing was chosen to be less than that corresponding to the spatial Nyquist frequency of the highest frequency content in the system. (Sample spacing in space is comparable to sample period in time; the spatial sample frequency is inversely proportional to the spatial sample spacing just as frequency is inversely proportional to the sample period in time. Just as temporal signals must be sampled with a spacing less than that corresponding to the Nyquist sampling frequency, a spatially-sampled signal must be sampled with a spacing less than that corresponding to the spatial Nyquist sampling frequency.) With the highest frequency content in the system originally being considered as 6 GHz, the spatial sampling spacing must be less than half the corresponding wavelength of 0.050 m, i.e. less than 0.025 m. A grid spacing of 5/8 in., or approximately 0.0158 m, sufficiently met this requirement with sufficient headroom, and therefore was used.

Despite taking measurements over the entire chamber floor, the scope of analysis was narrowed to a feasible test zone near the center of the chamber. A range about the center of the chamber, about 22 cm by 19 cm, was chosen for performing the modeling and analysis. This is illustrated in Fig. 5.8 as a red box around the chamber center floor. For the remainder

of the analysis, this will be known as the test zone. This size will sufficiently contain most small- to mid-sized device under test (DUT) that would be well-suited to a small chamber test environment. X values therefore fall in the range 0.2856 to 0.5062, while Y values fall in the range -0.3247 to -0.1357. The method provided can be used in conjunction with measurements over a larger region to generate a model for a large test zone and DUT.

5.4.3 Resulting Dataset

Using the results of the measurement campaign, we extracted a sampled channel over the test zone for each of the four probes and 1151 frequencies at 195 measurement points. Presenting this entire data set of 4604 narrowband channels is not practical or useful in the scope of this document, but a representative sampled channel magnitude (Fig. 5.9) and phase plot (Fig. 5.10) for a single frequency (5.15 GHz) and probe (probe one) is presented here.

The magnitude plot (Fig. 5.9) shows the channel has a channel magnitude varying between -46 dB and -36 dB over the test zone. The actual sample points are at the intersection points of the grid, while the surrounding color between sample points is an interpolation of the magnitude. As Probe 1 is closest to the bottom-right corner of the plot, points in the lower-right corner of the plot are closest to the probe while points in the upper-left corner of the plot are farthest.

As expected, points generally farther from the probe have a lower channel magnitude while points closer to the probe have a generally higher channel magnitude. The bands of peaks and troughs in the magnitude over the test zone indicate the presence of constructive and destructive interference, likely caused by at least one additive reflection present within the chamber. These trends are present for other frequencies in the channel measured

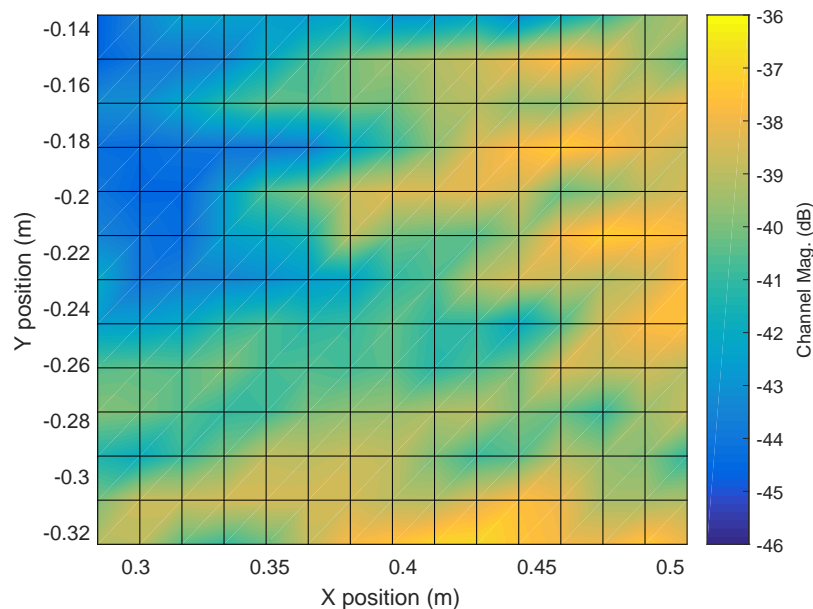


Figure 5.9: Measured Channel Magnitude (dB), Probe One (Located in Lower Right), 5.15 GHz

from probe one. The channel for probes two, three and four all exhibit similar magnitude trends proportional to distance from each probe, but have less pronounced constructive and destructive interference.

The phase plot (Fig.5.10) exhibits primarily concentric Eikonal surfaces with the center located near probe one. This is expected as the line of sight (LOS) component of the channel is dominant, and the LOS component is directly from probe one. Due to the spatial sampling resolution and the linear interpolation of plotted phase between points, the Eikonal surfaces plotted between sample points do not accurately illustrate the curved nature of the surfaces. Also, the interpolation does not properly account for phase wrapping by increasing or decreasing to the point of discontinuity and wrapping around. (For example, if one sampled point of phase is $-\frac{\pi}{2}$ and the following is $\frac{\pi}{2}$, and the actual phase process between

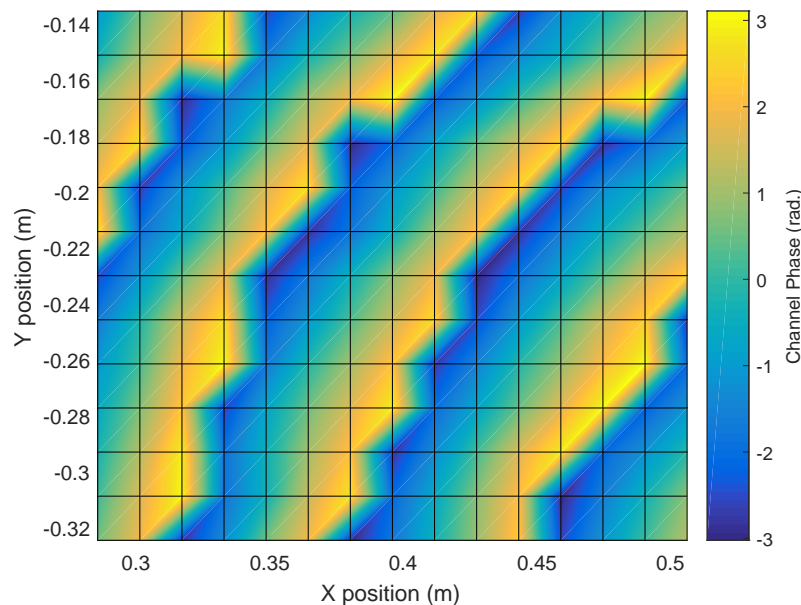


Figure 5.10: Measured Channel Phase (rad.), Probe One (Located in Lower Right), 5.15 GHz

the two points is a line between $-\frac{\pi}{2}$, and $-\pi$, then a discontinuity to π , and a line from π to $\frac{\pi}{2}$, the interpolation line would be directly from $-\frac{\pi}{2}$ and $\frac{\pi}{2}$ with no wrapped phase. Thus discontinuities between sample points are not captured in a plot consisting of filling between points with interpolation. Different phase differences between consecutive points bordering a discontinuity will exhibit different interpolation slopes, and the interpolation region between points covering a series of discontinuities may appear uneven, as is the case in Fig.5.10). These issues in interpolation cause the Eikonal surfaces to appear jagged in the plot.

To reiterate, this jagged nature of the phase plot is only a side effect of the method of displaying data. This inaccuracy in presentation should not be confused with introducing an inaccuracy to the collected data that will be present in our model, which rely on curve fitting and spectral analysis and not linear interpolation. The general trends of this plot, i.e.

curved concentric Eikonal surfaces centered around the probe for which the measurement was taken, are present in all phase plots from all probes at all frequencies.

5.5 Modeling of Measurement Data

With the channel sampled in frequency and space, the first part of the modeling process is to determine the minimum number of each type of SAF (point sources and plane waves) required to achieve a desired level of accuracy (i.e. sufficiently-low EVM across the test zone). In our analysis, a general observed trend was that more SAF were required for a given level of EVM at higher frequencies than low frequencies, so selecting the number of SAF through analysis at the highest frequency of the relevant measurement campaign (5.725 GHz) will provide a sufficient number of SAF for all other frequencies in the measurement campaign.

An investigation into the LN mean and LN SD of the EVM over the test zone was conducted for all possible combinations of 0 to 6 point sources and 0 to 20 plane waves for each of the four probes at 5.725 GHz using the procedure from the previous chapter. As in the analysis presented in the previous chapter, a value of LN mean + 1 SD EVM over the test zone was computed, and presented for each probe and combination of SAF. All possible combinations of SAF for a probe are presented in each plot (Fig. 5.11 - Fig. 5.14). A threshold of -15 dB for LN mean + 1 SD EVM was established, and all SAF combinations with worse EVM performance were truncated from the plots for easy analysis.

Analysis of these plots show that probes two and three (Fig. 5.12 and Fig. 5.12) require far more SAF components than probes two and four to achieve a LN mean + 1 SD EVM of -15 dB. The combination of SAF with a LN mean + 1 SD less than -15 dB for all four probes with the fewest number of components is three point sources (spherical components) and 19

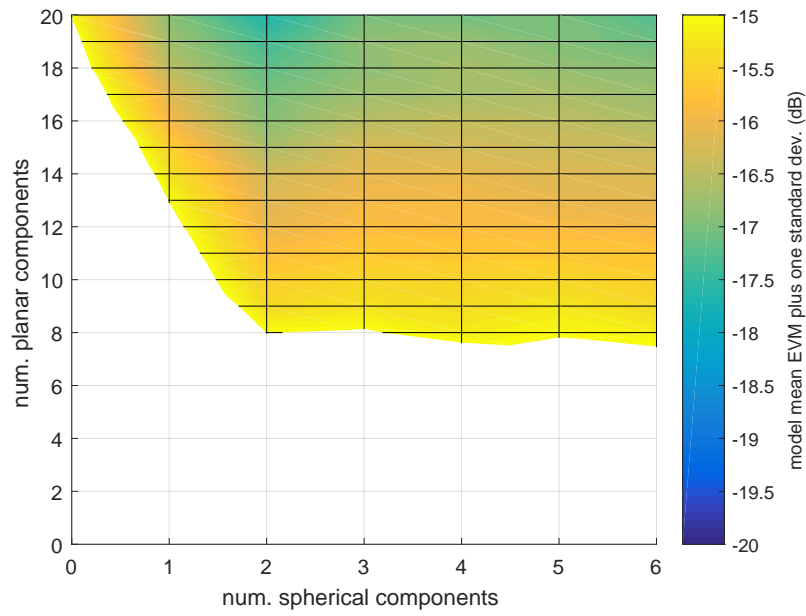


Figure 5.11: LN Mean + σ EVM, Probe One, 5.725 GHz

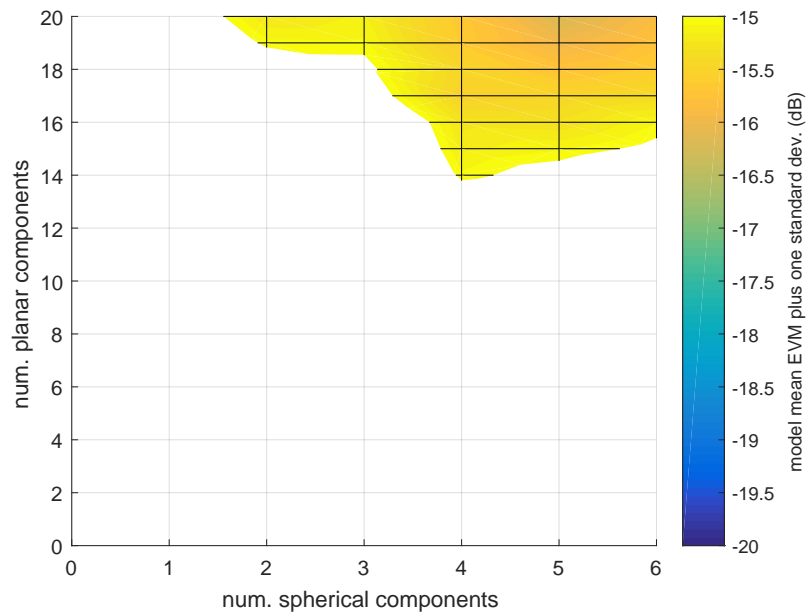


Figure 5.12: LN Mean + σ EVM, Probe Two, 5.725 GHz

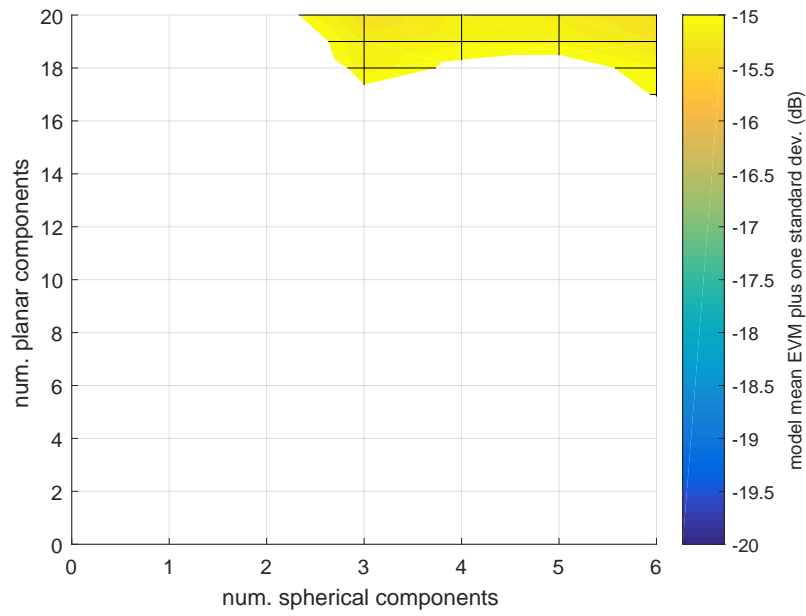


Figure 5.13: LN Mean + σ EVM, Probe Three, 5.725 GHz

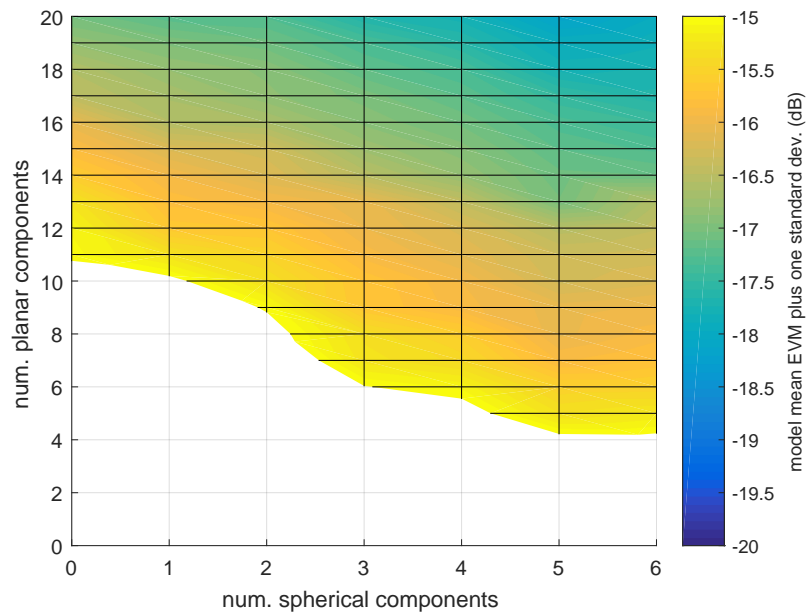


Figure 5.14: LN Mean + σ EVM, Probe Four, 5.725 GHz

plane wave components (planar components). It is this combination of 3 point sources and 19 plane waves that will be used for the remainder of the channel modeling at all frequencies for all probes, as this combination is of sufficient accuracy for even the worst-case probe and frequency.

5.5.1 Analysis of Complex Geostatistical Covariance Of Measurements

After determining the number and type of SAF used, the measurement data for a specific frequency and probe can be used in conjunction with the procedure in the previous chapter to iteratively determine first the 3 point sources and then the 19 plane waves. These 22 SAF evaluated at each measurement point in conjunction with a constant term can be fit to the measured data using least squares to obtain an initial estimate for the SAF coefficients, $\vec{\beta}$. This is then used to obtain an estimate of the residual, $\vec{\varepsilon}$. This residual is modeled statistically as in Sec. 5.1.3. This estimated residual model is then used to refine the complex coefficients of the model, which is then used to refine the residual model, and so forth until convergence is obtained.

For the purpose of investigating the properties of the empirical and modeled spatial covariance, the magnitude, real, and imaginary components of the empirically calculated channel covariance, empirically calculated residual covariance, and model covariance will be presented for the channel at a single frequency and probe.

First, the magnitude (Fig. 5.15), real (Fig. 5.16) and imaginary (Fig. 5.17) components of the spatial covariance of the measured channel, and the corresponding spatial power (Fig. 5.18) spectrum are observed for probe one at a frequency of 5.15 GHz. This information is not used in the channel model, but is useful in comparing characteristics with the empirical

and modeled residual covariance. Only separations for which significant signal overlap is achieved are analyzed, producing an oval-shaped region for which the spatial covariance is calculated.

The measured channel has a high magnitude of spatial cross-covariance along the general direction of propagation in the test zone, with the magnitude spreading in direction as separation distance increases (Fig. 5.15). The real and imaginary plots (Fig. 5.16) and 5.17)) have well-defined peaks and troughs perpendicular to the expected direction of travel. Finally, taking the spatial FFT of the windowed complex spatial cross-correlation (Fig. 5.18) we observe a strong spectral peak with slight spread, at the values of wave vector indicating wave propagation in the direction away from probe one, as expected. The remainder of the spectrum is generally 20 dB lower or less than the peak region, and without any significant peaks or noticeable structure. This would indicate that channel components beyond the LOS component will be significantly lower in magnitude.

The estimated empirical residual spatial cross-covariance is observed next, resulting from subtracting the weighted SAF from the measured channel. The magnitude of the empirical residual spatial cross-covariance as shown in in Fig.5.19 shows a small region of cross-correlation at very short separation lengths, and low-level cross-covariance at all other separations. Occasional small peaks occur at some large separations (e.g. near a separation vector of $(0.2, 0.03)$), but relative to small separations, there are comparatively fewer data points used for the expected values in these calculations, and therefore the estimated expectation may deviate from the actual mean.

The real part of the estimated empirical residual spatial cross-covariance as shown in Fig. 5.20 exhibits a peak at zero separation, and rapidly drops off to near-zero cross-covariance for all other separations. There is a faint low-level pattern in the cross-covariance of low-level

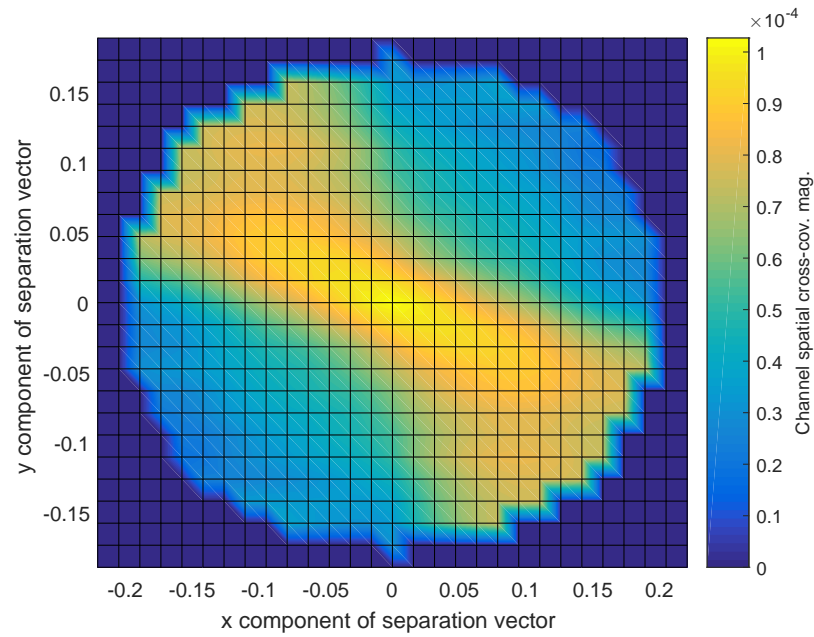


Figure 5.15: Measured Channel Spatial X-Cov., Mag., Probe One, 5.15 GHz

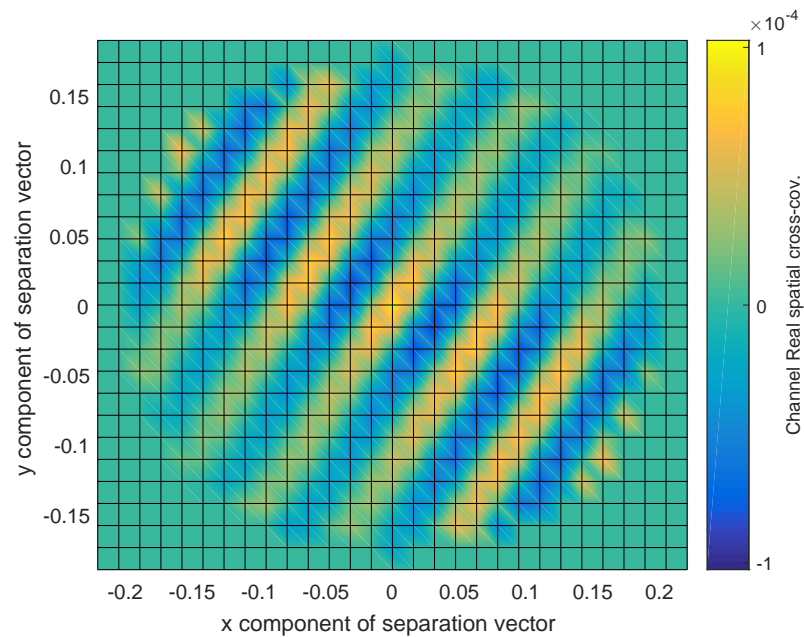


Figure 5.16: Measured Channel Spatial X-Cov., Real, Probe One, 5.15 GHz

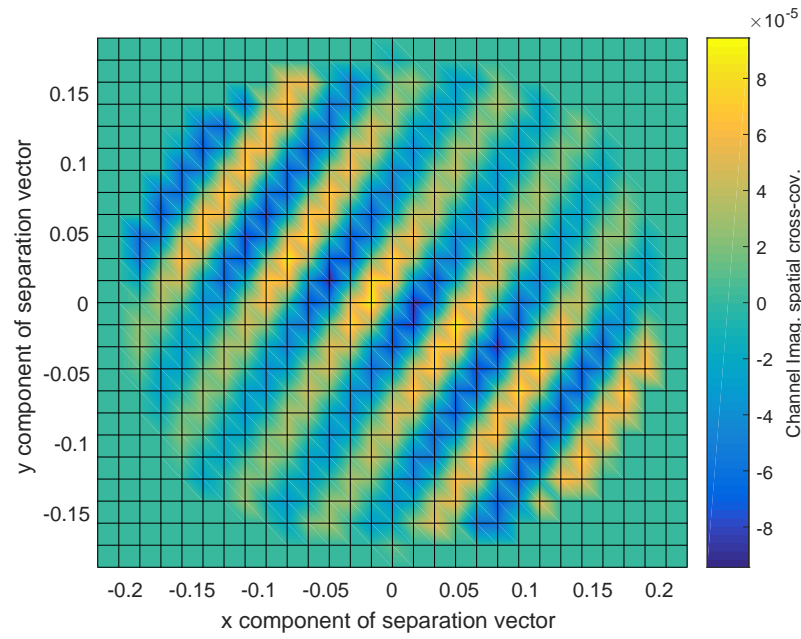


Figure 5.17: Measured Channel Spatial X-Cov., Imag., Probe One, 5.15 GHz

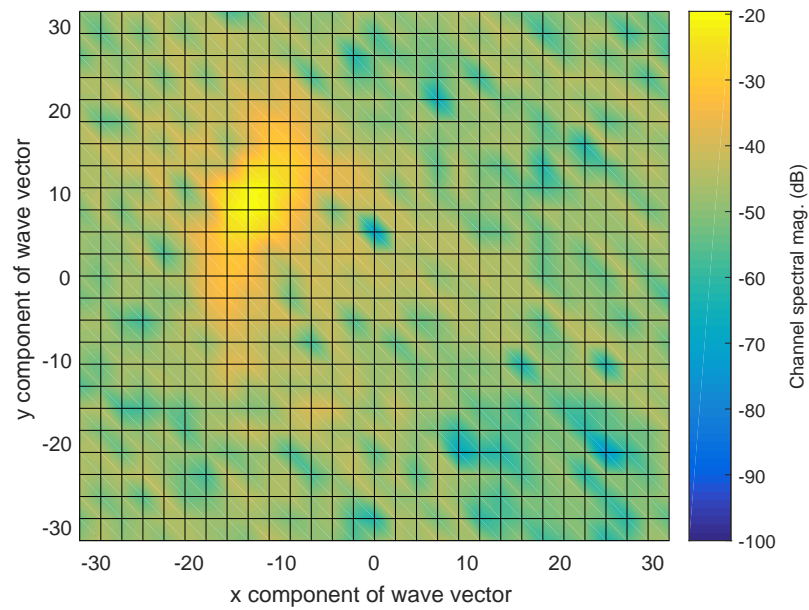


Figure 5.18: Measured Channel Spatial Power Spectrum, Probe One, 5.15 GHz

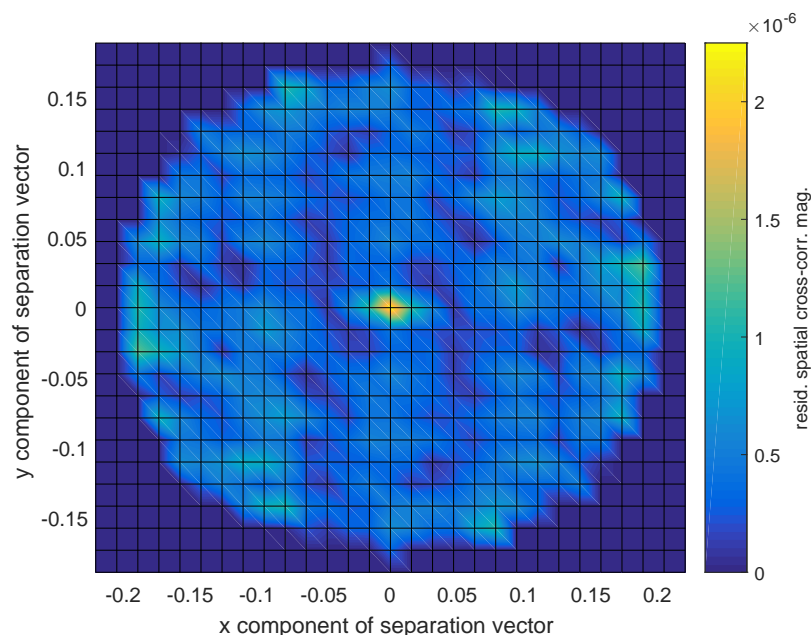


Figure 5.19: Residual Emp. Spatial X-Cov., Mag., Probe One, 5.15 GHz

peaks and troughs similar in direction to those observed in the real and imaginary cross-covariance of the channel itself, indicating that a very small part of the deterministic part of the channel remains in the residual that was not modeled by the SAF. For all purposes the magnitude of this pattern is significantly less than the peak, and therefore can be neglected from consideration in choosing a model cross-covariance function.

The imaginary part of the estimated empirical residual spatial cross-covariance as shown in Fig. 5.21 exhibits positive and negative peaks at separation vectors of approximately $(-0.01,0)$ and $(0.01,0)$ respectively. In conjunction with the real peak at zero separation, these individual imaginary positive and negative peaks are included in the Gaussian complex covariance model selected previously in Sec. 5.1.3, indicating this model was a good choice for modeling the residual present in our SAF-fitted channel. It should be noted that the imaginary part of the empirical residual spatial cross-covariance has a similar faint pattern

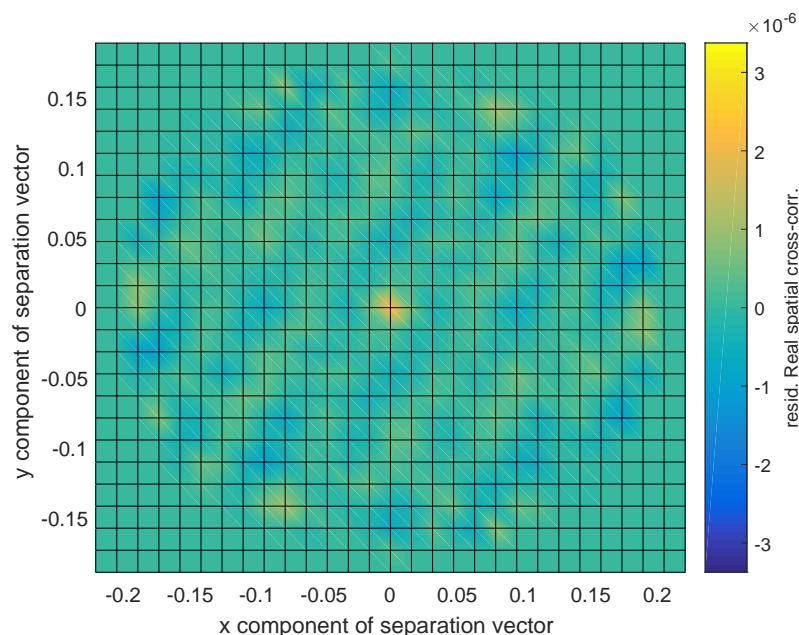


Figure 5.20: Residual Emp. Spatial X-Cov., Real, Probe One, 5.15 GHz

with low-level peaks and troughs in directions similar to the real and imaginary channel spatial cross-covariance plots. Also, the magnitude of the positive and negative imaginary peaks is lower than the magnitude of the real peak, and is also closer in level to the low-level pattern, which will have an effect on the fitting of the model to the data.

Next, for comparison (and not for use in the model itself), the spatial power spectrum of the empirical estimated residual is observed (Fig. 5.22), scaled identically to the spectrum of the channel (i.e. -100 dB to -20 dB). An approximately white spectrum with relative uniformity across all wave vectors and no well-defined peaks shows that the residual is noise-like and modeling with a cross-covariance model would be practical. Indeed, the spectrum is relatively uniform, particularly compared to the channel spectrum (Fig. 5.18) which has well-defined peak region. The residual spectrum does have more power in the negative X half space, and does have a couple small peaks near the wave vector corresponding to the peak in

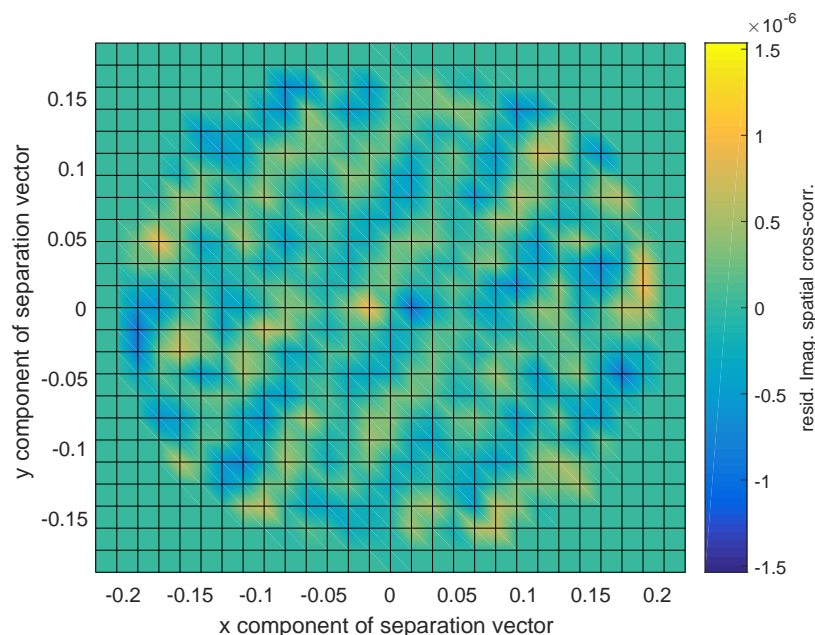


Figure 5.21: Residual Emp. Spatial X-Cov., Imag., Probe One, 5.15 GHz

the channel spectrum, which explains the faint patterns in the real and imaginary residual cross-correlation plots reminiscent of the channel cross-correlation real and imaginary plots. It is possible that adding additional plane waves to the SAF set could account for these peaks and further whiten the residual spectrum, but this would add unnecessary complexity to the model for the accuracy we wish to achieve.

With the empirical residual spatial cross-covariance calculated for the channel residual, the procedure from Sec. 5.1.3 can be applied to fit the empirical data to a complex Gaussian covariance model. This fitting process yields the covariance at zero distance (directly taken as the empirical cross-covariance at zero separation), an angle of maximum range (θ), the maximum range coefficient a_θ , and minimum range coefficient a_ϕ , as well as the translation vector \vec{c} . These parameters minimize the difference between the model and the empirical cross-covariance through the use of a global search algorithm. This procedure resulted in

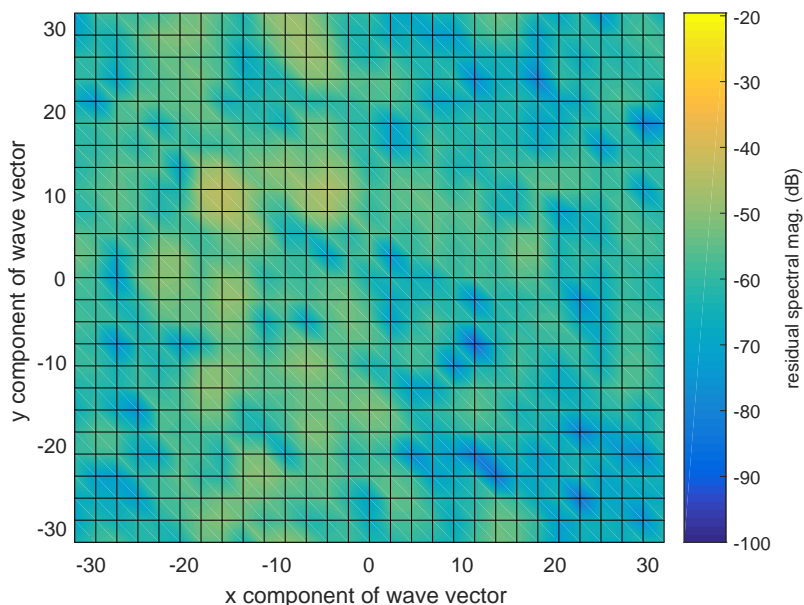


Figure 5.22: Residual Emp. Spatial Power Spectrum, Probe One, 5.15 GHz

the cross-covariance model yielding Figs. 5.23, 5.24, and 5.25.

Comparing the model cross-covariance magnitude (Fig. 5.23) to empirical cross-covariance magnitude (Fig. 5.19), we notice that the model has equivalent zero-separation magnitude to the empirical, and has a similar rate of drop-off in cross-correlation as separation distance increases. While the empirical separation sampling rate doesn't provide enough resolution to obtain the maximum and minimum ranges as well as the angle of maximum range by visual inspection with certainty, it does appear that the angle of maximum range could be approximately 0 radians as the width of the peak region appears longer along the X axis than in any other direction. In the model, the angle of maximum range appears to be in the direction of the LOS signal, perhaps influenced by the small residual pattern in the direction of the LOS signal observed in the real and imaginary LOS plots. With the exception of the angle of maximum range differing slightly (and for reasons that are expected), the model is

reasonably close to the observed empirical magnitude plot.

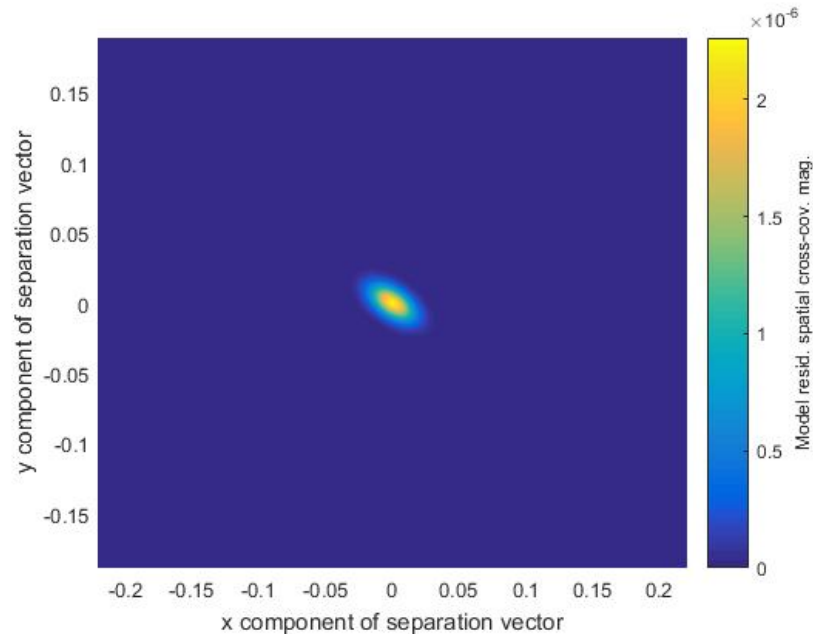


Figure 5.23: Residual Model Spatial X-Cov., Mag., Probe One, 5.15 GHz

Comparing the model to empirical real cross-covariance plots (Figs. 5.24 and 5.20 respectively), the real component appears to have identical real cross-covariance at zero separation between the two plots, and both plots rapidly decrease in magnitude to zero in all separation directions. Once again, due to limited spatial resolution, the shape and orientation of the empirical cross-covariance peak is not observable by inspection, but the maximum and minimum range of the model are within a similar short separation range as in the empirical plot, and thus once again the model is reasonably close to the observed empirical real plot.

Finally, comparing the model to empirical imaginary cross-covariance plots, as shown in Figs. 5.25 and 5.21 respectively, the separation of the positive and negative peaks near zero-separation are similar, and the region around these peaks is zero cross-correlation in both plots. The magnitudes of the two empirical peaks are approximately two orders of

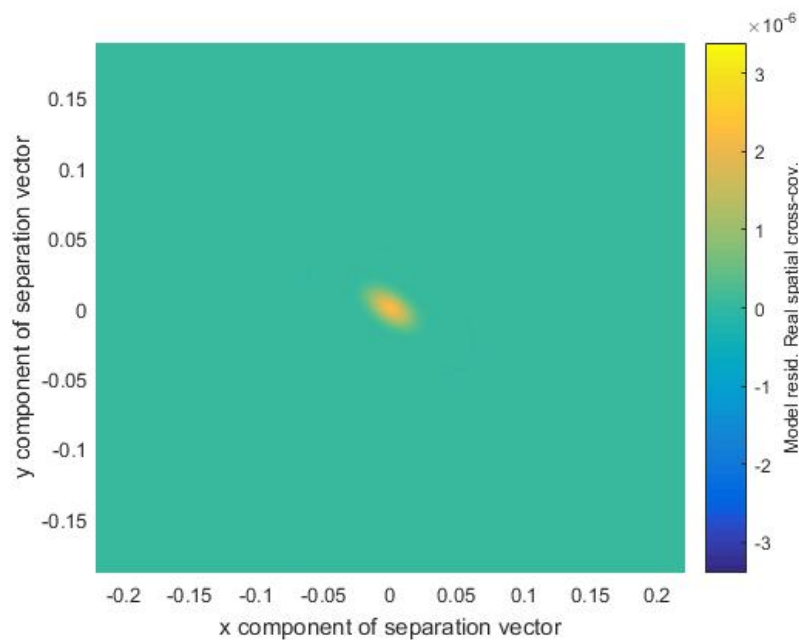


Figure 5.24: Residual Model Spatial X-Cov., Real, Probe One, 5.15 GHz

magnitude higher than the corresponding model peaks, and the model has the axis along which the two peaks are located in the direction of the small residual pattern (the LOS direction) instead of along the X axis as in the empirical plot. The direction of the axis of the peaks once again is likely due to the residual pattern, however the decreased peak magnitudes are possibly due to either the global search algorithm becoming consistently stuck in a local minimum when searching for parameters that minimized the difference between the model and empirical imaginary components, or the residual signal beyond the two peaks, which is only slightly lower in magnitude than the two peaks, significantly differed from zero and had a disproportionate effect on the calculation of the imaginary component. Further investigation of this is necessary, but through experimentation, this global optimization fit model was sufficiently accurate for our model and was not pursued further.

With SAF chosen and a sufficiently-accurate method for modeling the residual cross-

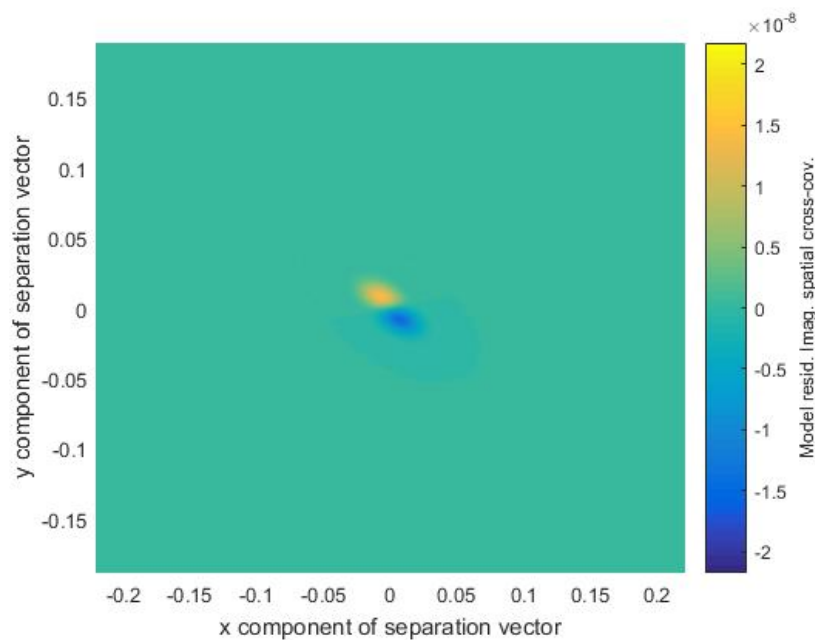


Figure 5.25: Residual Model Spatial X-Cov., Imag., Probe One, 5.15 GHz

covariance in terms of parameters, Geostatistical Regression (Sec. 5.1.4) is applied to iteratively refine the estimates of the SAF complex coefficients and the residual cross-covariance model parameters until all coefficients and parameters converge. This collection of SAF, coefficients, and parameters allow for channel estimation using Geostatistical Kriging (Sec. 5.1.5) at any location in the test zone, for the probe and frequency combination for which the model was generated.

As an aside, model estimations at measurement points will estimate the residual as the actual measurement residual, while estimations between measurement points will estimate the residual based on the spatial cross-covariance model in conjunction with measurement residuals at nearby points. In a sense, the method of Kriging is statistically-informed interpolation. Because model estimates at measurement points are almost exactly equal to the measurement, the error vector is approximately zero, and EVM at the measurement points

trends towards negative infinity. As such, in subsequent sections, the EVM of the estimated channel formed by the product of the SAF and complex coefficients $\vec{\beta}$ after the Geostatistical Regression process at all measurement points will be used to evaluate model accuracy.

Instead of running this entire procedure at each probe and frequency combination, the method of determining a set of SAF at a base frequency and re-using a frequency-scaled version of this set at a wide range of frequencies (as presented in Sec. 5.2) was investigated.

5.5.2 Selected Wideband Frequency Bands for Modeling

A method of applying a set of SAF at an arbitrary base frequency f_0 to a band of near frequencies was specified in Sec. 5.2. To effectively apply this method to our dataset, it was important to determine what bandwidth above or below the base frequency for which a set of SAF could be re-used while still maintaining acceptable accuracy. We chose various arbitrary base frequencies for all probes within our dataset, established a set of SAF at each base frequency, and then fitted frequency-scaled versions of the SAF to the channel measurements at each frequency within 100 MHz of the base frequency. While frequencies above the base frequency exhibited a rapid increase in EVM, frequencies below each base frequency generally exhibited a small increase of EVM and in many cases a decrease of EVM. Further investigation determined that a set of SAF could be used up to 160 MHz below the base frequency in all cases before a significant increase in EVM was observed. As such, we chose 160 MHz bands to model using SAF calculated at a base frequency at the end of each band. For each probe, the measurement set was divided into bands from 5.15 GHz to 5.31 GHz (with base frequency 5.31 GHz), 5.31 GHz to 5.47 GHz (with base frequency 5.47 GHz), 5.47 GHz to 5.63 GHz (with base frequency 5.63 GHz), and a final shorter band from 5.63 GHz to 5.725 GHz (with base frequency 5.725 GHz).

5.5.3 Performance Analysis of Frequency-Scaled Spatial Attribute Functions

Using the base frequencies and frequency bands specified, the SAF of each base frequency were scaled to each measurement frequency in the band and used to calculate coefficients and model parameters using Geostatistical Regression (Sec. 5.1.4), using the procedure specified in Sec. 5.2.1. The measured signal at each frequency in a band, scaled SAF and calculated coefficients at each frequency were used to calculate the residual and EVM at each frequency. Because showing a plot of the LN mean EVM of each combination of band and probe (a total of 16 plots) would be superfluous, two such selected plots will be included here.

Figs. 5.26 and 5.27 show two representative probe and band combinations, for probe one band four, and probe four band three respectively. Probe 1 band 4 has the worst representative increase in EVM as frequency decreases from the base frequency (still less than a 2 dB increase). It should be noted that frequencies in this band below 5.63 GHz are unused as they overlap with band three, and therefore the 5.56 to 5.63 GHz range with increased EVM does not adversely affect the model accuracy. Probe four band three shows a general decrease in LN mean EVM as frequency decreases, showing that using the scaled SAF at these frequencies is even more accurate than their use at the base frequency of this band!

All other bands have performance between these two relative extremes, and therefore the use of scaled SAF from a base frequency over a lower band of 160 MHz does not have a significant detriment to model accuracy, while saving significant computational cost of iteratively determining a separate set of SAF at each frequency.

This process has empirically generated all complex SAF coefficients and model param-

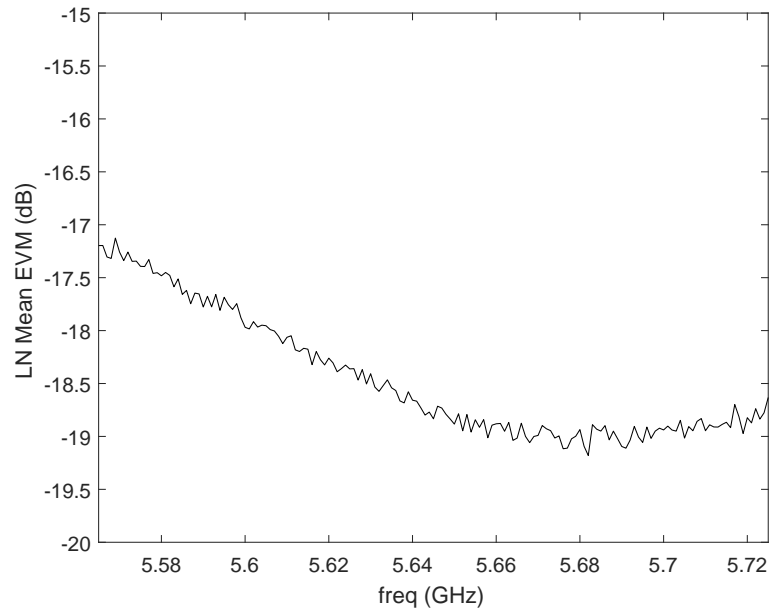


Figure 5.26: Empirical LN Mean EVM vs. Freq., Probe One Band Four

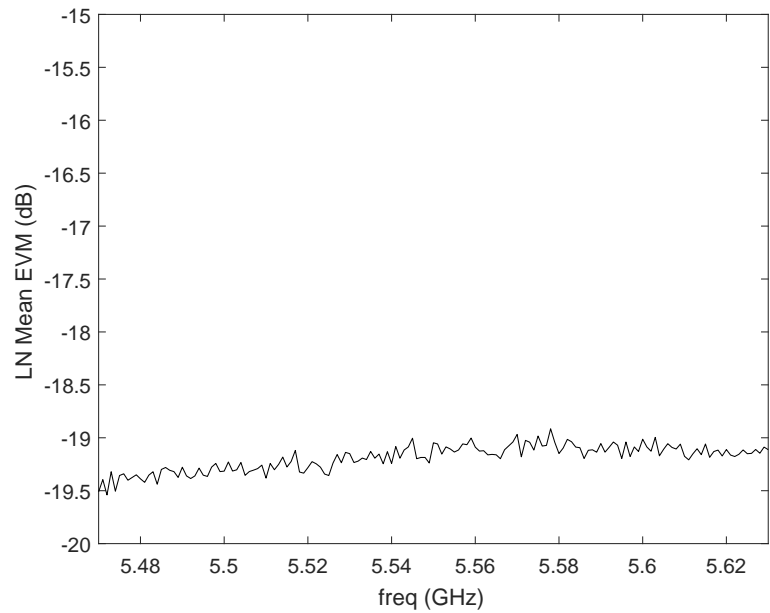


Figure 5.27: Empirical LN Mean EVM vs. Freq., Probe Four Band Three

eters at each frequency using scaled SAF. These empirical parameters can be modeled as polynomial functions of frequency. This process is described and evaluated in the following section.

5.5.4 Spatial Attribute Function Set Extension to Wideband Model

The procedure in Sec. 5.2.2 (polynomial regression of each parameter versus frequency) is applied to the magnitude and phase of each of the 23 coefficients in $\vec{\beta}$, the values of the three parameters in $\vec{\theta}$, to σ^2 , and the values of the two parameters in \vec{c} . This is performed for each probe and each band, for a total of 52 regressions by 16 bands.

The degree of each polynomial parameter regression was selected to closely following the trends of the modeled parameter over all instances of that parameter for all bands and probes. For the magnitude and phase models of each value of $\vec{\beta}$, a 13th-order polynomial and a 2nd-order polynomial respectively are fit to the magnitude and phase of each value of beta over the frequencies of each band and probe. For each value of σ^2 , $\vec{\theta}$, and \vec{c} , a 13th-order polynomial model was also fit. In the case of the phase of $\vec{\beta}$, every plot was observed to be primarily linear over frequency, so a low-order polynomial was sufficient to describe this parameter. All other parameters occasionally had characteristics that required a higher-order polynomial to accurately follow the trend of the parameter over all frequencies in a band.

Once again, due to the large data set, A representative selection of empirical and modeled parameters versus frequency is presented. Magnitude and phase of a point source coefficient β_1 for probe one band two as in Figs. 5.28 and 5.29 respectively, magnitude and phase of a plane wave coefficient β_4 for probe two band one as in Figs. 5.30 and 5.31 respectively, values of σ^2 for probe two band four as in Fig. 5.32, and values of c_1 for probe three band

two as in Fig 5.33.

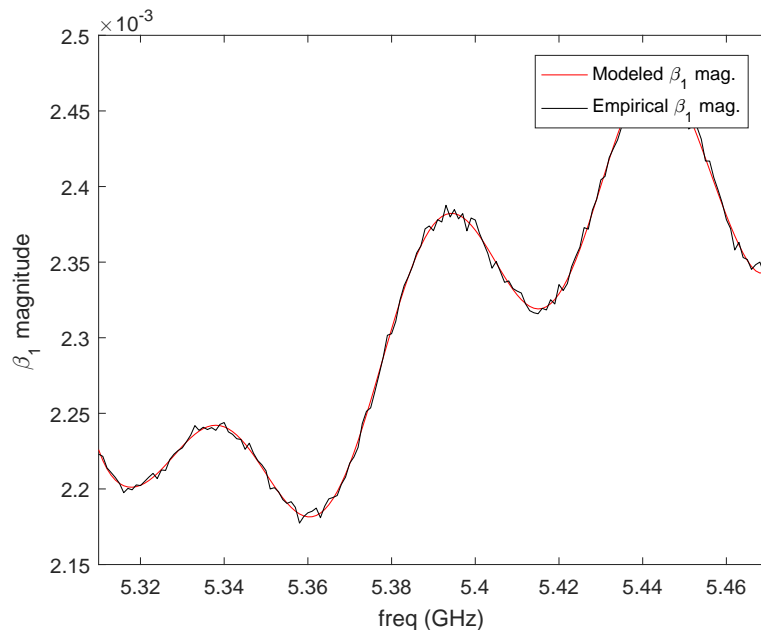


Figure 5.28: Emp. and Poly. Model of β_1 Mag. vs. Freq., Probe One Band Two

In general, the empirical parameters being modeled range from essentially noise-free (phase plots in Figs. 5.29 and 5.31) and very low noise (magnitude of β_1 in Fig. 5.28) to relatively constant variance noise following a clear trend (c_1 in Fig. 5.33). In all cases, the polynomial model closely follows the trend of the parameter being modeled. The statistics of the residual of this polynomial fit could be used to determine the error of each model, but this information is superfluous in the context of the goal of this work. Evaluation of this polynomial model method will be determined empirically through its effect on EVM relative to the EVM from the use of empirical model parameters.

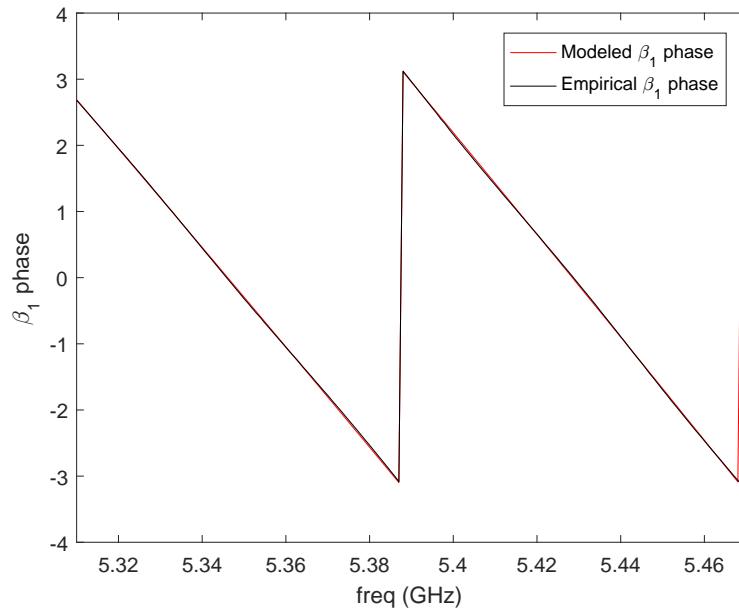


Figure 5.29: Emp. and Poly. Model of β_1 Phase vs. Freq., Probe One Band Two

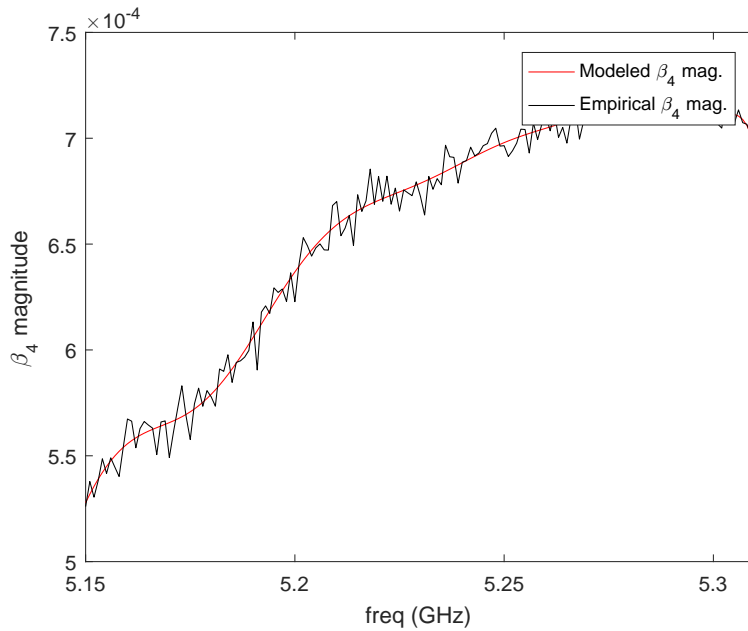


Figure 5.30: Emp. and Poly. Model of β_4 Mag. vs. Freq., Probe Two Band One

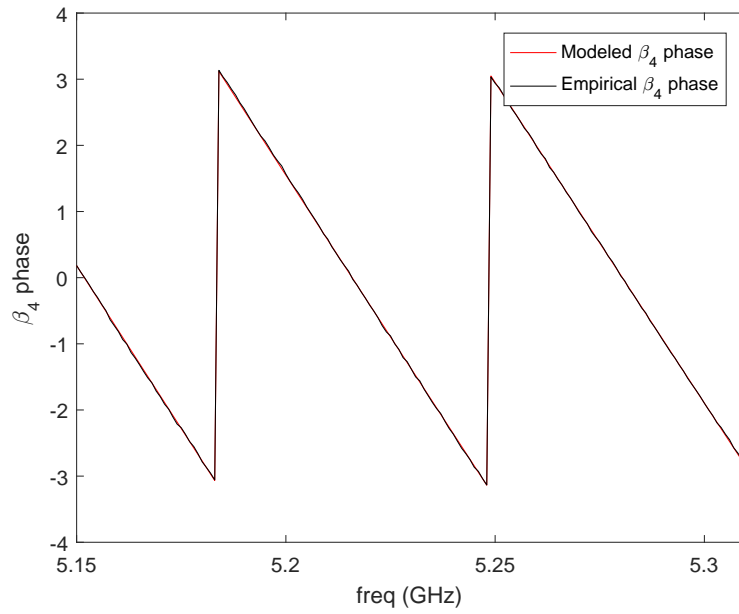


Figure 5.31: Emp. and Poly. Model of β_4 PHase vs. Freq., Probe Two Band One

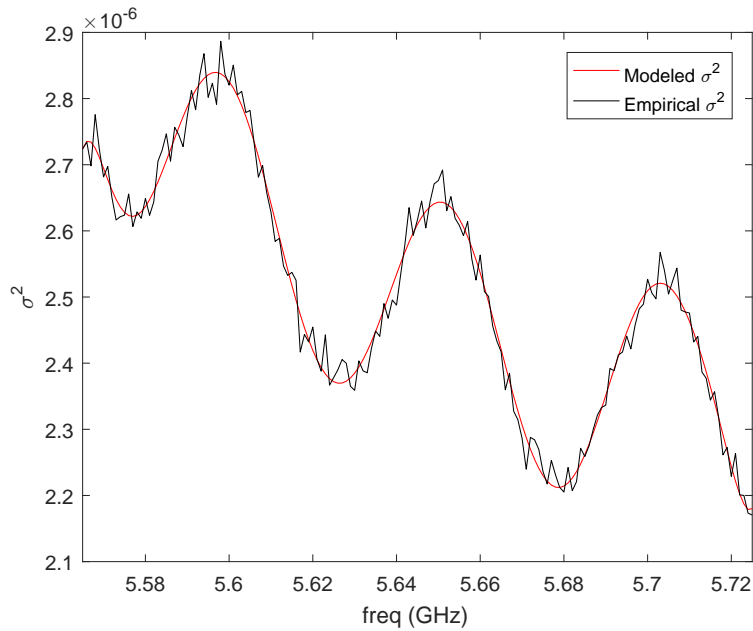


Figure 5.32: Emp. and Poly. Model of σ^2 vs. Freq., Probe Two Band Four

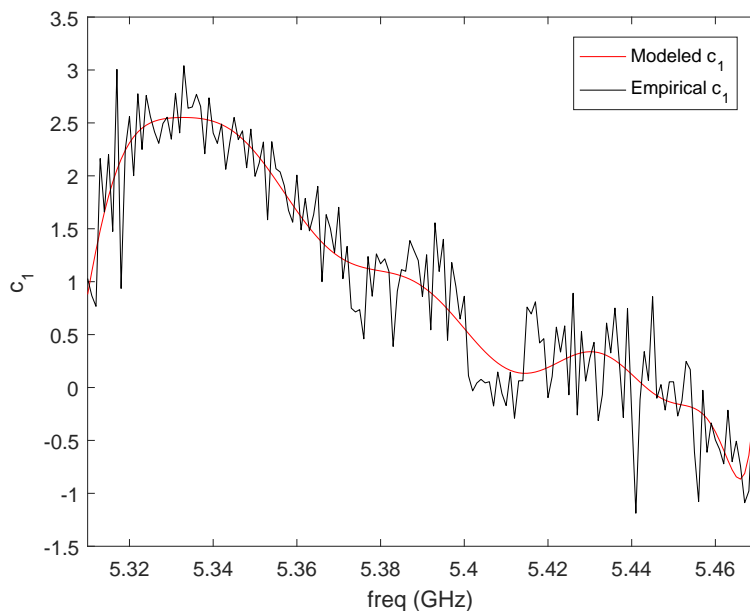


Figure 5.33: Emp. and Poly. Model of c_1 vs. Freq., Probe Three Band Two

5.5.5 Wideband Model Accuracy

Polynomial model $\vec{\beta}$ values used in conjunction with frequency-scaled SAF were used to estimate the channel at all measurement points for all frequencies in each band, and the LN mean EVM was calculated. Two representative probe and band EVM plots are included here, Probe one band four as in Fig. 5.34 and Probe four band three as in Fig. 5.35. These were selected to match the plots of EVM calculated using empirical values of $\vec{\beta}$ as in Figs. 5.26 and 5.27, for direct comparison so that the effect of parameter polynomial modeling on EVM can be observed.

The EVM observed in Fig. 5.34 follows the same trend as Fig. 5.26, with small increases in EVM at around 5.61 GHz, 5.66 GHz, and 5.69 GHz. Likewise, Fig. 5.35 follows the same trend as Fig. 5.27 with small increases in EVM at about 5.51 GHz, 5.59 GHz, and 5.61 GHz.

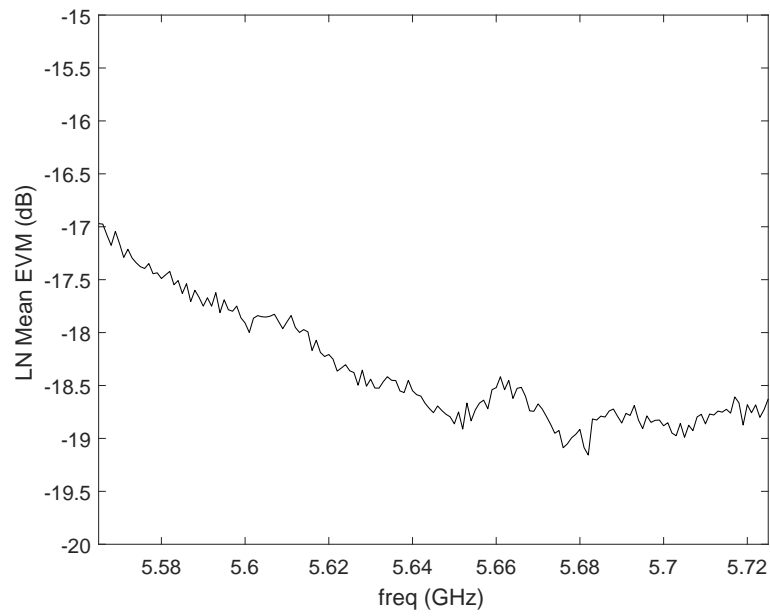


Figure 5.34: Modeled LN Mean EVM vs. Freq., Probe One Band Four

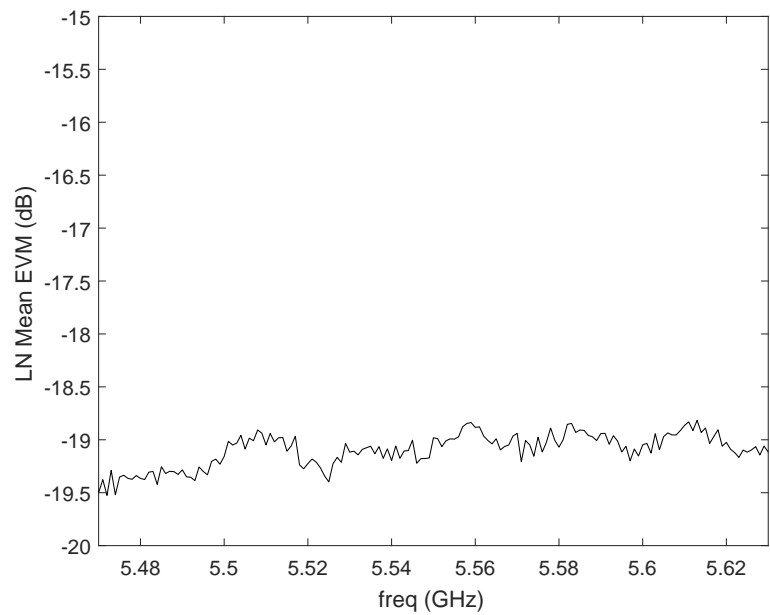


Figure 5.35: Modeled LN Mean EVM vs. Freq., Probe Four Band Three

The following plots show the calculated difference at each frequency between the Empirical and Polynomial parameter model LN mean EVM. Fig 5.37 shows the differences for probe one band four, and Fig 5.36 shows the differences for probe four, band three. In both cases, the increase in LN mean EVM using the polynomial parameter models is between 0 and 0.25 dB, with two to three small frequency ranges spiking up to less than 0.4 or 0.5 dB increase in EVM. No other LN mean EVM difference plot for any other probe or band was observed to have a difference of greater than 0.5 dB, and in general much lower.

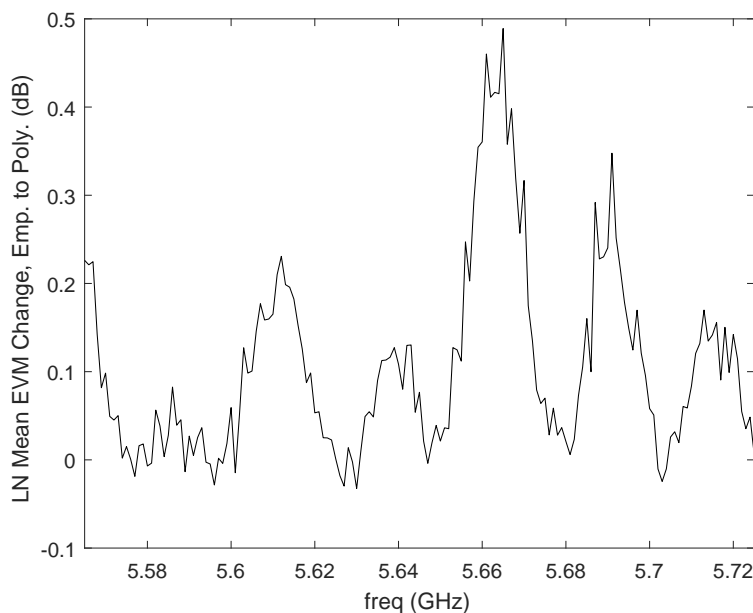


Figure 5.36: Increase of LN Mean EVM From Emp. to Model vs. Freq., Probe 1 Band 4

This result indicates that the use of a polynomial parameter model has an almost negligible effect on model accuracy, and can be used in place of the empirical parameters at each frequency. This completes the generation and validation of a channel model for the Octobox small anechoic chamber.

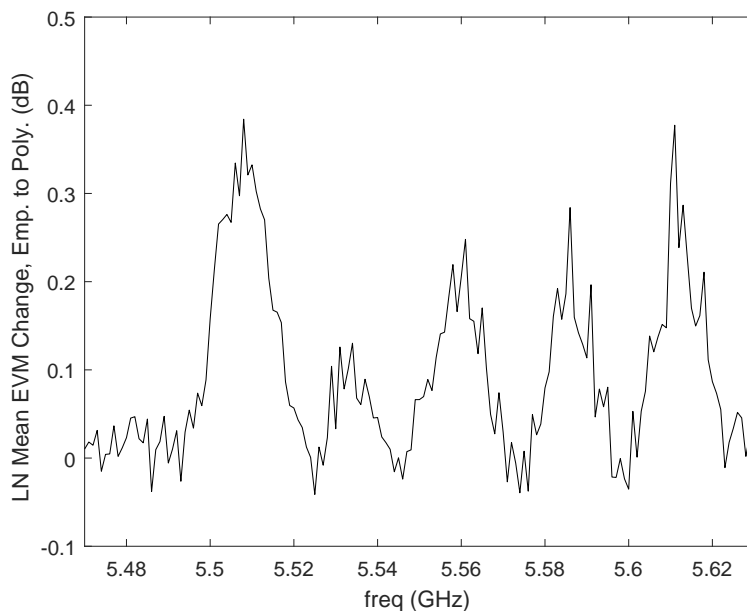


Figure 5.37: Increase of LN Mean EVM From Emp. to Model vs. Freq., Probe 4 Band 3

5.6 Conclusions

A complete channel model in terms of receiver position, probe number, and frequency is the result of the application of the methods contained within this chapter to a set of broadband spatial channel measurements. The frequency and probe is mapped to a modeled band, a set of spatial attribute functions for that band is scaled to the selected frequency and evaluated at the receiver position, and then multiplied by coefficients calculated as a function of frequency. This description of the channel can be evaluated at any position in the modeled test zone, at any frequency in the range of analysis. In addition, the residual of nearby measurement points can be used in conjunction with a statistical model with parameters calculated as a function of frequency to estimate the residual at the receiver position, further refining the channel estimate.

While this model is limited to vertically-polarized dipoles along a specific plane in the test zone, it could be easily extended to include three-dimensional sampling of a test zone, orthogonal receiver dipole polarizations, additional probe positions, etc. Each added item will add an extra dimension to the model space and will require exponentially more measurement points. Without a multi-port VNA, an automated receiver positioning system, and significant computing power for data processing, such additional complexity may make this added complexity infeasible.

In the next chapter, this model is used in the generation of a MIMO channel with receiver antennas at arbitrary positions in the test zone, using the channels modeled from each of the four probes, over the entire 5 GHz WiFi frequency range. An evaluation of capacity and spatial correlation of arbitrary DUT sizes and configurations can be performed over the entire test zone to predict DUT performance within the chamber.

CHAPTER 6

Application of Small Chamber Model to MIMO Analysis

The purpose of this chapter is to use the channel model developed and tested in the previous two chapters, specifically the model developed using the small anechoic chamber measurement set, in an analysis of expected MIMO performance in the small chamber channel. The contribution of this chapter is to show how our channel model can be used in standard MIMO analysis. This chapter revisits the channel magnitude and phase in addition to illustrating the broadband Channel Impulse Response (CIR) (Sec. 6.1), then concisely applies this model to investigate spatial correlation in the test zone for each of the four separate probe channels (Sec. 6.2). Also, 4×4 MIMO wideband capacity is investigated over the small chamber test zone as a function of DUT center position using 4 antenna DUTs. This analysis is performed for several DUT antenna spacings (Sec. 6.3).

6.1 Small Anechoic Chamber Channel and Impulse Response

In a small anechoic chamber, such as the one utilized for a measurement campaign as in the previous chapter, each probe antenna and receiver antenna pair forms a broadband SISO channel. This channel, as modeled in the previous chapter, is a function of frequency and receiver position, $H(f, x, y)$. Figs. 6.1 and 6.2 illustrate a realization of the model for

probe one at a fixed $f = 5.15$ GHz (magnitude and phase respectively), with more densely sampled X and Y positions in the test zone than in the measurement campaign.

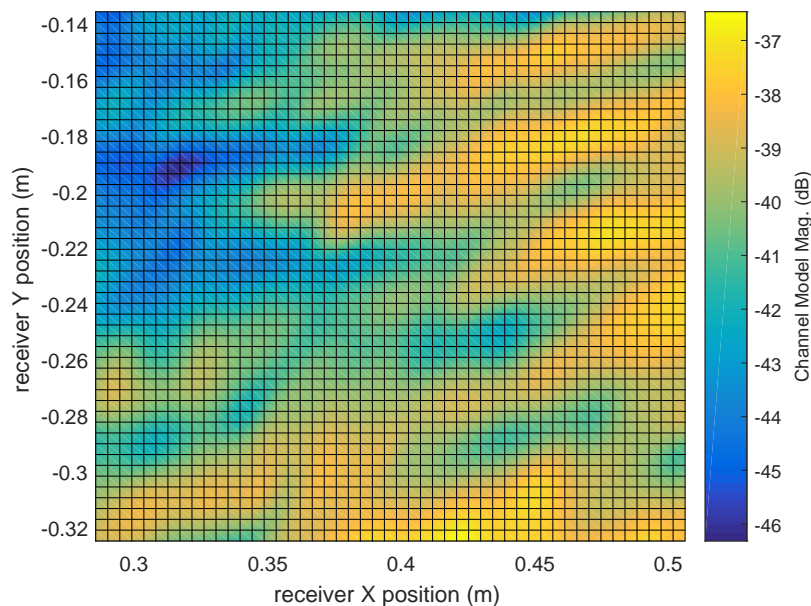


Figure 6.1: Probe One (Lower Right) Channel Model Mag. Over Test Zone

In addition to observing the model for a fixed frequency and observing magnitude and phase over X and Y positions, the channel can be observed for a fixed (X, Y) position, varying frequency. This frequency response for a fixed (X, Y) can be considered a transfer function $H(f)$. This transfer function at (X, Y) can then be transformed from the frequency domain to the time domain to obtain a Channel Impulse Response (CIR), $h(t)$. If the transfer function $H(f)$ is evenly sampled with N complex samples over the bandwidth of the channel model (in our model from 5.15 GHz to 5.725 GHz, a bandwidth of 575 MHz), then the sampled frequency response is converted to the CIR using the following procedure from [58]:

1. Discard the final frequency domain sample in the sampled bandwidth B , leaving $N - 1$ samples from f_{min} to $f_{max} - \frac{B}{N-1}$

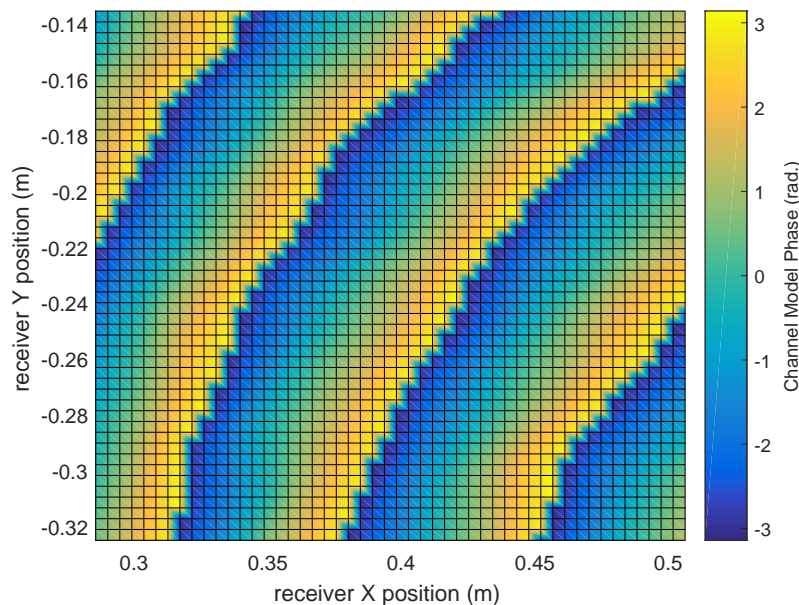


Figure 6.2: Probe One (Lower Right) Channel Model Phase Over Test Zone

2. Perform an IFFT shift to rearrange the $N - 1$ frequency domain samples to prepare the data for an inverse fast Fourier transform (IFFT).
3. Perform an IFFT on the shifted frequency domain samples.
4. Perform a phase shift in the time domain by $e^{j2\pi f_c}$, where f_c is the center frequency of the sampled frequency band ($f_c = f_{min} + \frac{B}{2}$). This is the equivalent to shifting the passband spectrum to the baseband spectrum. The result is the CIR.
5. Calculate the time domain sample time, $t_R = \frac{1}{B}$.

In the end, this entire procedure is encapsulated in a single expression for the CIR $h(t)$ sampled at multiples of t_R , $h(nt_R) = \text{ifft}(\text{ifftshift}[H(1 : (N - 1))]) \cdot e^{-j2\pi f_c}$ [58]. The command `ifft` performs an inverse fast Fourier transform, while `ifftshift` shifts the order of the

first and second halves of the data array to present the frequency response in the expected order to the ifft procedure.

The CIR magnitude can be converted to dB, and normalized such that the peak of the CIR is equal to 0dB. A CIR that decays gradually is indicative of a multipath-rich environment. Smaller peaks after the initial peak can indicate strong multipath clusters that have a delayed arrival relative to a line of sight (LOS) component (or relative to other clusters). Figs. 6.3 - 6.6 illustrate the CIR generated from the channel model for a receiver at the chamber center for each of the four probes.

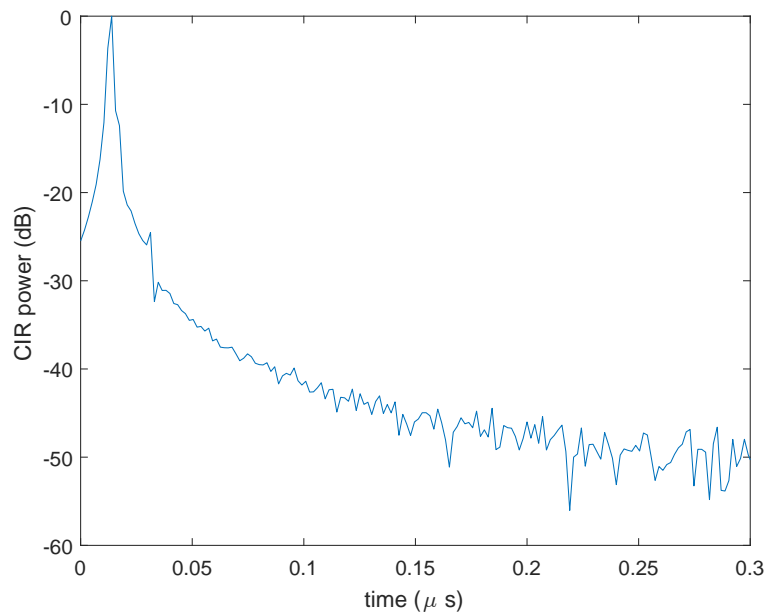


Figure 6.3: Probe One Channel Impulse Response at Chamber Center

All four CIR plots indicate a sharp peak with rapid decay, with very subtle features shortly after the peak at a level of about -15 to -28 dB, potentially indicating a couple of highly-attenuated multipath components. As the absorbing material is rated to attenuate reflections by about -20 dB, and all multipath distances are extremely short and thus would

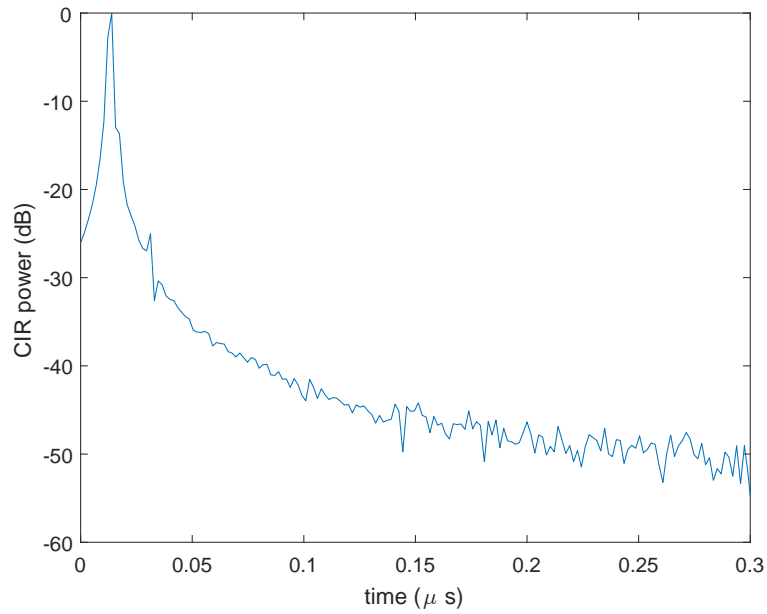


Figure 6.4: Probe Two Channel Impulse Response at Chamber Center

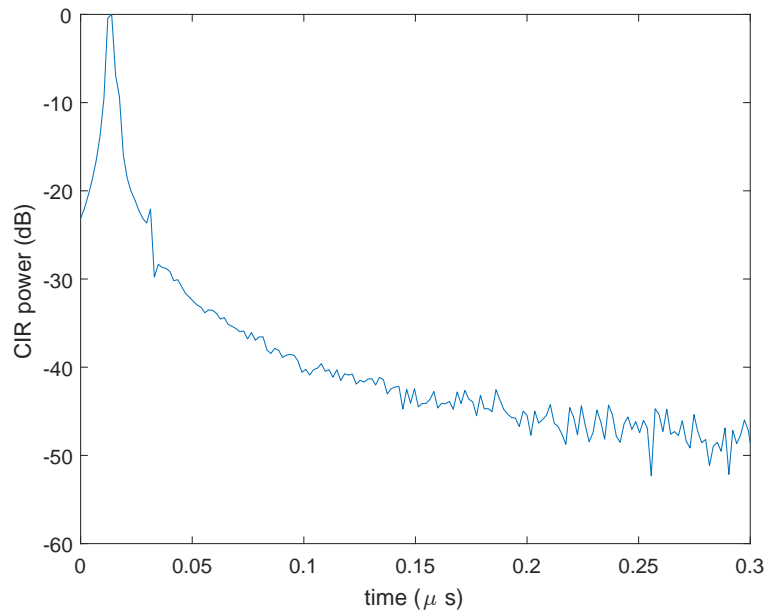


Figure 6.5: Probe Three Channel Impulse Response at Chamber Center

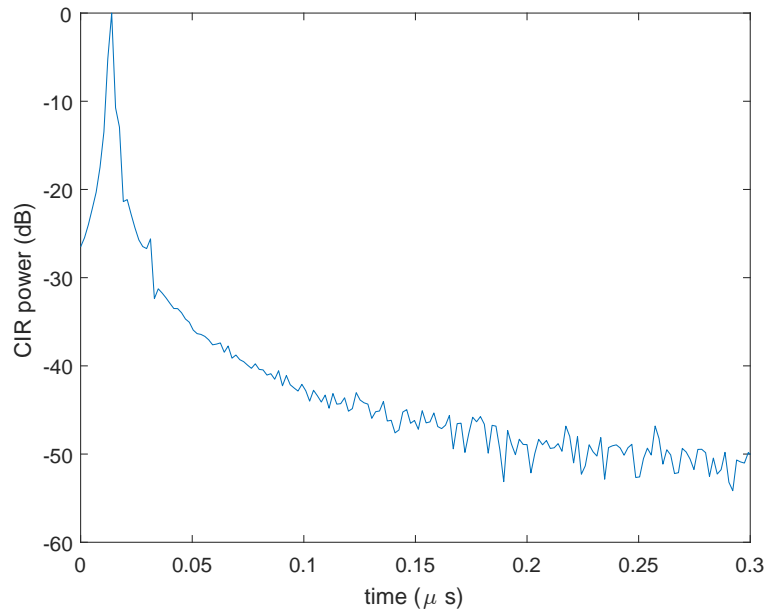


Figure 6.6: Probe Four Channel Impulse Response at Chamber Center

have travel time nearly as short as the LOS component, the observed features are as expected.

The CIR can be used to estimate an important characteristic of MIMO channel performance, spatial correlation, which is explained in the following section.

6.2 Small Anechoic Chamber Spatial Correlation Analysis

An analysis of spatial correlation is an important tool in understanding the nature and expected performance of a MIMO channel. As spatial correlation increases between elements at the transmitter and/or receiver of a MIMO system, the rank of the MIMO channel matrix is reduced (as elements in channel matrix rows and/or columns become correlated and have less variation), and the capacity of the channel decreases.

In the literature, it is common to utilize a sampled or simulated CIR to obtain spatial correlation. Kafle et al. specify an equation (6.1) to calculate receiver wideband spatial correlation $r_{i,j}^{RX}$ given the impulse responses at two receiver locations (i and j) from transmitter m , notated h_{im} and h_{jm} [59].

$$r_{i,j}^{RX} = \frac{E[h_{im}h_{jm}^*] - E[h_{im}]E[h_{jm}^*]}{\sqrt{(E[|h_{im}|^2] - |E[h_{im}]|^2)(E[|h_{jm}|^2] - |E[h_{jm}]|^2)}} \quad (6.1)$$

In this equation E is the expectation operator over CIR delay time, and $*$ is the complex conjugation operator.

To observe the effect of spatial correlation over the entire test zone, spatial correlation was investigated for 31 separation distances ranging from 0 to 4λ . For each separation distance, 30 random pairs of points in the test zone separated by the separation distance (with arbitrary uniformly-random orientation) were selected. At each pair of points, the pair of CIR were evaluated using the procedure described in the previous section. The spatial correlation between the pair of points was calculated using (6.1). The absolute spatial correlation was averaged for all 30 pairs of points at each separation distance. This yielded an empirical estimate of spatial correlation versus spatial separation. This procedure was repeated for the channels of each of the four probes. Figs. 6.7 - 6.10 show the empirical spatial correlation versus spatial separation for each of channels from the four probes. A 5th order polynomial was fit to each of the empirical spatial correlation data sets, and are also included in these plots.

All channels have very similar spatial correlation versus separation, with spatial correlation slowly decreasing from 1 to about 0.7 or 0.8 at a separation of 4λ . This behavior is typical of a LOS channel and is similar to the receiver spatial correlation plot for an indoor

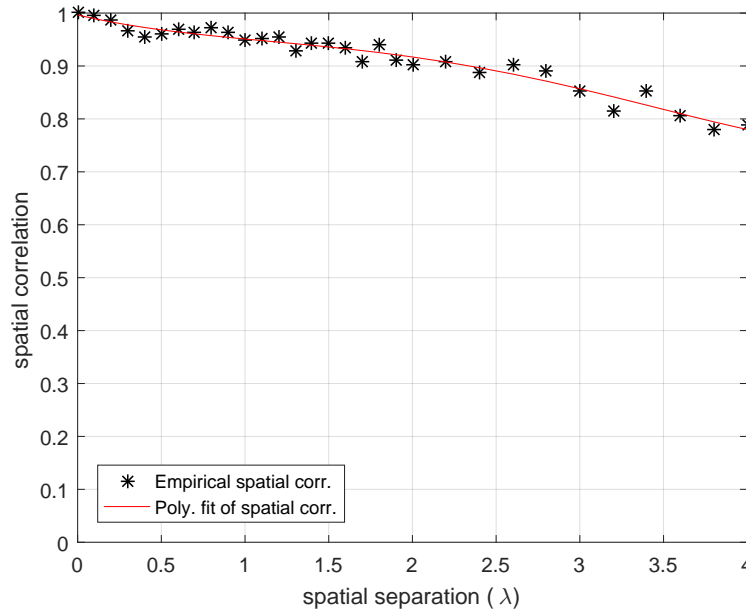


Figure 6.7: Probe One, Empirical and Polynomial Fit Spatial Correlation vs. Separation

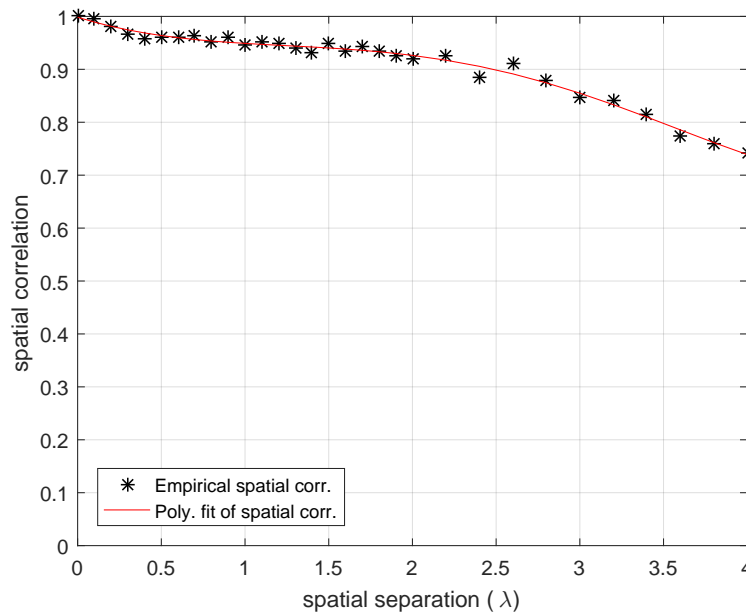


Figure 6.8: Probe Two, Empirical and Polynomial Fit Spatial Correlation vs. Separation

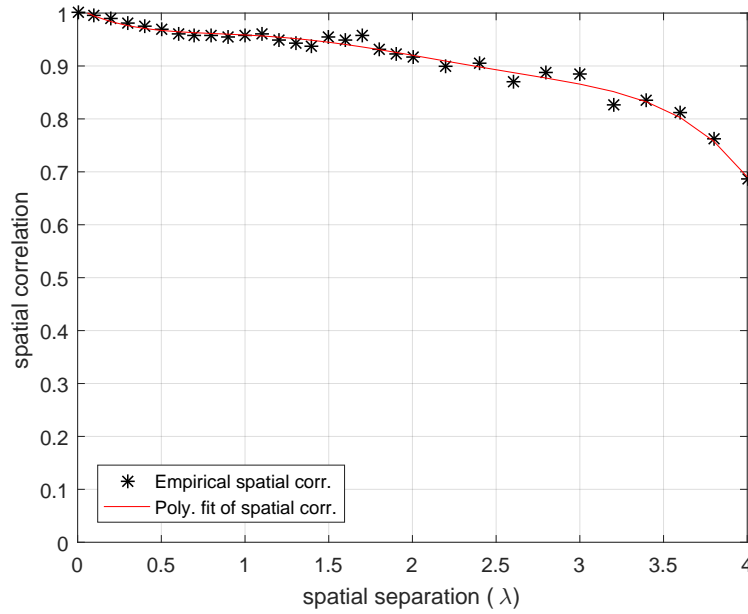


Figure 6.9: Probe Three, Empirical and Polynomial Fit Spatial Correlation vs. Separation

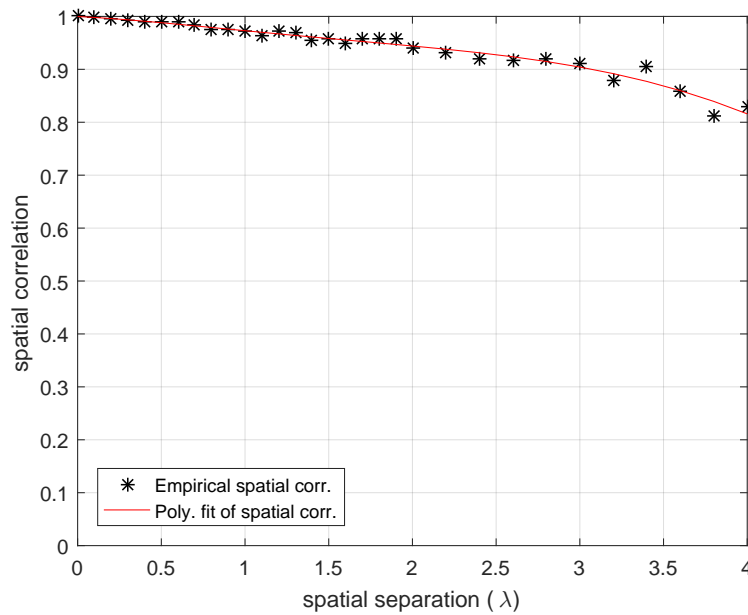


Figure 6.10: Probe Four, Empirical and Polynomial Fit Spatial Correlation vs. Separation

LOS environment in [59], which also decreases from 1 to just below 0.8 between 0 and 4λ . This would indicate that the channel inside the small anechoic chamber behaves like an LOS dominant channel.

Also of interest, is the distribution of spatial correlation for fixed separations. The empirical spatial correlation was calculated as a mean of 30 random location pairs in the chamber. Rather than averaging the 30 spatial correlations calculated for a set of constant separation, the distribution of those 30 spatial correlation values can be plotted as a CCDF for each probe and a selected set of fixed separations. Figs. 6.11 - 6.14 each show the CCDF for $\frac{\lambda}{4}$, $\frac{\lambda}{2}$, λ and $\frac{3\lambda}{2}$ for the channel corresponding to a probe.

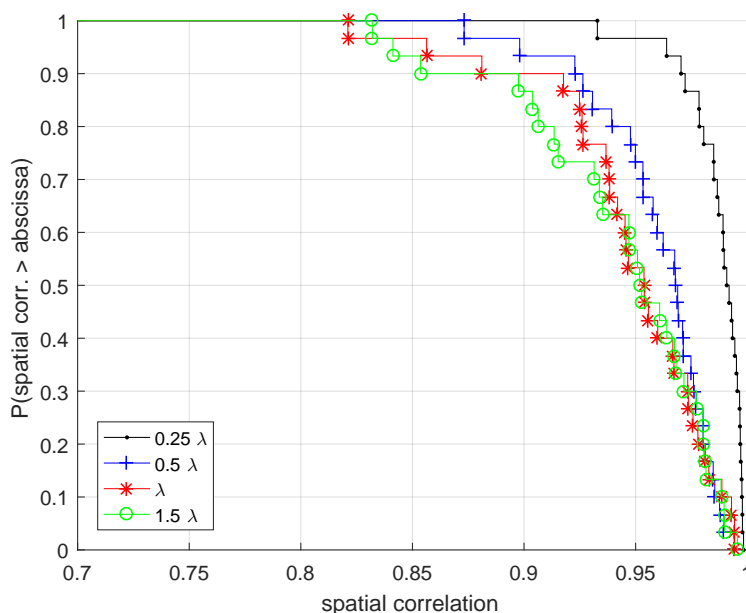


Figure 6.11: Probe One, Empirical Spatial Correlation CCDFs vs. Separation

In all four plots, the CCDF for $\frac{\lambda}{4}$ is the right-most CCDF curve. For probes two through four, one hundred percent of the observed spatial correlations were above 0.95, and for all four probes, one hundred percent of the spatial correlations were above 0.925. For probe

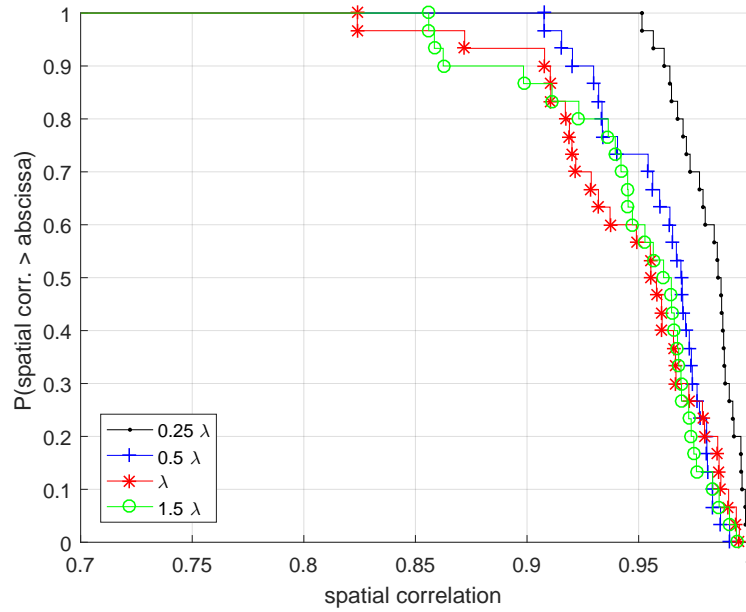


Figure 6.12: Probe Two, Empirical Spatial Correlation CCDFs vs. Separation

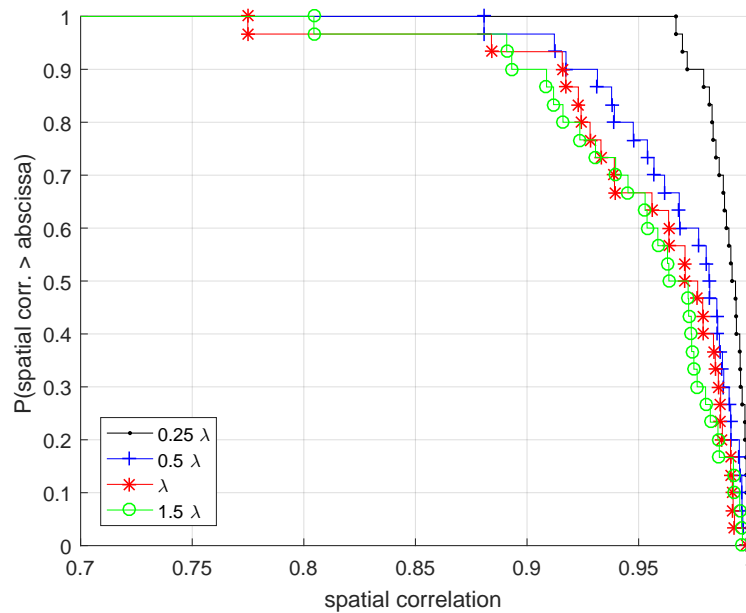


Figure 6.13: Probe Three, Empirical Spatial Correlation CCDFs vs. Separation

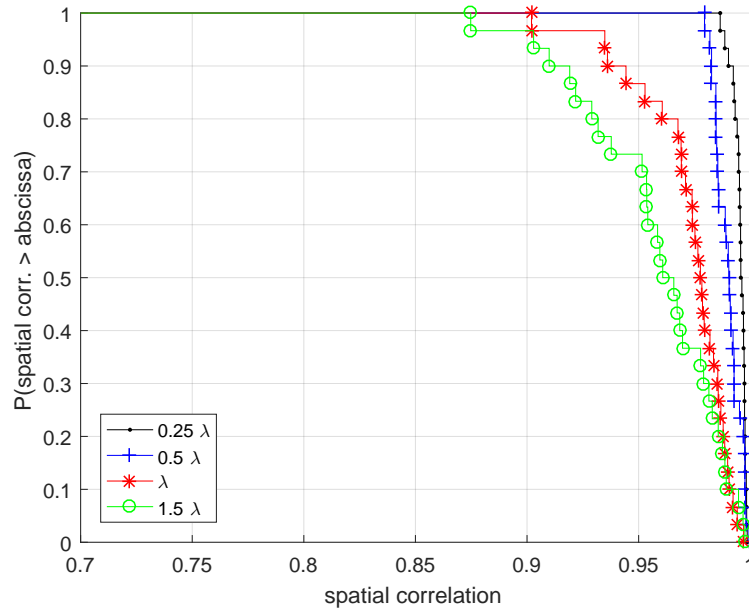


Figure 6.14: Probe Four, Empirical Spatial Correlation CCDFs vs. Separation

four in Fig. 6.14, the $\frac{\lambda}{2}$ CCDF curve was nearly as high as the $\frac{\lambda}{4}$ curve. For all probes, in almost all cases the $\frac{\lambda}{2}$ CCDF curve was the second right-most CCDF curve throughout. One hundred percent of spatial correlations for $\frac{\lambda}{2}$ were above 0.87 for all four probes.

With the exception of probe four, the CCDF curves of λ and $\frac{3\lambda}{2}$ all closely tracked each other, with the $\frac{3\lambda}{2}$ CCDF and the λ CCDF curves crossing each other in multiple places. Only probe four had strictly-ordered CCDF curves of $\frac{3\lambda}{2}$ to $\frac{\lambda}{4}$ from left to right for all probabilities.

The following section will investigate the effect of DUT antenna separation and size on MIMO capacity.

6.3 Wideband MIMO Capacity Using Small Chamber Channel Model

The instantaneous wideband MIMO capacity formula (2.8) can be used in conjunction with our channel model for each probe. For a 4×4 MIMO system ($M_{Rx} = M_{Tx} = 4$), four receiver antenna locations are selected in the test zone, and the channel $h_{i,j,k}$ from each of the four probe antennas (j) is calculated to each of the four receiver locations (i) at a selection of frequencies (k , with spacing Δf over a frequency range W , forming F frequency samples). All values of $h_{i,j,k}$ are used to populate $\mathbf{H}[f]$, which is then normalized as in (2.9). An arbitrary SNR ρ is chosen for the purposes of analysis (often chosen as the linear equivalent of 10 dB, 15 dB, or 20 dB in the literature).

6.3.1 MIMO Capacity Analysis System Description

For analysis, 20 frequencies evenly-spaced from 5.15 GHz to 5.725 GHz were selected. Four types of simulated square DUT antenna arrays were chosen, with antennas located on the corner of a square. The four square sizes were chosen to be $0.25\lambda \times 0.25\lambda$, $0.5\lambda \times 0.5\lambda$, $\lambda \times \lambda$, and $1.5\lambda \times 1.5\lambda$, allowing for the MIMO capacity to reflect the spatial correlations investigated in the previous section (as the majority of antenna pairs of the receiver will have a separation equal to a side length of the square).

Each simulated DUT was moved along an 8×8 grid of DUT center locations within the test zone, allowing the DUT to fully cover the entire test zone over the course of the 64 measurements. Due to varying DUT sizes, the grid of center locations had to decrease in size as DUT dimensions increased to allow the simulated DUT to remain in the test zone at all times. As a result, plots of capacity versus simulated DUT center location will have

smaller X and Y dimensions for simulated DUTs with increased dimensions.

6.3.2 MIMO Capacity and Eigenvalue Results

Figs. 6.15 - 6.18 show the wideband capacity of the four simulated DUT sizes across the test zone. The X and Y coordinates indicate the center position of the simulated DUT where that capacity was calculated.

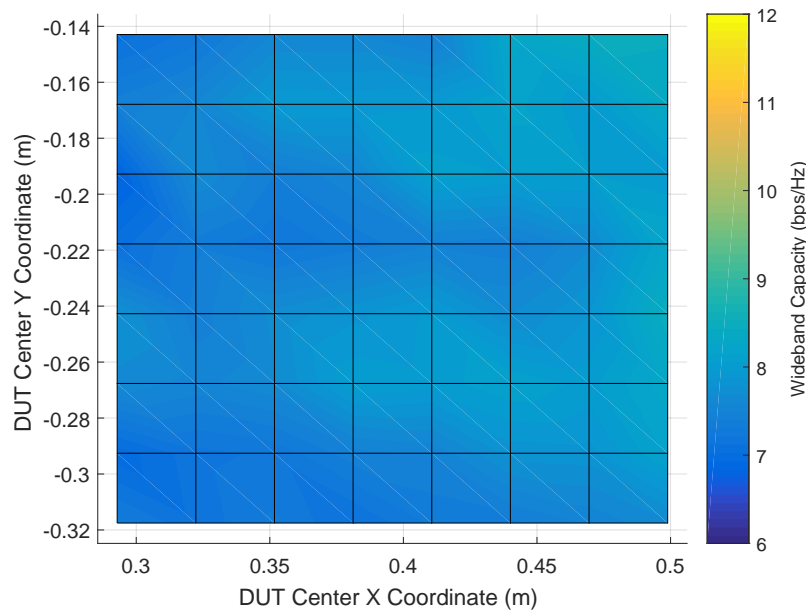


Figure 6.15: $0.25\lambda \times 0.25\lambda$ DUT WB Cap. Vs. DUT Center Pos.

Common trends across all four DUT sizes include greater capacity on the right side of the test zone than the left side, generally lower capacity in the bottom left (front left of the chamber), and capacities across the test zone varying by about 2dB in all cases. The $0.25\lambda \times 0.25\lambda$ DUT as in Fig. 6.15 exhibited a capacity range of approximately 6.8 to 8.5 bps/Hz, the $0.5\lambda \times 0.5\lambda$ DUT as in Fig. 6.16 exhibited a capacity range of 8.4 to 10 bps/Hz, the $\lambda \times \lambda$ DUT as in Fig. 6.17 exhibited a capacity range of 9.2 to 11 bps/Hz, and the

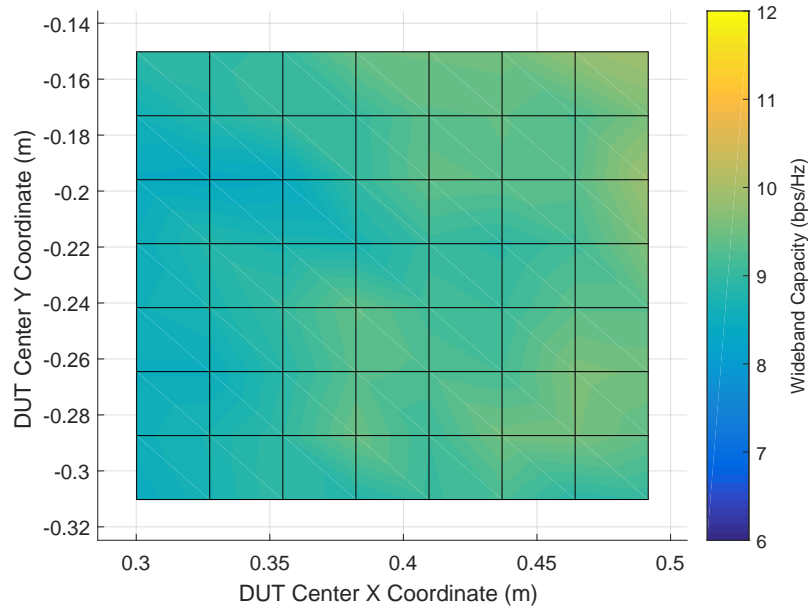


Figure 6.16: $0.5\lambda \times 0.5\lambda$ DUT WB Cap. Vs. DUT Center Pos.

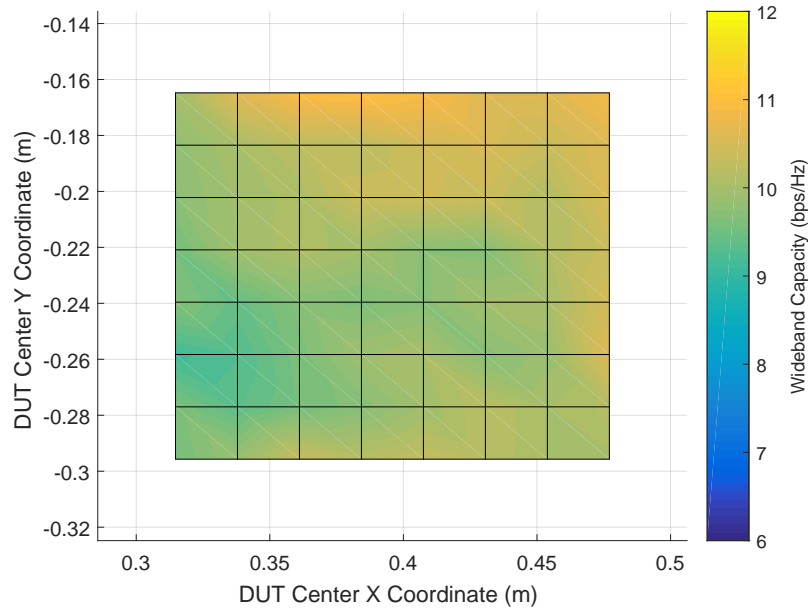


Figure 6.17: $\lambda \times \lambda$ DUT WB Cap. Vs. DUT Center Pos.

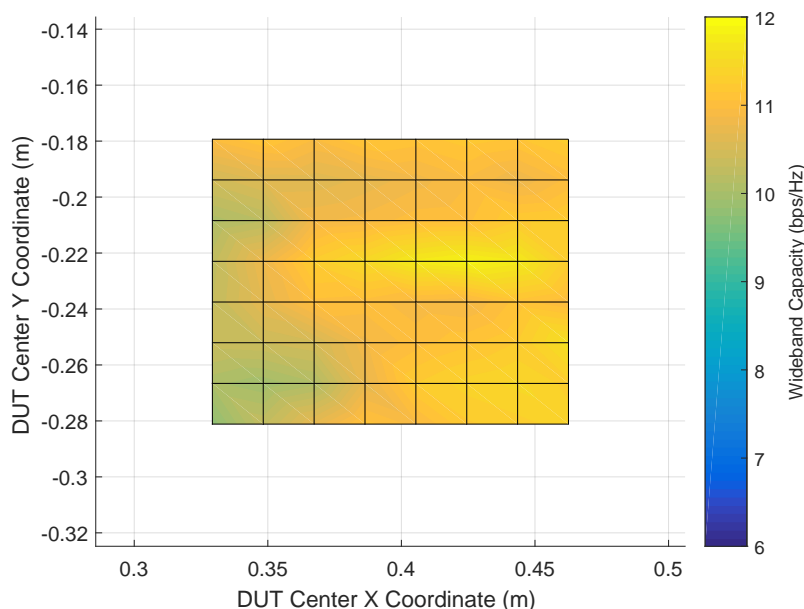


Figure 6.18: $1.5 \lambda \times 1.5 \lambda$ DUT WB Cap. Vs. DUT Center Pos.

1.5×1.5 DUT as in Fig. 6.18 exhibited a capacity range of 9.8 to 11.8 bps/Hz.

A potentially more useful way of observing each set of 64 capacities is to observe them as a CCDF rather than plotted versus center coordinate. Figs. 6.19 - 6.22 are plots of the capacity CCDFs for each of the four simulated DUT configurations. The capacity ranges will remain identical to those observed in the previous four plots, but the distribution of the observed capacities will be apparent.

The $\frac{\lambda}{4} \times \frac{\lambda}{4}$ DUT appears to have a median capacity of 7.7 bps/Hz, the $\frac{\lambda}{2} \times \frac{\lambda}{2}$ DUT has a median capacity of 9.1 bps/Hz, the $\lambda \times \lambda$ DUT has a median capacity of 10 bps/Hz, and the $\frac{3\lambda}{2} \times \frac{3\lambda}{2}$ DUT has a median capacity of 11 bps/Hz. The increase in capacity by increasing a DUT size from $\frac{\lambda}{4} \times \frac{\lambda}{4}$ to $\frac{\lambda}{2} \times \frac{\lambda}{2}$ is more pronounced than further increases in the MIMO channel present in the small anechoic chamber.

One additional method of characterizing the MIMO channel is to observe the distribution

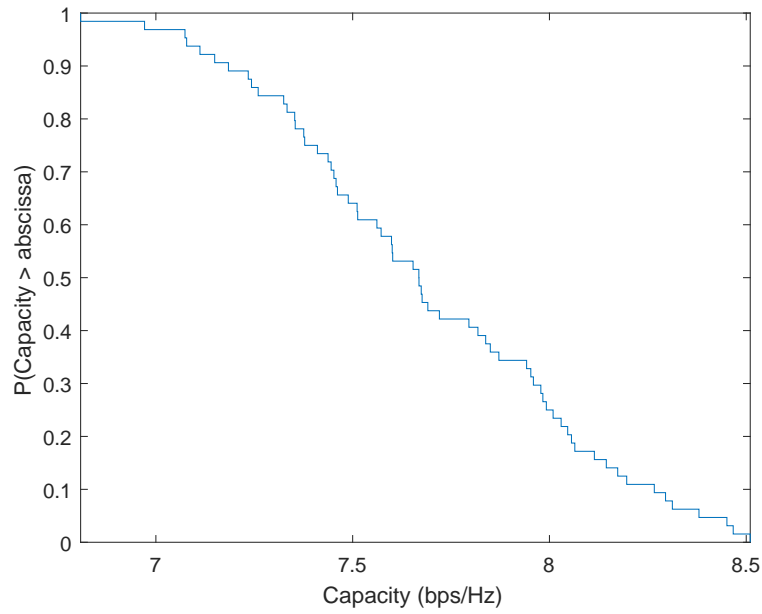


Figure 6.19: $0.25 \lambda \times 0.25 \lambda$ DUT WB Cap. CCDF

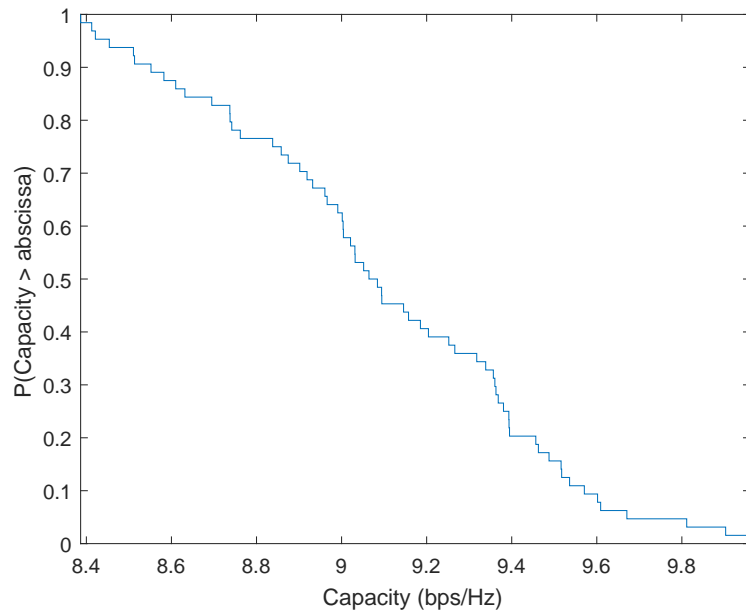


Figure 6.20: $0.5 \lambda \times 0.5 \lambda$ DUT WB Cap. CCDF

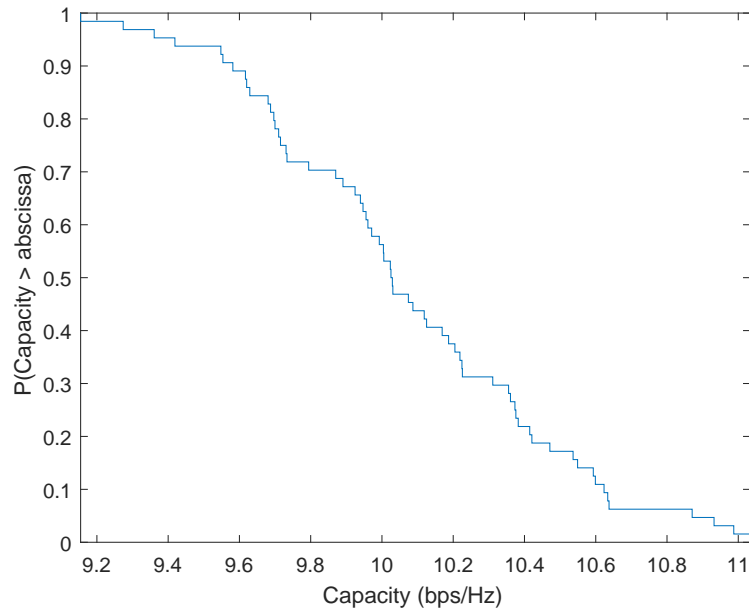


Figure 6.21: $\lambda \times \lambda$ DUT WB Cap. CCDF

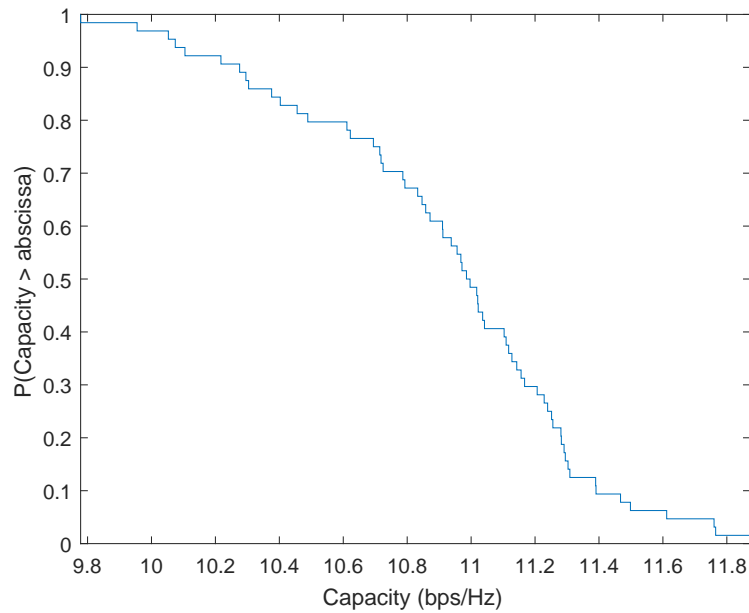


Figure 6.22: $1.5 \lambda \times 1.5 \lambda$ DUT WB Cap. CCDF

of its eigenvalues [60]. An eigenvalue decomposition of an $N \times N$ channel matrix will yield N eigenvalues. The number of non-zero eigenvalues of the channel matrix \mathbf{H} , which is also the rank of \mathbf{H} , indicates the number of spatial degrees of freedom present in the channel [13]. Greater spatial degrees of freedom translate into higher MIMO capacities, especially in channels where all N eigenvalues are nearly-identical. Practically, eigenvalue decomposition will likely produce N non-zero eigenvalues in a real channel in almost all circumstances, however if one or more of these is significantly lower than others and/or nearly equal to zero, then the number of spatial degrees of freedom is effectively lower than N .

Using the channel data generated for the previous set of plots, for each simulated DUT we have 20 frequencies \times 64 center positions = 1280 narrowband MIMO channel matrices. If we perform an eigenvalue decomposition to obtain the eigenvalues of each, normalize the eigenvalues such that their linear sum is equal to 1, and then sort the eigenvalues by size, we can observe a CCDF for each of the four eigenvalues for each simulated DUT configuration. This allows us to evaluate the distribution of each eigenvalue, and determine if it is too low to be a spatial degree of freedom for that simulated DUT in the chamber. Figs. 6.23 - 6.26 each plot the CCDF of eigenvalues 1 through 4 (ϵ_1 to ϵ_4 ; the variable ϵ will be used for eigenvectors instead of the traditional λ to avoid confusion with wavelength) for each of the four simulated DUT configurations.

Fig. 6.23, the $\frac{\lambda}{4} \times \frac{\lambda}{4}$ DUT, has a ϵ_4 that is likely at least 20 dB smaller than ϵ_1 and ϵ_3 that is likely 13 dB smaller than ϵ_1 . Even ϵ_2 is likely at least 5 dB smaller than ϵ_1 , indicating that the channel for the $\frac{\lambda}{4} \times \frac{\lambda}{4}$ DUT practically only has about one or two degrees of spatial freedom at most. This is a poorly-conditioned channel matrix, and as a result the capacity will be low, which is exactly what was observed in the corresponding capacity CCDF Fig. 6.19.

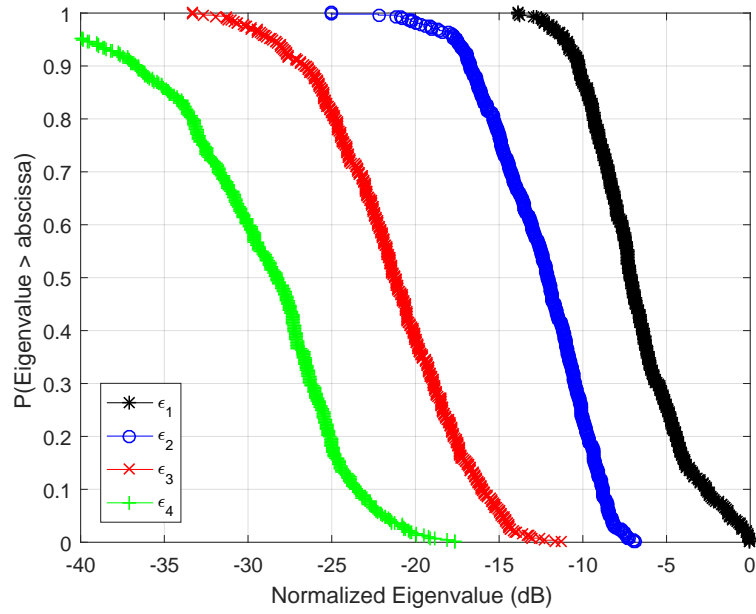


Figure 6.23: $\frac{\lambda}{4} \times \frac{\lambda}{4}$ DUT Channel Eigenvalue CCDF

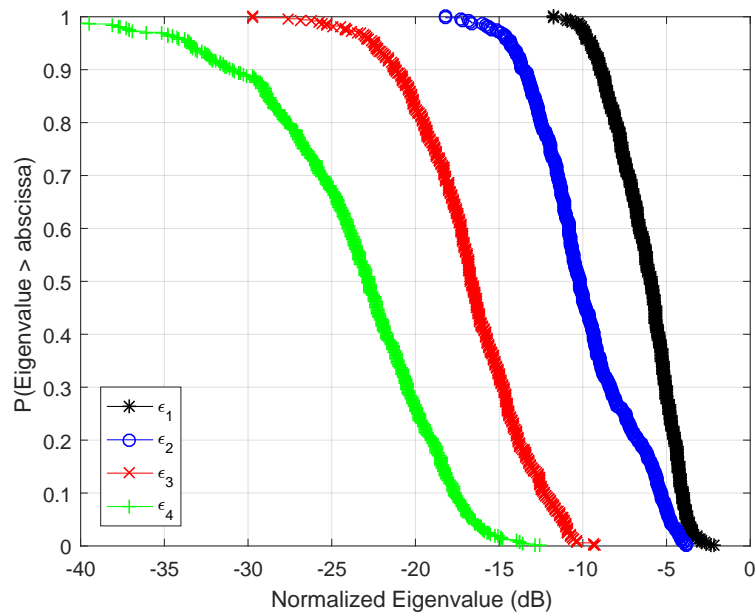


Figure 6.24: $\frac{\lambda}{2} \times \frac{\lambda}{2}$ DUT Channel Eigenvalue CCDF

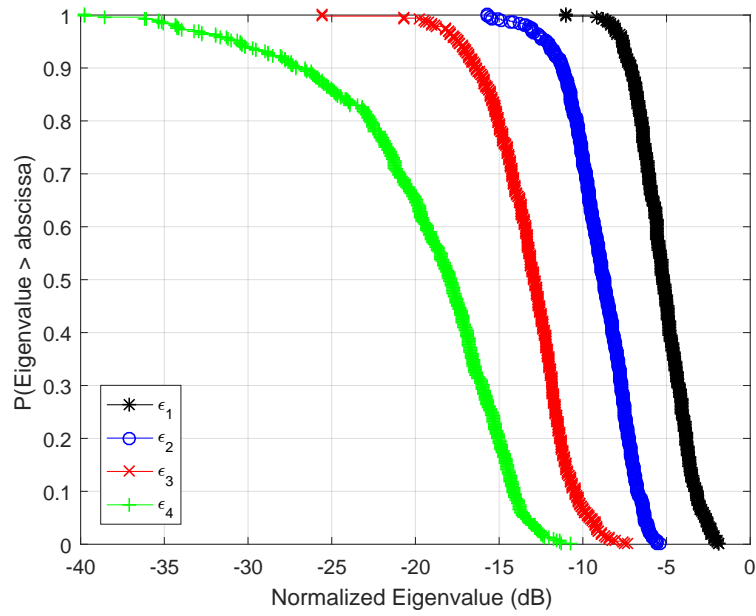


Figure 6.25: $\lambda \times \lambda$ DUT Channel Eigenvalue CCDF

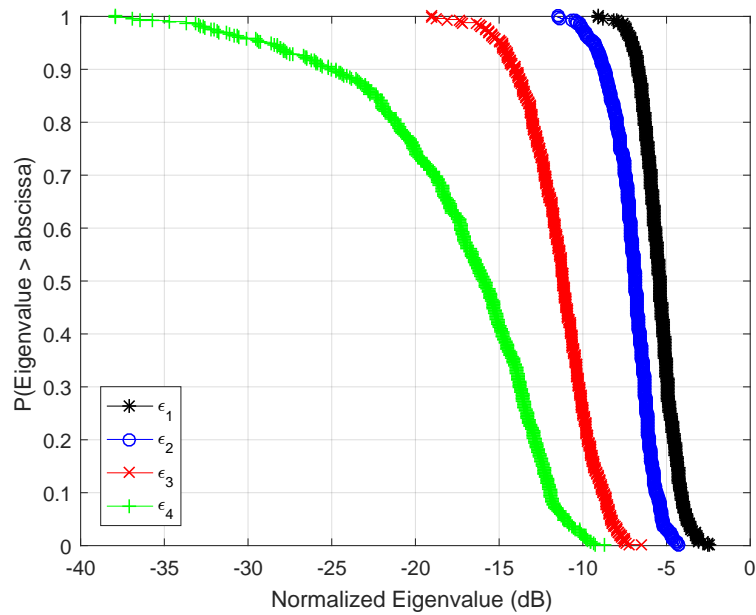


Figure 6.26: $\frac{3\lambda}{2} \times \frac{3\lambda}{2}$ DUT Channel Eigenvalue CCDF

Fig. 6.24, the $\frac{\lambda}{2} \times \frac{\lambda}{2}$ DUT, still has a ϵ_4 that is likely 15 dB lower than ϵ_1 . ϵ_3 is likely about 11 dB smaller than ϵ_1 , and ϵ_2 is likely about 4dB smaller or less. This is still a relatively poorly-conditioned channel matrix with about two or possibly three spatial degrees of freedom.

Fig. 6.25 shows ϵ_4 still too low to be considered a degree of freedom, but has ϵ_3 and ϵ_2 closing in on ϵ_1 . This indicates a channel that is closer to three spatial degrees of freedom, even though the fact that the three eigenvalues are not close in value indicates that this channel matrix still would not be well-conditioned even for a 3×3 MIMO channel.

Finally, Fig. 6.26 shows the ϵ_2 CCDF very close to the ϵ_1 CCDF. ϵ_3 is also slightly greater than in the previous plot. ϵ_4 is also higher, but is still close to being excluded as a spatial degree of freedom. This channel could therefore be considered to have three spatial degrees of freedom or possibly even four, with better conditioning than that of all smaller DUT configurations.

This analysis has shown the usefulness of the contributed channel model in extensively analyzing the MIMO channel characteristics of a system such as the small anechoic chamber. This information provides feedback to the MIMO performance of such a chamber, helps validate whether this system meets the criteria of standardized MIMO OTA testing, and can be used to help improve the chamber design to better meet the needs of a low-cost MIMO OTA testing solution.

6.4 Conclusions

In this chapter, we have investigated how the small anechoic chamber MIMO channel, modeled in the previous two chapters, performs by metrics including spatial correlation, capacity, and channel Eigenvalue distributions. The channel exhibits high spatial correlation

even at separations up to 4λ , indicating that the MIMO channel in the chamber is LOS-dominant. Wideband capacity and eigenvalues, calculated over the entire test zone and frequency range of the model for multiple simulated DUT sizes, further supported the notion that the chamber MIMO channel is primarily LOS, yielding eigenvalue distributions that even with $\frac{3\lambda}{2}$ spacing never truly yielded channel matrices that were full-rank in a 4×4 system or well-conditioned. This analysis of the MIMO performance of a modeled small anechoic chamber channel simultaneously has showed the usefulness of our channel model and how it can be applied to performance evaluation of real-world OTA test solutions. Future work may include investigating the chamber MIMO channel for other DUT configurations and orientations, including ULA, rectangular arrays, and larger-dimension arrays.

CHAPTER 7

Conclusion and Future Work

This dissertation has provided an analysis of near-field MIMO systems of the type that are present in a small anechoic chamber testing environment. This analysis has included a feasibility study of standard-compliant electric field generation in a small anechoic chamber for MIMO-OTA testing, investigating parameters such as chamber size and probe antenna array size and spacing. In addition, and more significantly, this dissertation contributed a novel method of modeling a measured or numerical near-field channel using a sum of weighted joint spatial attribute functions plus a statistically-modeled residual refinement term based on neighboring measurements. Model parameters for a series of narrowband models were fit to functions of frequency, thus producing a wideband channel model. This modeling technique was used for a measurement campaign of a small anechoic chamber, and the resulting models were utilized in a MIMO system analysis of the small anechoic chamber.

The modeling method in this dissertation achieved an accuracy of below -15 dB error vector magnitude for at least 84 percent of measurement locations in the defined test zone for all frequencies analyzed. This accuracy is prior to application of the modeled residual term which further increases model accuracy, particularly at locations near measurement points.

An investigation into MIMO system performance of a small anechoic chamber using a model obtained from a measurement campaign showed that the channel in the chamber exhibited high spatial correlation, generally greater than 0.8 for distances of 4λ or less. This spatial correlation is indicative of a highly line of sight environment, one in which

MIMO systems exhibit limited capacity gain from spatial diversity. Further investigation of capacity and eigenvalue decomposition of the MIMO channel matrix versus a range of simulated DUT antenna separations over the test zone of the chamber showed that DUTs with antenna spacing of $\frac{\lambda}{4}$ exhibited approximately a single degree of spatial freedom, while a separation of $\frac{3\lambda}{2}$ exhibited around 3 degrees of spatial freedom, though the third eigenvalue was still well below the first two, yielding a poorly-conditioned channel matrix.

The results of this dissertation can be used to inform the design or refinement of a small anechoic chamber environment, with the goal of reducing spatial correlation of the system. It can also be used to quantify expected DUT performance in a small anechoic chamber, allowing for test metrics and repeatable testing design.

Future work expanding on these results includes expanding the model to include a larger test zone in the chamber, extending the model to additional frequency bands for other wireless technologies, expanding the test zone to three dimensions to model the channel as a three-dimensional function of space and frequency, investigating the effect of receiver polarization on the channel and incorporating this information into the channel model. Also, a measurement campaign varying transmitter position can be performed to investigate transmitter spatial correlation, and potentially extend the model as a function of both receiver and transmitter location, rather than discrete models for single transmitter locations. Finally, the effects of coupling between multiple DUT antennas on the channel model can be investigated, modeled, and incorporated into this channel model. Due to the extremely large possible configurations and electromagnetic properties of a DUT, the challenges of deciding a proper way to incorporate this into a channel model that will be applicable to any DUT in the chamber proved beyond the scope of this dissertation.

References

- [1] 3GPP releases. [Online]. Available: <http://www.3gpp.org/specifications/releases>
- [2] Y. Tak and S. Nam, "Mode-based computation method of channel characteristics for a near-field MIMO," *IEEE Antennas and Wireless Propagation Letters*, vol. 10, pp. 1170–1173, 2011.
- [3] H. Hirayama, G. Matsui, N. Kikuma, and K. Sakakibara, "Improvement of channel capacity of near-field MIMO," *Proceedings of the Fourth European Conference on Antennas and Propagation, IEEE*, pp. 1–4, April 2010.
- [4] Octoscope, Inc. octobox OBS-14 and OBS-15 high gain antenna array datasheet. [Online]. Available: https://www.octoscope.com/English/Collaterals/Documents/octoBox_OBS-14_OBS-15_High-Gain_Antenna_Datasheet.pdf
- [5] Pasternack. PE51083 rubber duck antenna datasheet. [Online]. Available: <https://www.pasternack.com/images/ProductPDF/PE51083.pdf>
- [6] Keysight Technologies. Keysight E5063A ENA vector network analyzer datasheet. [Online]. Available: <https://literature.cdn.keysight.com/litweb/pdf/5991-3614EN.pdf?id=2424803>
- [7] R. Bajaj, S. Bates, B. P., K. Bennett *et al.* Connecting america: The national broadband plan. [Online]. Available: <https://transition.fcc.gov/national-broadband-plan/national-broadband-plan.pdf>

REFERENCES

- [8] The path to 5G: as much evolution as revolution. [Online]. Available: http://www.3gpp.org/news-events/3gpp-news/1774-5g_wiseharbour
- [9] Unleashing 5G with 'High Band' Spectrum. [Online]. Available: <http://www.ctia.org/docs/default-source/default-document-library/high-band-spectrum-april-2016.pdf>
- [10] J. Xu, D. Goeckel, and R. Janaswamy, "The capacity of MIMO systems with increasing SNR by electromagnetic analysis," *Wireless Communications, IEEE Transactions on*, vol. 8, no. 9, pp. 4752–4761, 2009.
- [11] N. Costa and S. Haykin, *Multiple-Input Multiple-Output Channel Models: Theory and Practice*. Wiley, 2010.
- [12] J. Tefft and N. Kirsch, "Small anechoic chambers for MIMO-OTA testing," *IEEE Transactions on Instrumentation and Measurement (ready for submission)*, Aug. 2016.
- [13] D. Tse and P. Viswanath, *Fundamentals of Wireless Communication*. Cambridge University Press, 2005.
- [14] J. Foschini and M. J. Gans, "On the limits of wireless communications in a fading environment when using multiple antennas," *Wireless Personal Communications*, vol. 6, pp. 315–335, March 1998.
- [15] A. Goldsmith, *Wireless Communications*. Cambridge University Press, 2005.
- [16] R. Janaswamy, "Effect of element mutual coupling on the capacity of fixed length linear arrays," *IEEE Antennas and Wireless Propagation Letters*, vol. 1, no. 1, pp. 157–160, 2002.

REFERENCES

- [17] H.-S. Lui, H. T. Hui, and M. S. Leong, “A note on the mutual-coupling problems in transmitting and receiving antenna arrays,” *IEEE Antennas and Propagation Magazine*, vol. 51, no. 5, pp. 171–176, Oct 2009.
- [18] E. Hansen, *Spherical Near-Field Antenna Measurements*. Peter Peregrinus Ltd., 1988.
- [19] S. Orfanidis. Electromagnetic waves and antennas. [Online]. Available: <http://www.ece.rutgers.edu/~orfanidi/ewa/>
- [20] 3rd Generation Partnership Project (3GPP), *Inter-Lab/Inter-Technique OTA Performance Comparison Testing for MIMO Devices*. Work Group Document: MOSG120521R9, 2013.
- [21] W. Fan, X. Carreno Bautista de Lisbona, F. Sun, J. Nielsen, M. Knudsen, and G. Pedersen, “Emulating spatial characteristics of MIMO channels for OTA testing,” *Antennas and Propagation, IEEE Transactions on*, vol. 61, no. 8, pp. 4306–4314, 2013.
- [22] G. de la Roche, A. Alayn-Glazunov, and B. Allen, *LTE-Advanced and Next Generation Wireless Networks: Channel Modelling and Propagation*. Wiley, 2012.
- [23] C. Lotback Patane, A. Skarbratt, R. Rehammar, and C. Orlenius, “On the use of reverberation chambers for assessment of MIMO-OTA performance of wireless devices,” in *Antennas and Propagation (EuCAP), 2013 7th European Conference on*, 2013, pp. 101–105.
- [24] I. Carton Llorente, W. Fan, and G. Pedersen, “MIMO-OTA testing in small multi-probe anechoic chamber setups,” *Antennas and Wireless Propagation Letters, IEEE*, vol. PP, no. 99, pp. 1–1, 2015.

REFERENCES

- [25] T. Laitinen, P. Kyösti, T. Jamsa, and P. Vainikainen, “Generation of a field with a laplacian-distributed power azimuth spectrum scattered by a single cluster in a MIMO-OTA test system based on multiple probe antennas,” in *Proceedings of Asia-Pacific Microwave Conference (APMC)*, Dec. 2010.
- [26] J. T. Toivanen, T. A. Laitinen, S. Pivnenko, and L. Nyberg, “Calibration of multi-probe antenna measurement system using test zone field compensation,” in *2009 3rd European Conference on Antennas and Propagation*, March 2009, pp. 2916–2920.
- [27] J. T. Toivanen, T. A. Laitinen, and P. Vainikainen, “Modified test zone field compensation for small-antenna measurements,” *IEEE Transactions on Antennas and Propagation*, vol. 58, no. 11, pp. 3471–3479, Nov 2010.
- [28] J. T. Toivanen, T. A. Laitinen, V. M. Kolmonen, and P. Vainikainen, “Reproduction of arbitrary multipath environments in laboratory conditions,” *IEEE Transactions on Instrumentation and Measurement*, vol. 60, no. 1, pp. 275–281, Jan 2011.
- [29] P. Kyösti, J. P. Nuutinen, and T. Jämsä, “MIMO OTA test concept with experimental and simulated verification,” in *Proceedings of the Fourth European Conference on Antennas and Propagation*, April 2010, pp. 1–5.
- [30] Y. Okano, K. Kitao, and T. Imai, “Impact of number of probe antennas for MIMO OTA spatial channel emulator,” in *Proceedings of the Fourth European Conference on Antennas and Propagation*, April 2010, pp. 1–5.
- [31] P. Kyösti and L. Hentilä, “Criteria for physical dimensions of MIMO OTA multi-probe test setup,” in *2012 6th European Conference on Antennas and Propagation (EUCAP)*, March 2012, pp. 2055–2059.

REFERENCES

- [32] W. Fan, J. . Nielsen, O. Franek, X. Carreño, J. S. Ashta, M. B. Knudsen, and G. F. Pedersen, “Antenna pattern impact on MIMO OTA testing,” *IEEE Transactions on Antennas and Propagation*, vol. 61, no. 11, pp. 5714–5723, Nov 2013.
- [33] W. Fan, F. Sun, P. Kyosti, J. Nielsen, X. Carreno, M. Knudsen, and G. Pedersen, “3d channel emulation in multi-probe setup,” *Electronics Letters*, vol. 49, no. 9, pp. 623–625, April 2013.
- [34] P. Kyösti, T. Jämsä, and J. P. Nuutinen, “Channel modelling for multiprobe over-the-air MIMO testing,” *International Journal of Antennas and Propagation*, vol. 2012, pp. 1–11, Mar 2012.
- [35] A. Khatun, T. Laitinen, V. M. Kolmonen, and P. Vainikainen, “Dependence of error level on the number of probes in over-the-air multiprobe test systems,” *International Journal of Antennas and Propagation*, vol. 2012, p. 6, Mar 2012.
- [36] W. Fan, J. . Nielsen, X. Carreño, O. Franek, M. B. Knudsen, and G. F. Pedersen, “Impact of probe placement error on MIMO OTA test zone performance,” in *Antennas and Propagation Conference (LAPC), 2012 Loughborough*, Nov 2012, pp. 1–4.
- [37] T. Laitinen, J. Toivanen, P. Kyösti, J. P. Nuutinen, and P. Vainikainen, “On a MIMO-OTA testing based on multi-probe technology,” in *Electromagnetic Theory (EMTS), 2010 URSI International Symposium on*, Aug 2010, pp. 227–230.
- [38] W. Fan, X. Carreño, J. . Nielsen, K. Olesen, M. B. Knudsen, and G. F. Pedersen, “Measurement verification of plane wave synthesis technique based on multi-probe MIMO-OTA setup,” in *Vehicular Technology Conference (VTC Fall), 2012 IEEE*, Sept 2012, pp. 1–5.

REFERENCES

- [39] J.-S. Jiang and M. A. Ingram, "Spherical-wave model for short-range MIMO," *IEEE Transactions on Communications*, vol. 53, no. 9, pp. 1534–1541, Sept 2005.
- [40] K. Nishimori, N. Honma, T. Seki, and K. Hiraga, "On the transmission method for short-range MIMO communication," *IEEE Transactions on Vehicular Technology*, vol. 60, no. 3, pp. 1247–1251, March 2011.
- [41] N. Honma, K. Nishimori, T. Seki, and M. Mizoguchi, "Short range MIMO communication," in *2009 3rd European Conference on Antennas and Propagation*, March 2009, pp. 1763–1767.
- [42] N. Gvozdenovic, W. Thompson, M. A. Beach, C. F. Mecklenbräuker, and G. Hilton, "Short range ultra-wideband multiple input multiple output channel measurements," in *2013 IEEE Wireless Communications and Networking Conference (WCNC)*, April 2013, pp. 2575–2578.
- [43] M. K. Ozdemir, H. Arslan, and E. Arvas, "A mutual coupling model for MIMO systems," in *Wireless Communication Technology, 2003. IEEE Topical Conference on*, Oct 2003, pp. 306–307.
- [44] H. Kanj, S. Ali, P. Lusina, and F. Kohandani, "A modeling approach for simulating MIMO systems with near-field effects," in *Wireless Technology, 2008. EuWiT 2008. European Conference on*, Oct 2008, pp. 143–146.
- [45] M. A. Nikravan, D. H. Kwon, H. G. Schantz, and A. H. Uden, "Near-field MIMO communication utilizing both electric and magnetic field components," in *2014 IEEE Antennas and Propagation Society International Symposium (APSURSI)*, July 2014, pp. 474–475.

REFERENCES

- [46] Y. Tak, S. Yun, J. Park, and S. Nam, "Analysis of a near-field mimo based on the polarization diversity by using the mode-based approach," in *Antenna Technology and Applied Electromagnetics (ANTEM), 2012 15th International Symposium on*, June 2012, pp. 1–4.
- [47] D. Zhang, "Research on channel capacity characteristics of near-field MIMO systems," Ph.D. dissertation, University of Fukui, The address of the publisher, 9 2013.
- [48] M. Jensen and J. Wallace, "A Review of Antennas and Propagation for MIMO Wireless Communications," *IEEE Transactions on Antennas and Propagation*, vol. 52, no. 11, pp. 2810 – 2824, Nov 2004.
- [49] T. A. Laitinen, P. Kyosti, J.-P. Nuutinen, and P. Vainikainen, "On the number of OTA antenna elements for plane-wave synthesis in a MIMO-OTA test system involving a circular antenna array," in *4th European Conference on Antennas and Propagation (EuCAP'10)*, Apr. 2010.
- [50] D. Baum, J. Hansen, and J. Salo, "An interim channel model for beyond-3G systems: extending the 3GPP spatial channel model (SCM)," in *2005 IEEE 61st Vehicular Technology Conference*, vol. 5, May 2005, pp. 3132–3136.
- [51] W. Stutzman and G. Thiele, *Antenna Theory and Design*. John Wiley and Sons, Inc., 2012.
- [52] T. Smith. Notebook on spatial data analysis (online). [Online]. Available: <http://www.seas.upenn.edu/~ese502/#notebook>
- [53] R. Horn and C. Johnson, *Matrix Analysis*. Cambridge University Press, 1985.

REFERENCES

- [54] R. Mersereau and T. Speake, "The processing of periodically sampled multidimensional signals," *IEEE Transactions on Acoustics, Speech, and Signal Processing*, vol. ASSP-31, pp. 188–194, Feb 1983.
- [55] B. Engquist and H. Zhao, "Approximate separability of the Green's function of the Helmholtz equation in the high frequency limit," *Communications on Pure and Applied Mathematics*, vol. 71, pp. 2220–2274, Nov 2018.
- [56] N. A. C. Cressie, *Statistics for Spatial Data*. Wiley, 1993.
- [57] D. P. S. De Iaco, "Wind velocity prediction through complex kriging: Formalism and computational aspects," *Environmental and Ecological Statistics*, vol. 23, no. 1, pp. 115–139, Mar 2016.
- [58] S. Rey and T. Kuerner, "IEEE 802.15-16-0207-01-003d how to drive the channel impulse response from a broadband channel transfer function," *IEEE P802.15 Working Group for Wireless Personal Area Networks*, pp. 1–8, Mar 2016.
- [59] P. L. Kafle, A. Intarapanich, A. B. Sesay, J. McRory, and R. J. Davies, "Spatial correlation and capacity measurements for wideband MIMO channels in indoor office environment," *IEEE Transactions on Wireless Communications*, vol. 7, no. 5, pp. 1560–1571, May 2008.
- [60] J. P. Kermoal, L. Schumacher, P. E. Mogensen, and K. I. Pedersen, "Experimental investigation of correlation properties of mimo radio channels for indoor picocell scenarios," in *Vehicular Technology Conference Fall 2000. IEEE VTS Fall VTC2000. 52nd Vehicular Technology Conference (Cat. No.00CH37152)*, vol. 1, Sept 2000, pp. 14–21.